SCUOLA DI DOTTORATO
UNIVERSITÀ DEGLI STUDI DI MILANO-BICOCCA

Dipartimento di / Department of
Physics “G. Occhialini”

Dottorato di Ricerca in / PhD program in Physics and Astrophysics — Ciclo / Cycle XXIX

Curriculum Subnuclear Physics

Transition Edge Sensor calorimeters for HOLMES

Cognome / Surname Puiu — Nome / Name Paul Andrei

Matricola / Registration number 714152

Tutore / Tutor: Prof. Angelo Enrico Lodovico Nuciotti

Coordinatore / Coordinator: Prof. Marta Calvi

ANNO ACCADEMICO / ACADEMIC YEAR 2016

Dalle rape non si cava sangue

REPARTO DI EMATOLOGIA, IRCSS ISTITUTO NAZIONALE DEI TUMORI

Sarebbe carino...

ANGELO ENRICO LODOVICO NUCCIOTTI. SINCE 1967

No platypus has been harmed or injured in any way in the experiments described in this work.

Contents

Introduction

Neutrinos are the most elusive particle in the Standard model. Since their existence was proposed by Pauli in the 1930 letter, we have made important steps towards the understanding of neutrinos, yet there are important pieces of information missing: we don't know neutrinos absolute mass scale, nor we do know whether they are Majorana or Dirac particles, and finally we have not yet solved the so called hierarchy problem.

In the last two decades, measurements performed at the Super-Kamiokande, SNO, Daya-Bay and RENO neutrinos observatories have shed light on the neutrino oscillation phenomena and have firmly established the fact that neutrinos do have a non zero mass. Neutrino oscillations experiments are sensitive to the square mass difference of neutrino mass eigenstates and they can not provide any information about the absolute mass scale. The most common methods to assess neutrino mass are measurement of the neutrinoless double beta decay rate, cosmological observations and surveys and the direct measurement of the neutrino mass from single beta or electron capture decay spectra. The latter is the only one that can provide a model independent measurement since it is purely kinematic and relies solely on the energy conservation principle.

The topic of this dissertation is the description of HOLMES, an experiment started in 2015, aiming at performing a direct measurement of neutrino mass from the electron capture spectrum of ^{163}Ho. In order to be able to reach the desired sub-eV sensitivity on neutrino mass, very high statistics have to be gathered at the end point, which is the sensitive part of the spectrum to a non zero neutrino mass; ^{163}Ho is a very suitable isotope for this purpouse since its low transition value is close to the energy of the M1 orbital from which electrons are captured, enhancing the event rate close to the end point.

HOLMES will use low temperature calorimeters with Holmium embedded in the detector itself in order to eliminate the systematic uncertainties arising from the use of an external beta emitting source, typical of spectrometers. In its final configuration HOLMES will deploy a 1000 detector array operated at temperatures as low as 60 mK in a dilution refrigerator.

The dissertation will be separated in two parts: in the former I will briefly describe the status of neutrino mass direct measurements focusing in detail on the goals of HOLMES experiment, while in the latter I will describe all the necessary steps taken and yet to be taken for operating the final 1000 detectors array, focusing on the development of the multiplexed readout and the characterization of the single HOLMES detector with the related challenges for achieving the required performances in terms of time and energy resolution for being able to probe the neutrino mass.

I had the opportunity to take part in the HOLMES experiment from the very beginning

of the project. During my PhD program I first instrumented a new dry dilution refrigerator with all the necessary components that would allow us to read out and reconstruct signals from multiplexed rf-SQUIDs coupled to Transition Edge Sensors (TES). I have subsequently started a detailed characterisation of the system starting with the multiplexing system and ending with the TES detectors. In the first cool downs I have measured TES coupled to Bismuth absorbers in order to gain familiarity with the new system, while waiting for the HOLMES detectors to be produced at NIST and shipped to Italy. As soon as I got the first HOLMES prototypes I have started to test them in calibration runs using first a ^{55}Fe source in order to address important issues as the time response and the energy resolutions of the chips; I have therefore switched to a fluorescence multi-line X ray source in order to test the detector linear response on a wider energy range.

The work presented in this thesis was supported by the European Research Council (FP7/2007–2013) under Grant Agreement HOLMES no. 340321.

Chapter 1

Neutrinos

It's been a long time since neutrinos were first proposed in 1930 by Pauli in his famous letter. Since then several radioactive ladies and gentleman have achieved important breakthroughs in understanding the elusive particle. In the following paragraphs I will outline the general framework of neutrino flavour oscillations, followed by a general overview of non oscillation related experiments and finally I will describe the present and future efforts towards a direct measurement of the neutrino mass.

The Standard Model(SM) is the most complete description of particles and their interaction we have ever achieved. It is a gauge field theory invariant under the unitary transformation $SU(3) \otimes SU(2) \otimes U(1)$ and it fully describes the electromagnetic, weak and strong interaction. The SM has passed several high precision tests at the LEP collider and its success culminated with the observation of the predicted Higgs Boson at the LHC. Yet, during the years several physical observations challenged the integrity of the SM, opening up the opportunity of a beyond the SM scenario.

One of the most revolutionary evidences of the limits of the SM came from the observation of neutrino flavor oscillations, which have clearly shown that neutrinos have a non zero mass. However, neutrino oscillation can not directly assess the absolute neutrino mass scale, since they are sensitive only to the squared difference of the value of the mass eigenstates Δm^2_{ij}. Neutrino mass experiments have investigated several different observables:

- Cosmological observations and surveys analysis that are sensitive to the sum of the neutrino masses $\sum_{i=1}^{3} m_i$
- Neutrinoless double beta decay ($0\nu\beta\beta$) rate, sensitive to the parameter $m_{\beta\beta}$
- Precise measurement of the kinematic energy of electrons emitted in weak nuclear processes such as β decay or Electron Capture (EC), which bear the information on effective neutrino mass m_e

1.1 Neutrino mass

After the initial proposal by Pauli, it took twenty years to *see* the neutrino. In 1959 Reines and Cowan [1] [2], observed the inverse beta decay process $\nu_e + p \rightarrow e^+ + n$ using the neu-

trinos produced by a nuclear reactor at Savannah River. In 1962 Lederman, Schwartz et al. measured ν_μ at Brookhaven National Laboratories [3], and finally the first direct evidence of ν_τ comes from the DONUT collaboration in 2000 [4]. The neutrino has no electric charge, is solely left handed and weakly interacting. It can travel through matter with low/no interaction at all for long distances, bearing information about its original energy and direction, and is hence a very important tool for cosmological studies. Its relatively low cross section with matter makes it very difficult to detect and measure, so that up to now many aspects about the neutrino remain unknown.

1.1.1 Neutrino oscillation

The discovery of neutrino oscillations produced quite a revolution in the SM especially because it implies that neutrinos have non zero mass. The very first idea of *oscillating* neutrinos was concieved by Pontecorvo in [5], long before the phenomenon had been experimentally observed. After many years of experimental and theoretical advancements we finally got a more clear picture of the neutrino oscillation, yet some important questions are still open or under investigation, such as the mass hierarchy, CP violation in the leptonic sector and the possibility of existence of a fourth, non-interacting, sterile neutrino. The following brief theoretical introduction can be found in the review by Bellini, Ludhova et al. [6].

Neutrinos interact with matter weakly, via charged-current (CC) and neutral-current (NC) processes. The SM lagrangian term for the interaction are

$$j_i^{CC} = 2 \sum_{l=e,\mu,\tau} \overline{\nu}_{lL} \gamma_i l_L + \dots \tag{1.1}$$

$$j_i^{NC} = \sum_{l=e,\mu,\tau} \overline{\nu}_{lL} \gamma_i \nu_{lL} + \dots \tag{1.2}$$

where l are the charged lepton fields. If neutrinos have non zero mass, the α -flavour interaction field components $\nu_{\alpha L}$ can be a superposition of the left handed components ν_{iL} of the neutrino fields with mass m_i. We can write the following for a highly relativistic neutrino

$$\nu_{\alpha L} = \sum_{i=1}^{N} U_{\alpha i} \nu_{iL} \tag{1.3}$$

where U is a unitary matrix called *PMNS matrix* (*Pontecorvo-Maki-Nakagawa-Sakata*), analogue to the mixing matrix *CKM* for the quark sector [7, 8]. Considering that a field operator creates particles and antiparticles, this implies that a flavor eigenstate $|\nu_\alpha\rangle$ is a superposition of different mass eigenstates $|\nu_i\rangle$ according to

$$|\nu_{\alpha L}\rangle = \sum_{i=1}^{N} U^*_{\alpha i} |\nu_{iL}\rangle \tag{1.4}$$

while for antineutrinos we obtain

$$|\overline{\nu}_{\alpha L}\rangle = \sum_{i=1}^{N} U_{\alpha i}|\overline{\nu}_{iL}\rangle \tag{1.5}$$

The summation index N is not necessarily constrained to three; it can assume larger values, if that were the case, we must assume there there are sterile neutrinos, light fermions that do not interact with either 1.1 nor 1.2, since the LEP collider measurement of the Z boson width showed that $N_\nu = 2.984 \pm 0.008$.

Assuming that there are only three massive neutrinos, the PMNS matrix can be expressed in terms of three mixing angles θ_{12} , θ_{23} and θ_{13}, and one Dirac CP phase δ according to

$$U = R_{23}\left(\theta_{23}\right) \Gamma\left(\delta\right) R_{13}\left(\theta_{13}\right) \Gamma^{\dagger}\left(\delta\right) R_{12}\left(\theta_{12}\right) \tag{1.6}$$

with $R_{ij}(\theta_{ij})$ being the matrix for a θ_{ij} angle rotation in the ij plane and $\Gamma(\delta) = diag\left(1, 1, e^{i\delta}\right)$. This assumes neutrinos are Dirac particles. If that were not the case, for Majorana neutrinos two additional phases have to be considered and the mixing matrix becomes $U \rightarrow U \cdot U_M$ where $U_M = diag\left(1, e^{i\phi_1}, e^{i\phi_2}\right)$. The Majorana phases are not observable in oscillation experiment, they are part of the $m_{\beta\beta}$ observable of the $0\nu\beta\beta$ decay. The mixing matrix can be expressed in components:

$$\begin{aligned}
U &= \begin{pmatrix} c_{12}c_{13} & s_{12}c_{13} & s_{13}e^{-i\delta} \\ -s_{12}c_{23} - c_{12}s_{23}s_{13}e^{i\delta} & c_{12}c_{23} - s_{12}s_{23}s_{13}e^{i\delta} & s_{23}c_{13} \\ s_{12}s_{23} - c_{12}c_{23}s_{13}e^{i\delta} & -c_{12}s_{23} - s_{12}c_{23}s_{13}e^{i\delta} & c_{23}c_{13} \end{pmatrix} \cdot \\
&\cdot \begin{pmatrix} 1 & 0 & 0 \\ 0 & e^{i\alpha_2/2} & 0 \\ 0 & 0 & e^{i\alpha_3/2} \end{pmatrix} = \\
&= \begin{pmatrix} 1 & 0 & 0 \\ 0 & c_{23} & s_{23} \\ 0 & -s_{23} & c_{23} \end{pmatrix} \begin{pmatrix} c_{13} & 0 & s_{13}e^{-i\delta} \\ 0 & 1 & 0 \\ -s_{13}e^{-i\delta} & 0 & c_{13} \end{pmatrix} \begin{pmatrix} c_{12} & s_{12} & 0 \\ -s_{12} & c_{12} & 0 \\ 0 & 0 & 1 \end{pmatrix} \cdot \\
&\cdot \begin{pmatrix} 1 & 0 & 0 \\ 0 & e^{i\alpha_2/2} & 0 \\ 0 & 0 & e^{i\alpha_3/2} \end{pmatrix} \quad , \quad c_{ij} = \cos\theta_{ij} \quad , \quad s_{ij} = \sin\theta_{ij}
\end{aligned} \tag{1.7}$$

It is convenient to indicate with $\Delta m^2_{ij} \equiv m^2_i - m^2_j$, and neutrino mass eigenstates can be orederd so that $\Delta^2 m_{21} > 0$ and $\Delta m^2_{21} \ll |\Delta m^2_{31}|$. The sign of Δm^2_{31} determines the mass

ordering, or hierarchy; in case of $\Delta m^2_{31} > 0$ neutrino mass eigenstates are normal ordered (NH) and for $\Delta m^2_{31} < 0$ neutrino mass eigenstates are in inverse ordering (IH).

The evolution of a state $|\nu(t)\rangle$ is described by the equation

$$i\frac{d|\nu(t)\rangle}{dt} = H|\nu(t)\rangle \tag{1.8}$$

where H is the Hamiltonian operator. We can express the previous equation in term of the flavor eigenstates $\{|\nu_\alpha\rangle\}$ as well

$$i\frac{d|\nu^f(t)\rangle}{dt} = H^f|\nu^f(t)\rangle \tag{1.9}$$

where $\nu^f(t)$ is the vector describing the flavor content of the neutrino state $|\nu(t)\rangle$ given by

$$\nu^f(t) = (a_e(t), a_\mu(t), a_\tau(t), \ldots)^T \tag{1.10}$$

with $a_\alpha(t) = \langle\nu_\alpha|\nu(t)\rangle$, and the matrix H^f is given by

$$H^f_{\alpha\beta} = \langle\nu_\alpha|H|\nu_\beta\rangle \tag{1.11}$$

In vacuum the neutrino Hamiltonian H_{vac} is a function of the neutrino masses and the mixing parameters so that

$$H^f_{vac} = UH^m_{vac}U^\dagger \tag{1.12}$$

with H^m_{vac} being the vacuum Hamiltonian in the mass eigenstate basis given by

$$H^m_{vac} = diag\left(\sqrt{\overrightarrow{p}^2 + m_1^2}, \ldots, \sqrt{\overrightarrow{p}^2 + m_N^2}\right) \approx |\overrightarrow{p}| + \frac{1}{2|\overrightarrow{p}|}diag\left(m_1^2, \ldots, m_N^2\right) \tag{1.13}$$

In the last equality we used the ultra-relativistic approximation $E = |\overrightarrow{p}| + 1/2|\overrightarrow{p}|$ and we assumed that the neutrino state can be described as a superposition of states with fixed momentum $\overrightarrow{p}$, which corresponds to the *plane wave* approximation, that can be used to describe the neutrino evolution when coherence of the different components of the neutirno wave packet is not lost in the propagation and detection processes.

Let's now assume that a neutrino flavor ν_α is created at the time $t = 0$; in the flavor eigenstates basis, this state is

$$\nu^f(0) = (a_e(0), a_\mu(0), a_\tau(0), \ldots)^T \tag{1.14}$$

with components $a_\beta(0) = \delta_{\beta\alpha}$. Applying the time evolution operator, after a time t, the neutrino propagated for a distance $x \simeq t$ and its flavor content evolved with

$$\nu^f(x) = S^f(x)\nu^f(0) \tag{1.15}$$

where the S evolution operator is

$$S^f(x) = T\left[exp\left(-i\int_0^x dx' H^f(x')\right)\right] \tag{1.16}$$

with T being the time ordering operator. In case of neutrino mixing the Hamiltonian H^f is not diagonal. Having non null $\beta \neq \alpha$ components, is it possible to detect a neutrino of flavor ν_β at some distance L from the source; this probability is non zero and, it is computed by

$$P(\nu_\alpha \longrightarrow \nu_\beta) = |a_\beta(L)|^2 = |S^f_{\beta\alpha}(L)|^2 \tag{1.17}$$

In case of vacuum oscillation, the Hamiltonian H is constant and the S operator can be calculated explicitly

$$S^f(x) = US^mU^\dagger \tag{1.18}$$

where S^m is the evolution operator in the mass eigenstates basis, which is

$$S^m = diag(exp(i\phi_1), \ldots, exp(i\phi_N)) \tag{1.19}$$

with $\phi_i = -m_i x/2|\overrightarrow{p}|$. The probability of observing oscillation $\nu_\alpha \longrightarrow \nu_\beta$ after the initial ν_α has traveled over a distance L is given by

$$P(\nu_\alpha \longrightarrow \nu_\beta) = \sum_{i,j} \left[U_{\beta i} U^*_{\alpha i} U^*_{\beta j} U_{\alpha j}\right] exp(i\phi_{ij}) \tag{1.20}$$

where $\phi_{ij} = \left[\left(m_j^2 - m_i^2\right) L\right]/2E$. The above equation can be re-written separating the constant and the oscillating term

$$P(\nu_\alpha \longrightarrow \nu_\beta) = \sum_i |U_{\beta i}|^2 |U_{\alpha i}|^2 + 2\Re\left[\sum_{i>j} U_{\beta i} U^*_{\alpha i} U^*_{\beta j} U_{\alpha j} exp(i\phi_{ij})\right] \tag{1.21}$$

If the phase ϕ_{ij} varies over a range $\Delta\phi_{ij} \gg 1$, as it can because of a large neutrino energy spread or the baseline length, the oscillation effect is averaged. If we assume two neutrino mixing and we consider only one mixing angle θ_{ij}, the oscillation probability can we written as

$$P(\nu_\alpha \longrightarrow \nu_\beta) = sin^2(2\theta_{ij}) sin^2\left(\frac{\Delta m^2_{ij}}{4E}\right) \tag{1.22}$$

For the three neutrino case one can take into account the approximation of a dominant mass scale $\Delta m^2_{21} \ll |\Delta m^2_{31}| \approx |\Delta m^2_{32}|$ which is motivated by the fact that the atmospheric neutrino mass difference is much larger than the solar neutrino mass difference, as can be seen in Figure 1.2.

In the three flavors scenario, only two neutrino mass squared differences are independent: Δm^2_{21} and Δm^2_{31}. For convenience Δm^2_{21} is set to be the smaller of the two and the neutrino will be numbered in such a way that $m_1 < m_2$, so that Δm^2_{21} turns out to be a positive quantity. The angles Θ_{12} and Θ_{23} and the mass squared differences Δm^2_{21} and Δm^2_{32} are determined by the oscillation experiments of solar (ν_e) and atmospheric neutrinos (ν_μ and $\overline{\nu}_\mu$), respectively. The latest data from neutrino experiments (Table 1.1 [9], Figure 1.1) do not allow us to determine the sign of Δm^2_{31}, thus two *hierarchies* are possible (fig. 1.2): *normal hierarchy (NH)* ($m_1 < m_2 \ll m_3$) and *inverted hierarchy (IH)* ($m_3 \ll m_1 < m_2$). The situation where $m_1 \sim m_2 \sim m_3$ is called degenerate pattern.

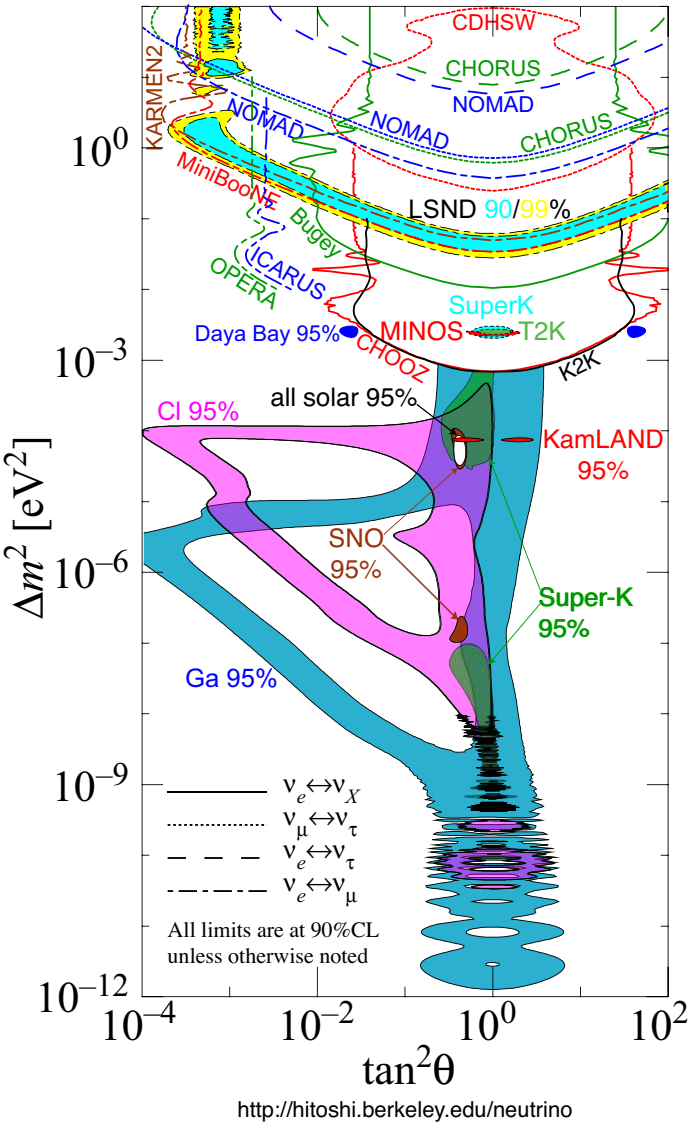

Figure 1.1: Most recent neutrino oscillation parameters.

Parameter	Central value	1σrange	2σrange
$\Delta m^2_{21}/10^{-5}eV^2$ (NH or IH)	7.54	7.32 7.80	7.15 8.00
$\Delta m^2/10^{-3}eV^2$ (NH)	2.43	2.37 2.49	2.30 2.55
$\Delta m^2/10^{-3}eV^2$ (IH)	2.38	2.32 2.44	2.25 2.50
$\sin^2\Theta_{12}/10^{-1}$ (NH or IH)	3.08	2.91 3.25	2.75 3.42
$\sin^2\Theta_{13}/10^{-2}$ (NH)	2.34	2.15 2.54	1.95 2.74
$\sin^2\Theta_{13}/10^{-2}$ (IH)	2.40	2.18 2.59	1.98 2.79
$\sin^2\Theta_{23}/10^{-1}$ (NH)	4.37	4.14 4.70	3.93 5.52
$\sin^2\Theta_{23}/10^{-1}$ (IH)	4.55	4.24 5.94	4.00 6.20
δ/π (NH)	1.39	1.12 1.77	0.00 0.16⊕0.86 2.00
δ/π (IH)	1.31	0.98 1.60	0.00 0.02⊕0.70 2.00

Table 1.1: Latest oscillation parameters. Δm^2 is defined as $m^2_3 - (m^2_1 + m^2_2)/2$, assuming positive values for NH and negative for IH.

The absolute mass scale is not accessible with oscillation experiments. Neither is the Majorana phase. In order to asses these observables, other experiments are needed, such as the ones aiming at measuring the $0\nu\beta\beta$ decay or single β decay end point measurement.

Concerning the hierarchy problem, there are currently two experiments under construction which aim at measuring the disappearance of reactor antineutrinos. The Jiangmen Underground Neutrino Observatory (JUNO) is a 53 km medium baseline reactor neutrino experiment at Kaiping, Jiangmen in Southern Chinam [10], while RENO-50 is a 50 km medium baseline detector located underground in Korea, close to the Hanbit nuclear plant. The JUNO detector consists of a 35.4 m diameter transparent sphere containing 20.000 tons of linear alkylbenzene liquid scintillator, surrounded by approximately 17.000 photomultiplier tubes, a water pool, and a muon veto kept underground. RENO-50 will consist of 18.000 tons of ultra-low radioactivity liquid scintillator and 15.000 photomultiplier tubes, located underground as well.

1.1.2 Non oscillation experiments

As seen in the previous section, the evidence of oscillation amongst different flavors showed a non-vanishing neutrino mass. To assess the mass parameter we shall rely on non oscillation experiments. In the following paragraph I will give a brief overview on the major non oscillation experiments aiming at a measurement of neutrino mass

1.1.2.1 Cosmological measurements

Neutrinos, like any other existing particle, give a contribution to the total energy density of the Universe. Light neutrinos can be considered relativistic for most of the evolution of the

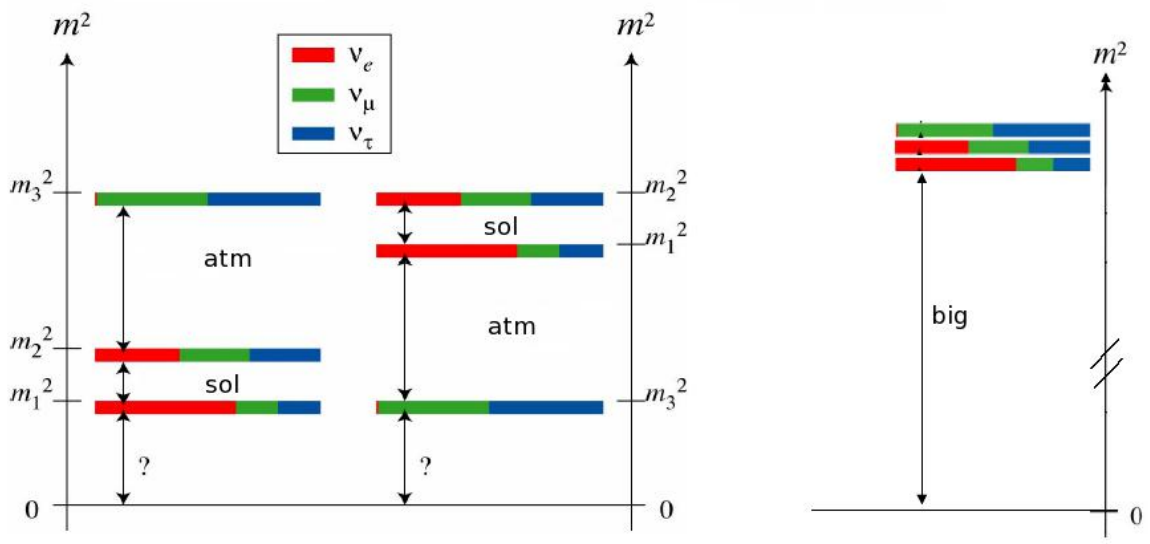

Figure 1.2: The neutrino mass hierarchies. Colors indicate flavor abundance in each mass eigenstate.

Universe. As a consequence, they play an important role in large scale structures formation, with a clear signature in many cosmological observables. The main effect of neutrinos in cosmology is to suppress the growth of fluctuations on scales below the horizon when they become non-relativistic. Because of this suppression it is possible to infer constraints, although indirectly, on the neutrino masses by comparing the most recent cosmological data with the current theoretical predictions. The neutrino energy density ($\Omega_\nu h^2$) is related to the sum of the neutrino masses through

$$\Omega_\nu h^2 = \sum_i m_i/(94\ eV^2) \tag{1.23}$$

with h being the normalised Hubble constant. According to the different datasets considered the limits may vary from fev eV to few hundreds of meV. At the end of a 9-year long data taking, the WMAP collaboration published a constraint on the upper bound on the sum of neutrino masses of 1.3 eV at 95% C.L. [11] assuming the standard cosmologica model CDM. More recently, the Planck data alone set a constraint on $\sum_i m_i$ to 0.72 eV at 95% C.L. [12]. This result should be considered as the most conservative and reliable cosmological constraint on neutrino masses. A tighter bound on the neutrino masses can be obtained by combining CMB observations data with measurements of the Hubble constant H_0 and cosmic distances such as from Type Ia supernovae and Baryon Acoustic Oscillations (BAO). The combined analysis of Plank TT+lensing+polarization+H_0 published in [12] sets a limit of 0.23 eV at 95% C.L.. Current cosmological data probe the region of neutrino masses where the three neutrino states are degenerate. In conclusion, the cosmological observations can lead to results complementary to laboratory experiments, such as single beta decay and neutrinoless double beta decay, but they still are strongly model dependent.

1.1.2.2 Neutrinoless double beta decay

The two-neutrino double beta decay ($2\nu\beta\beta$) was proposed for the first time in 1935 by Maria Goeppert-Mayer [13]. It is a second order process of the SM and its first direct observation dates back to 1987 [14], and it has now been observed in more than ten nuclei [15]. The neutrinoless double beta decay ($0\nu\beta\beta$) has never been observed yet, and if, is an extremely rare process. In the $0\nu\beta\beta$ the two weak vertecses are connected by a neutrino propagator, with only two electrons emitted in the decay. Given the V-A nature of weak interactions, this process would require the coupling of a right-handed anti-neutrino in one vertex and of a left-handed neutrino in the other one. This is possible only if the neutrino is not a chirality eigenstate (i.e. if the neutrino is massive) and if the neutrino and anti-neutrino are two states of the same particle; this would mean that neutrino is a Majorana particle. This decay would violate the conservation of the lepton number by two units, so it is not allowed within the SM theory. Besides, given the very small value of the neutrino mass, the phase space related to the process would strongly suppress the probability of the decay, making it one of the most rare processes that could occur in nature. The lifetime of the neutrinoles double beta decay is expected to be longer than 10^{25} years. The current best limit on $0\nu\beta\beta$ half life is $T^{0\nu}_{1/2} > 2 \cdot 10^{26}$ yr set by the KamLand-ZEN collaboration on the isotope ^{136}Xe. The half life is directly related to the parameter $m_{\beta\beta}$ by

$$\left(T^{0\nu}_{1/2}\right)^{-1} = \frac{|m_{\beta\beta}|^2}{m_e^2} G^{0\nu} |M^{0\nu}|^2 \tag{1.24}$$

with m_e being the electron mass, $G^{0\nu}$ the phase factor, $M^{0\nu}$ the nuclear matrix element and $m_{\beta\beta}$ is the effective Majorana mass. The latter is defined as

$$m_{\beta\beta} = |\sum_i |U_{ei}|^2 e^{i\alpha_i} m_i| \tag{1.25}$$

where U_{ei} are the first raw elements in the PMNS matrix associated with the electron flavour and α_i are the Majorana phases. If the matrix elements are calculated and the squared mass differences are known from the oscillation experiments, it is possible to draw an exclusion plot for $m_{\beta\beta}$ in terms of the mass of the lightest neutrino mass eigenstates and the two Majorana phases. For an accurate estimation of the neutrino mass it is necessary to know $m_{\beta\beta}$ with high accuracy; currently, the greatest contribution to the uncertainties on $m_{\beta\beta}$ comes from the nuclear matrix elements due to unknown details of the nuclear transitions involved in the process. Different calculations of $M^{0\nu}$ exists, relying on different nuclear models. The most recent limits on $m_{\beta\beta}$ are reported in Table 1.2.

1.1.2.3 Single beta decay or electron capture

As described in the previous sections, both the cosmological observations and the $0\nu\beta\beta$ are powerful tools to gather information regarding the neutrino mass with high sensitivity, but both are affected by uncertainties due to the theoretical model of the system they are observing. The only theory-independent method of measuring the neutrino mass is based on the kinematic analysis of electrons emitted in single beta decay. The non vanishing neutrino mass is included in the phase factor calculations and the experimental signature is a

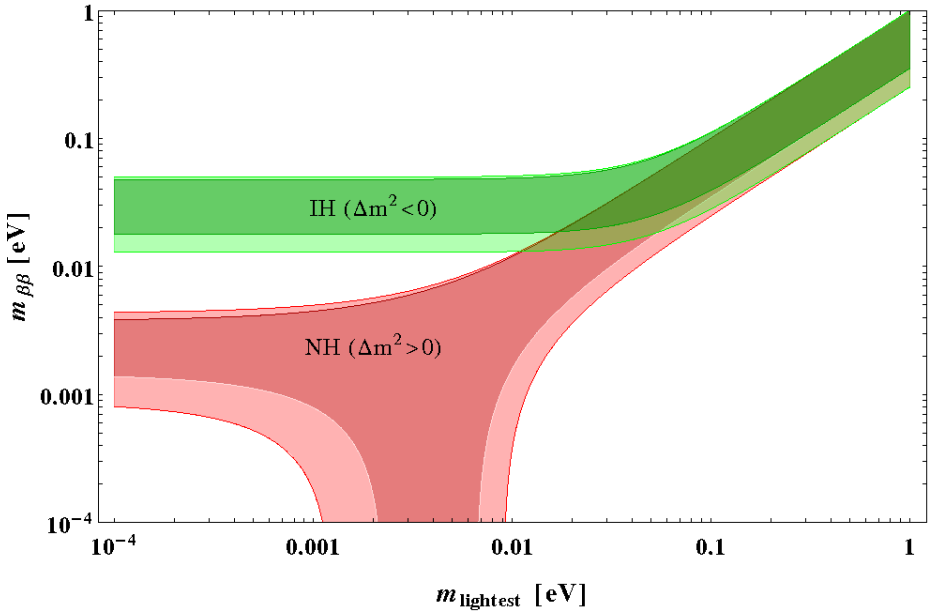

Figure 1.3: Predictions on $m_{\beta\beta}$ as a function of the lightest neutrino mass in the cases of NI and IH. The shaded area correspond to the 3σ interval [16].

shift towards lower energy of the end point, as well as a deformation of the spectrum. The observable accessible for single beta or electron capture neutrino experiments is

$$m_{\nu_e} = \sqrt{\sum_{i=1}^{3} |U_{ei}|^2 m_i^2} \tag{1.26}$$

The sum runs over all the three mass eigenstates since it is not possible to disentangle each contribution experimentally. Even so, by setting a limit on ν_e, a limit on the lightest mass eigenstate is set as well. Combining the single beta decay data with the oscillations data, which will give the values and the signs of Δm_{ij}^2 and the mixing parameters $|U_{ei}|^2$, from the measured the value of m_{ν_e}, the neutrino mass squared (m_j^2) can be determined with

$$m_j^2 = m_{\nu_e} - \sum_i |U_{ei}|^2 \Delta m_{ij}^2 \tag{1.27}$$

In case only Δm_{ij}^2 is known, from the limit calculated from the single beta decay, a limit on the heaviest neutrino mass eigenstate can be given

$$m_{max}^2 = m_{\nu_e} - \sum_{i>j} |\Delta m_{ij}^2| \tag{1.28}$$

In Table 1.3 the current limits for direct neutrino searches are shown. In the following chapter I will give an overview on the current experiments aiming at a direct observation of the neutrino mass from either beta decay or electron capture spectra.

$m_{\beta\beta}$ (eV)	Isotope	% C.L.	Experiment
<0.42 - 0.66	^{76}Ge	90	Heildeberg-Moscow [17]
<0.33 - 1.35	^{76}Ge	90	IGEX [18]
<0.2 - 0.4	^{76}Ge	90	GERDA [19]
<0.94 - 2.5	^{82}Se	90	NEMO-3 [20]
<0.3 - 0.9	^{100}Mo	90	NEMO-3 [21]
<0.27 - 0.76	^{130}Te	90	CUORE-0 [22]
<0.14 - 0.28	^{136}Xe	90	KamLAND-Zen [23]
<0.19 - 0.45	^{136}Xe	90	EXO [24]
<1.1 - 2.7	^{136}Xe	90	DAMA [25]

Table 1.2: Most recent limits on the effective Majorana mass.

m_β eV	C.L. %	Experiment	Isotope	Technique
15	90	Mibeta	^{187}Re	Calorimetric
2.05	95	Troitsk	^{3}H	Spectrometric
2.03	95	Mainz	^{3}H	Spectrometric

Table 1.3: Current limits on the electron neutrino mass.

Chapter 2

Direct Measurements

In this chapter I will make an overview of the single beta decay measurements and I will refer to the past and present experiments that set a limit and currently aim at a measurement of the neutrino mass. In the former part I will briefly describe the single beta decay process and the experimental challenges. In the latter section I will describe past and current experiment, such as KATRIN, aiming at pushing the sensitivity on neutrino mass down to 0.2 eV by measuring the energy of electrons emitted in Tritium decay. Finally I will say a few words about ECHo and NuMECS, who aim at measuring the neutrino mass from the ^{163}Ho decay spectrum.

2.1 Direct mass measurement

As already mentioned, the only theory-independent method for probing the neutrino mass is the measurement of the kinetic energy of the electron emitted in a single beta process, either beta decay or electron capture (EC). Currently the most stringent limits come from spectrometric experiments, which set the m_ν to be smaller than 2.1 eV.
The β-decay is a nuclear process that involves two isobar nuclides with the emission of an electron and an anti-neutrino:

$$(A, Z-1) \rightarrow (A, Z) + e^- + \overline{\nu}_e \tag{2.1}$$

For a single beta decay the actual mass term is that of the anti-neutrino, which, according to the CPT theorem, is equal to the neutrino mass. The total energy Q released is

$$Q = M(A, Z-1)c^2 - M(A, Z)c^2 \tag{2.2}$$

where M indicates the total mass of the atom.
By neglecting the recoil of the nucleus, and calling E_0 the maximum kinetic energy available to the electron, the energy distribution of the electrons emitted is described by:

$$N_\beta = p_\beta E_\beta \left(E_0 - E_\beta\right) \sqrt{\left(E_0 - E_\beta\right)^2 - m_{\nu_e}^2 c^4} F\left(Z, E_\beta\right) S\left(E_\beta\right) \left[1 + \delta_R\left(Z, E_\beta\right)\right] \tag{2.3}$$

where p_β and E_β are respectively the momentum and the energy of the e^-. In the equation (2.3) the following parameters are present:

- $p_\beta \left(E_\beta + m_e c^2\right) (E_0 - E_\beta) \sqrt{(E_0 - E_\beta)^2 - m_{\nu_e}^2 c^4}$ is the phase-space of a three-body decay.
- $F(Z, E_\beta)$ is a Coulomb correction (Fermi function), which takes into account for the effects due to the charge of the nucleus on the wave function of the emitted electron. Considering the relativistic effects and a finite dimension of the nucleus it becomes:

$$F(Z, E_\beta) = 4 \left(\frac{2 p_e R}{\hbar}\right)^{2\gamma-2} e^{\pi\eta} \left|\frac{\Gamma(\gamma + i\eta)}{\Gamma(2\gamma+1)}\right|^2 \approx \frac{2\pi\eta}{e^{-2\pi\eta}} \tag{2.4}$$

  where $\eta = \alpha Z E_\beta 7 p_e$, $\gamma = \left(1 - (\alpha Z)^2\right)^{1/2}$, R is the nuclear radius ($R = 1.2A^{1/3} fm$) and α is the fine structure constant. The expression (2.4) is obtained as solution of the Dirac equation assuming point-like nucleus, evaluated at R distance from the nucleus. When we consider the shielding of the (Z-1) electrons of the parent nucleus, this term gets a further correction factor

$$F(Z, E_\beta)' = F(Z, E_\beta - \langle V_\beta \rangle) \frac{E_\beta - \langle V_\beta \rangle}{E_\beta} \tag{2.5}$$

  where $\langle V_\beta \rangle$ is the average potential experimented by the electron at the nuclear surface due to the atomic electrons. In the Thomas-Fermi model it is $\langle V_\beta \rangle = 1.45 m_e \alpha^2 Z^{4/3}$.
- $S(E_\beta)$ is the form factor of the beta spectrum which takes into account the nuclear matrix element $M(E_\beta)$ of the electro-weak interaction. In can be expressed as:

$$S(E_\beta) = G_F^2 \left(\frac{m_e^5 c^4}{2\pi^3 \hbar^7}\right) \cos^2\Theta_C |M(E_\beta)|^\epsilon \tag{2.6}$$

  where G_F is the Fermi coupling constant and Θ_C is the Cabibbo angle.
- δ_R, finally, is the electromagnetic radiative correction, which can be neglected due to the smallness of this value.

An easy way to picture the effect of the neutrino mass is the use of *Kurie plot*, where the variable $K(E_\beta)$ is plotted as a function of the energy of the electron E_β:

$$K(E_\beta) = \sqrt{\frac{N_\beta(Z, E_\beta, m_{\nu_e})}{p_\beta E_\beta F(Z, E_\beta) S(E_\beta) [1 + \delta_R(Z, E_\beta)]}} = (E_0 - E_\beta) \left(1 - \frac{m_{\nu_e}^2 c^4}{(E_0 - E_\beta)^2}\right)^{1/4} \tag{2.7}$$

In the ideal case of infinite energy resolution, one can observe that the *Kurie plot* is a straight line that, whit $m_\nu = 0$, intersects the energy axis at the total transition energy, while in case of $m_\nu \neq 0$ a distortion from the linearity is observable near the end-point, as can be seen in Figure 2.1. It is clear from this plot that the region of interest of the spectrum for the measurement of neutrino mass is the upper tail, where the sensitivity to m_ν is higher. Unfortunately, the closer the energy gets to the Q-value, the smaller the event rate is. The fraction of events within the energy interval $\Delta E \approx 3 m_{\nu_e}$ is

$$F_{\Delta E}(E) = \int_{E_0 - \Delta E}^{E_0} N_\beta(Z, E_\beta, m_{\nu_e} = 0) dE \approx 2 A_\beta \left(\frac{\Delta E}{E_0}\right)^3 \tag{2.8}$$

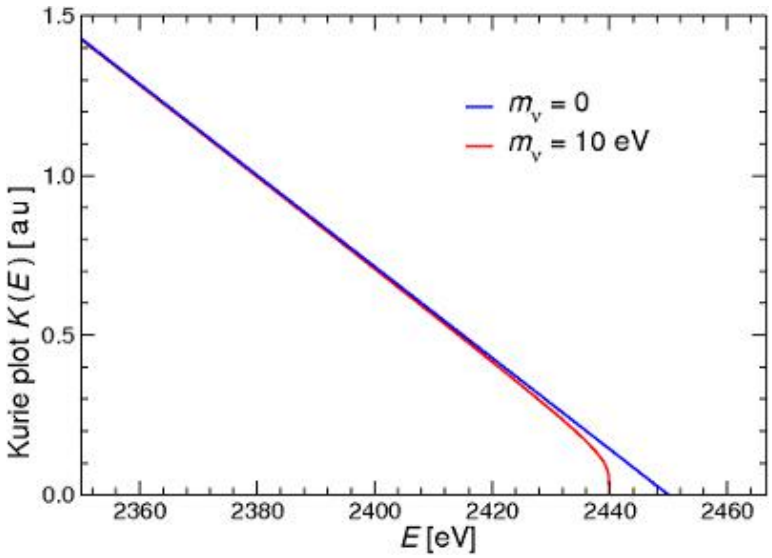

Figure 2.1: *Kurie plot* in the case $m_\nu = 0$ (blue line) and $m_\nu = 5$eV (red line).

Besides the low statistics, there are other systematic effects that contribute to hiding the effect of a non vanishing mass neutrino mass. To compensate for the finite energy resolution of the detector, a precise knowledge of the detector response function is necessary. Furthermore, the decay could occur with the daughter atom into an excited state and the de-excitation energy could be released after the response time of the detector; this source effect causes a distortion of the spectrum. The final spectrum will then be the sum of different single final state spectra

$$N_\beta(Z, E_\beta, m_{\nu_e}) \approx \sum_i w_i p_\beta E_\beta (E_0 - E_\beta - V_i)^2 \left(1 - \frac{m_{\nu_e}^2 c^4}{(E_0 - E_\beta - V_i)^2}\right) F(Z, E_\beta) S(E_\beta) \quad (2.9)$$

where w_i and V_i are the probabilities and the energies of transition of the *i*-th final level. This effect is particularly misleading in measuring the neutrino mass: as becomes evident by assuming $m_{\nu_e} = 0$ and summing over all the final states:

$$N_\beta(Z, E_\beta, 0) \approx p_\beta E_\beta (E_0 - E_\beta - \langle V_i \rangle)^2 \left(1 + \frac{\langle V_i^2 \rangle - \langle V_i \rangle^2}{(E_0 - E_\beta - \langle V_i \rangle)^2}\right) F(Z, E_\beta) S(E_\beta) \quad (2.10)$$

which would correspond to a beta spectrum with a neutrino squared mass equal to $-\sigma^2 = -\left(\langle V_i^2 \rangle - \langle V_i \rangle^2\right) < 0$!
Another non–negligible systematic in the end-point region comes from the radioactive background, which, due to the very poor statistics at the end point, may become a significant contribution. An uncertainty δB in the radioactive background evaluation results in a distortion of the spectrum

$$N_\beta = p_\beta E_\beta (E_0 - E_\beta)^2 \left(1 + \frac{\delta B}{p_\beta E_\beta (E_0 - E_\beta) F(Z, E_\beta) S(E_\beta)}\right) F(Z, E_\beta) S(E_\beta) \quad (2.11)$$

A deformation of this kind could lead to a negative neutrino squared mass equal to $-2\delta B/[p_\beta E_\beta FS]$. In order to increase the statistics of the events close to the end-point, a low Q-value β-decay emitter is preferable (eq. 2.8). To date the most important results obtained by direct measurement of the neutrino mass are based on ^{3}H and ^{187}Re β-decays.
Tritium beta decay is a super-allowed transition with a low end-point energy of 18.6 keV. Thanks to its rather short half-life of 12.3 y, it is possible to create sources with high specific activity. This isotope is used in spectrometric experiments. ^{187}Re decays via a unique forbidden transition at 2.47 keV. One of the most interesting isotopes however is ^{163}Ho, which decays via electron capture with a Q-value of 2.88 keV and, even though it is not the lowest known, it represents a very valid alternative due to the proximity of its Q-value to the M1 shell energy from which the electron is capture, providing an enhancement of the event rate close to the endpoint.

2.1.1 Spectrometric experiments

The experiments aimed at the measurement of the neutrino mass that use spectrometers are divided into two categories: magnetic and electrostatic with magnetic collimation. The former is used to select the energy of the electrons by means of the bending effect of a proper magnetic field, while in the latter the electrons are collimated by a magnetic field and then selected by a potential barrier. Before the '90s, the magnetic spectrometers were the most sensitive instruments for neutrino mass measurement, achieving a sensitivity of 10-20 eV. The electrostatic spectrometers are characterized by a higher energy resolution ($\sim$ 1 eV for next generation experiments), a stronger rejection of the background and a higher luminosity.
The main advantage that made spectrometers competitive in direct mass measurement experiments so far is the filtering capability: only the useful fraction of electrons with energies very close to the transition energy can be selected. Therefore very high statistics can be accumulated in the interval of interest.
On the other hand, using an external source implies that the response function is a convolution of the exact transmission function T of the spectrometer with four correcting functions that take into account the effects of energy loss, source charging, backscattering from the substrate (present when the source is deposited on a solid substrate) and the energy dependence of detection efficiency [26]. The results of the Mainz and Troitzk experiments brought to attention that there are other factors that play a significant role: Mainz improved its results only after including a *rugosity* effect of the tritium source [**?**], while Trostzk needed to add a step function of unknown origin in the integral spectrum of the electron in order to get a significant result on the neutrino mass [27]. Finally, the energy spectrum is the superposition of different spectra due to decays on excited states (eq. 2.9).
The spectrometer is a rather complicate system and, in order to be sensitive to the tiny effect of the neutrino mass, the response function must be computed with extreme accuracy and every systematic must be kept in check.

2.1.1.0.1 KATRIN The Karlsruhe Tritium Neutrino (KATRIN) is the ultimate spectrometer experiment that will start collecting data from a tritium source in 2017. In KATRIN

the electrons are emitted by a windowless gaseous ^{3}H source and are guided adiabatically through a 70 meter long vacuum pipe to the spectrometer, pushing the spectrometer technology to the extreme. A decay rate of 10^{11} events/s is required from the source, which will be kept at 27 K; a flux of 10^{19} T_2 molecules/s will be injected at the midpoint of the source. A crypumping section will keep the T_2 flux from the source to the spectrometer lower than 10^5 molecules/s, while a pre-spectrometer will operate a first energy selection, allowing only the high energy electrons to enter the main spectrometer, so that background effects due to ionizing collisions are reduced. Background electrons, which are emitted from the spectrometer walls, will be screened off electrostatically by an inner grid system. KATRIN aims to pushing down the present sensitivity of 2 eV by of one order of magnitude, reaching 0.2 eV [28].

2.1.1.0.2 Project 8 Project 8 is an ambitious project which exploits a novel technique for measuring the neutrino mass. Project 8 will measure the frequency of cyclotron radiation of the electrons emitted from a tritium source [29]. While propagating in a region where a constant magnetic field is present, the electrons follow a cyclotron motion which occurs at a frequency that depends on the kinetic energy of the charged particle. By measuring the cyclotron radiation it is then possible to extract the original energy of the electrons and to construct in this way the beta spectrum exploiting the high precision which can be achieved in a frequency measurement.
In a recent presentation at Neutrino 2016, Project 8 achieved an energy resolution FWHM of 3.3 eV on the 30 keV emission lines of ^{83m}Kr.

2.1.2 Calorimetric experiments

In an ideal calorimetric experiment the source is embedded inside the detector; in this way all the energy is detected, except for the fraction taken from the neutrino. This approach eliminates completely the effects of the decays on excited states since the detector integrates all the energy released within its response time. In general the advantages of a calorimetric measurement are:

- capability to collect all the energy, including decays on excited levels
- no self-absorption
- no backscattering

There is however a limitation related to this approach. Having the isotope embedded in the detector, it is not possible to operate a selection *a priori* of the emitted electrons hence every decay will be recorded, setting a limit on the maximum count rate in order to limit the unresolved pile up, which poses a serious threat to the determination of m_ν. The faster the detector, the less the fraction of unresolved pile-up.
If we denote with τ_R the detector time resolution and assuming that the events follow the Poisson distribution, in a first approximation the fraction of events suffering pile-up is:

$$P(\Delta t < \tau_R) = 1 - e^{A_\beta \tau_R} \approx A_\beta \tau_R \tag{2.12}$$

where A_β is the activity of the source and Δt is the temporal separation of two events. Considering the presence of pile-up, the beta spectrum is:

$$N'_\beta = N_\beta\left(Z, E\right) + \left(1 - e^{-A_\beta \tau_R}\right) \int_0^{E_0} N_\beta\left(Z, E'\right) N_\beta\left(Z, E - E'\right) dE' \tag{2.13}$$

The number of spurious events caused by pile-up is obtained by integration of the pile-up spectrum in the interval ΔE below the end-point

$$F^{pp}_{\Delta E} = A_\beta(1 - e^{A_\beta \tau_R}) \int_{E_0-\Delta E}^{E_0} dE \int_0^{E_0} dE' N_\beta(Z, E') N_\beta(Z, E - E') \tag{2.14}$$

2.1.3 Holmium 163

During the last decades the international community focused with increasing interest on the ^{163}Ho electron capture (EC) as a powerful means for neutrino mass determination. ^{163}Ho decays to ^{163}Dy with a convenient low transition energy of 2.88 keV [30]. The capture is only allowed from the M shell or higher, and the dauther Dy* decays via non radiative atom de-excitation. [1] and from the Inner Bremsstrahlung (IB) radiation. There are at least three proposed independent methods to estimate the neutrino mass from the ^{163}Ho EC: absolute M capture rates or M/N capture ratios [31], IB end-point [32] and calorimetric de-excitation spectrum end-point measurement [33].

2.1.3.0.3 Absolute M capture rates or M/N capture rate ratios The EC decay rate can be expressed as a sum over the possible levels of the captured electron [34]:

$$\lambda_{EC} = \frac{G_\beta^2}{4\pi^2} \sum_i n_i C_i \beta_i^2 B_i \left(E_0 - E_i\right) \left[\left(E_0 - E_i\right)^2 - m_\nu^2\right]^{1/2} \tag{2.15}$$

where $G_\beta = G_F \cos\Theta_C$, n_i is the fraction of occupancy of the i-th atomic shell, C_i is the atomic shape factor, β_i is the Coulomb amplitude of the electron radial wave function and B_i is an atomic correction for electron exchange and overlap. It is important to note that every single addend of equation 2.15 has a dependence on m_ν, which can be constrained by measuring the ratios of absolute capture rates

$$\frac{\lambda_i}{\lambda_j} = \frac{n_i p_{\nu,i} E_{\nu,i} \beta_i^2 \beta_i}{n_j p_{\nu,j} E_{\nu,j} \beta_j^2 \beta_j} \tag{2.16}$$

2.1.3.0.4 Inner Bremsstrahlung end-point From eq. 2.3 it is evident that one can measure the neutrino mass from the energy spectrum of the electrons emitted in the decay, because of the neutrino mass term in the phase-space factor $\left(E_0 - E_\beta\right)\sqrt{\left(E_0 - E_\beta\right)^2 - m_{\nu_e}^2 c^4}$. A similar factor exists also for the emission rate of Internal Bremsstrahlung in Electron Capture (IBEC). To date, only one experiment actually measured the IBEC spectrum from ^{163}Ho decay, but the measurement was compromised by background [35].

[1] The intensity of the radiative decays with respect to the non radiative ones is below one part per thousand.

2.1.3.0.5 Calorimetric absorption spectrum end-point The expression of the de-excitation spectrum has again a dependence on the neutrino mass through the phase-space factor, where the energy of the β-electron is replaced by the total de-excitation energy. The spectrum features Breit-Wigner peaks resonances centered at the ionization energies E_i of the captured electrons. Given the finiteness of the intrinsic width of the lines the total spectrum presents a continuum between adjacent peaks, coming from the overlap of the tails of every resonance. The distribution of the de-excitation energy E_c is [33]:

$$\frac{d\lambda_{EC}}{dE_c} = \frac{G_\beta^2}{4\pi^2}(E_0 - E_c)\sqrt{(E_0 - E_c)^2 - m_\nu^2 c^4}\sum_i n_i C_i \beta_i^2 B_i \frac{\Gamma_i}{2\pi}\frac{1}{(E_c - E_i)^2 + \Gamma_i^2/4} \tag{2.17}$$

For single beta decay, the spectrum is truncated at $E_0 - m_\nu$ and the sensitivity on m_ν is strictly related to the fraction of events at the end-point.

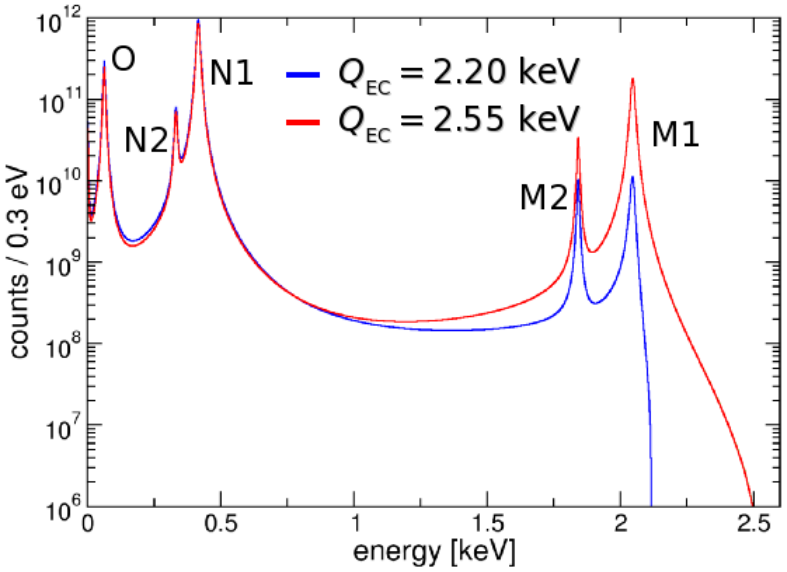

Figure 2.2: De-excitation spectrum coming from the EC of ^{163}Ho with the two possible Q-values. The two spectra have been calculated considering an energy resolution $\Delta E_{FWHM} = 2$ eV, a fraction of events affected by pile-up $f_{pp} = 10^{-6}$ and a number of events $N_{ev} = 10^{14}$.

In Figure 2.2 two spectra corresponding to two possible transition energies are plotted, while in Figure 2.3 the effects of a finite neutrino mass on the end-point are displayed, considering a Q=2.555 keV because at the time of the proposal the expected Q-value was 2555 eV.

The total statistics N_{ev} is a crucial parameter for reaching a sub-eV neutrino mass statistical sensitivity, which scales as $N_{ev}^{-1/4}$. The energy resolution, in the range achievable with the present microcalorimeters technology, does not play a significant role, while the fraction of unresolved pile-up events has a strong effect on the statistical sensitivity.

The ideal detector candidate must be easily scalabile to arrays of $\gtrsim 10^3$ detectors, have a fast response ($\sim$ μs), in order to allow the acquisition of the highest possible statistics while keeping the contribution of the pile-up events as small as possible.

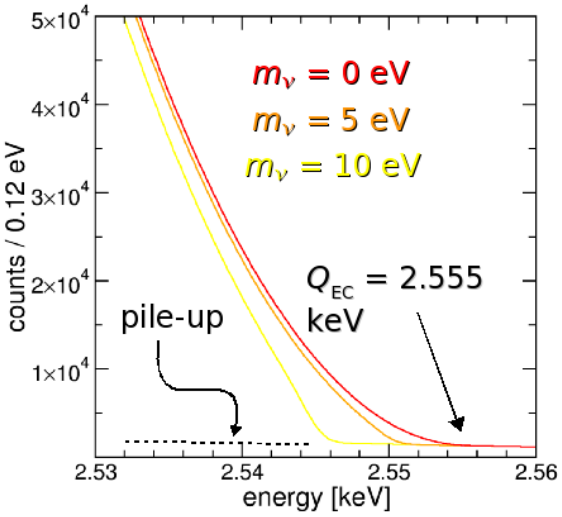

Figure 2.3: Effect of different values of m_ν on the shape of the ^{163}Ho spectrum at the end point. A Q=2.555 keV has been considered.

In the following chapters I will outline the solutions adopted by HOLMES in order to perform a neutrino mass measurement with 1 eV sensitivity.

Chapter 3

^{163} Ho isotope

In the following chapter I will outline the reasons why ^{163}Ho is a very promising isotope for the search of neutrino mass from the Electron Capture decay spectrum. ^{163}Ho is not a naturally abundant isotope, so I will briefly describe the necessary steps for its production. Finally I will address the issue of the sensitivity to neutrino mass from an acquired energy spectrum.

3.1 EC-decay spectrum

A Holmium based experiment for measuring the neutrino mass was proposed by De Rújula and Lusignoli in the 1980's in [33] and in [36]. In the papers, the authors describe the decay spectrum of ^{163}Ho emphasising the event rate enhancement due to the proximity of the end point to the atomic resonance M1 and, for the first time they propose a calorimetric experiment for measuring the neutrino using ^{163}Ho. The initial rationale for looking for another isotope at a time when ^{3}He spectrometers were improving their sensitivity and making progress towards the eV scale was the systematic uncertainties arising from the use of a Tritium source or, to say it as De Rújula and Lusignoli said it, to avoid the "molecular interplay" problem connected to the use of an external source. The operating principle of the calorimetric experiment proposed in [33] for ^{163}Ho was to record the "calorimetric" energy E_c that, together with the neutrino energy E_ν adds up to the Q-value, which ultimately is the mass difference between the ^{163}Ho and the daughter ^{163}Dy atoms.

In the following paragraphs will analyse the spectrum of the calorimetric energy E_c emitted in the decay process

$$^{163}\mathrm{Ho} \longrightarrow \nu_e(E_\nu) +^{163}\mathrm{Dy}^{H} \longrightarrow^{163}\mathrm{Dy} + E_c \tag{3.1}$$

where H labels the hole left in the daughter atom by the electron capture. Capture is indeed allowed only from orbitals with a non vanishing wave function at the origin, i.e. $H = nS$ and $H = nP_{1/2}$. If E_H is the positive energy of the ionisation of the H orbital and Q is such that $E_L < Q < E_M$, the capture can occur only for electrons with energy lower than the M1 shell($n > 2$). The recoil energy of the Dy atoms $E_{Dy} < 2 \cdot 10^{-5}$ eV is completely negligible so

we safely state that $Q = E_c + E_\nu$ with the calorimetric spectrum being a measurement of the neutrino energy as well.

We can now proceed with the construction of the E_c, and hence the E_ν spectrum: the E_c spectrum is the sum of peaks at $E_c = E_H$ with relative height according to the ratios of the orbital wave function at the origin $|\phi_H(0)|^2$. The peaks have Breit-Wiegner shape with natural width Γ_H equal to the excited Dy_H. An easy way used by De Rújula and Lusignoli in order to explain the E_c spectrum is to look at the calorimetric spectrum dW/dE_c with $E_c = Q - E_\nu$ and to think of E_ν as of the neutrino spectrum dW/dE_ν of a two body process with the neutrino recoiling on a series of states with width non zero width. This way we can write

$$dW/dE_c = N\left\{(Q-E_c)\left[(Q-E_c)^2 - m_\nu^2\right]^{1/2}\right\} \times \sum_H |\phi_H(0)|^2 \frac{\Gamma_H}{2\pi} \frac{1}{(E_c - E_H)^2 - \Gamma_H^2/4} \quad (3.2)$$

and its integral, in the very good narrow width approximation, which allows us to neglect non resonant contributions, is

$$W = \sum_H |\phi_H(0)|^2 (Q-E_H)^2 \left[(Q-E_H)^2 - m_\nu^2\right]^{1/2} \quad (3.3)$$

The phase space factor $\left\{(Q-E_c)\left[(Q-E_c)^2 - m_\nu^2\right]^{1/2}\right\}$ is $E_\nu|p_\nu|$. The Dy atoms decay predominantly by emitting Auger electrons, with fluorescence yields f(M1) = $1.1 \cdot 10^{-3}$, f(M2) = $1.8 \cdot 10^{-3}$, f(N1) = $3.7 \cdot 10^{-5}$, f(N2) = $7.0 \cdot 10^{-5}$.

Until 2015, when Eliseev et al. performed a precise Penning trap measurement of the mass difference between ^{163}Ho and ^{163}Dy, which turned out to be the unfortunate $2833(30_{stat})(15_{sys})$eV, the Q-value of the ^{163}Ho decay was not precisely known. Most of the previous estimations relied on the M1/N1 and M1/M2 peak ratios, which is sensitive to the Q-value, as shown in Figure 3.1. Besides, the peak ratio is sensitive to neutrino mass too, even though the effect depends on Q, and it was estimated to be the order of 5% for Q=2555 keV, making it ultimately very difficult to observe for Q=2833.

3.1.1 Neutrino mass sensitivity

The sensitivity on neutrino mass is achieved by collecting as many events as possible at the high end of the E_c spectrum. The first crucial question is one of counting rate. We can define a figure of merit g as the fraction of events in the interval (Q-m_ν, Q) in the normalized spectrum dW/WdE_c

$$g(Q, m_\nu) = \frac{1}{W(Q)} \int_{Q-m_\nu}^{Q} dE_c \frac{dW(Q, m_\nu = 0)}{dE_c} \quad (3.4)$$

This is a good measure of the difference in fractional counting rates for m_ν=0, $m_\nu \neq$O. The figure of merit in ^{3}H decay is $g \sim 8 \cdot 10^{-9}\ (m_\nu/30eV)^3$. The figure of merit for ^{163}Ho is not necessarily cubic in neutrino mass due to the Breit-Wiegner matrix element affecting the spectral shape. For the sake of comparison, the figure of merit for ^{163}Ho computed using

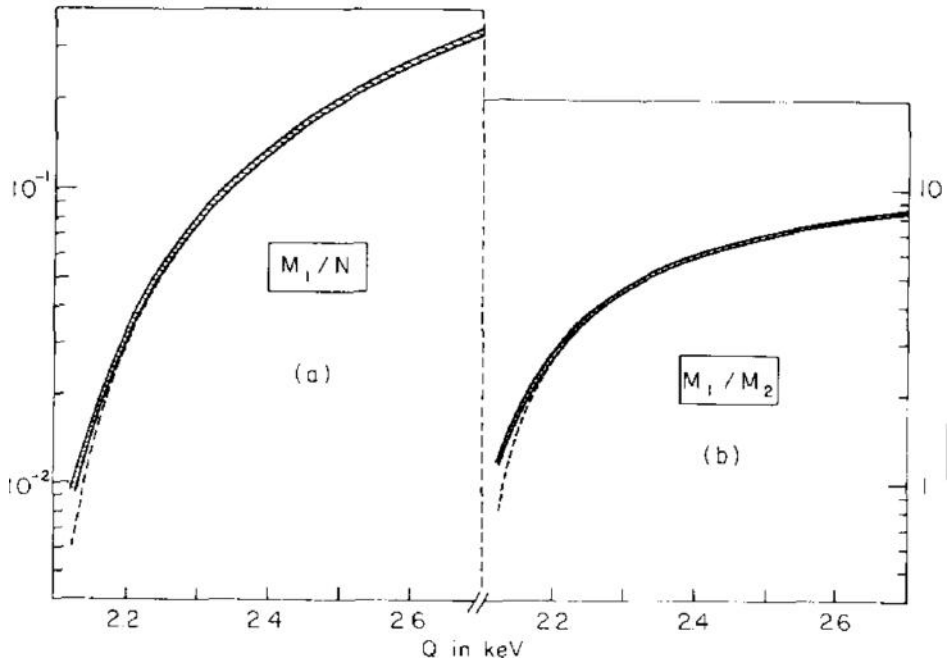

Figure 3.1: Original calculations of the peak ratio as a function of Q made by De Rújula and Lusignoli; peak heights with gaussian resolution (FWHM= 100 eV), for m_ν=0 and m_ν=60 eV.

the most recent value for Q=2833 eV, and the data in Table 3.1, assuming an infinite detector resolution and with a neutrino mass $m_1 nu$=30 eV is $g = 2.65 \cdot 10^{-8}$.

The figure of merit in case of m_ν=1 eV and m_ν=10 eV for ^{163}Ho is $g_{1\ eV} = 4.89 \cdot 10^{-13}$ and $g_{10\ eV} = 4.92 \cdot 10^{-10}$.

Level	E_i [eV]	Γ_i [eV]
M1	2047	13.2
M2	1842	6.0
N1	414.2	5.4
N2	333.5	5.3
O1	49.9	
O2	26.3	

Table 3.1: Energy levels of the captured electrons, with their widths, for ^{163}Dy

In principle one could design an experiment with the highest activity possible in order to gather enough statistics to reach sub eV sensitivities to neutrino mass, yet there is a limiting factor, which is related to the finite time resolution of the detection system: the pile-up. A case of pile-up is when two single events accidentally occur within the same time resolution window, and the detector registers the sum of their energies. The time resolution τ_R is

the crucial detector parameter that needs to be optimised in order to keep the pile-up low. Yet, the possibility of pile-up can not be ruled out, and a precise calculation of the pile-up spectrum is necessary for evaluating the ultimate experimental sensitivity on neutrino mass. We define N and $T_{1/2}$ as the number and half-life of ^{163}Ho atoms. The fraction of accidental double coincidences per single event is $N \cdot \tau_R \ln 2/T_{1/2}$. The energy spectrum of accidental double coincidences, normalized in the same way, is shown in Figure 3.2 (pile-up fraction 10^{-4}) altogether with the single hit E_c spectrum. The predicted form for the accidental coincidences dA

$$\frac{dA}{dE_c} = \frac{N\tau_R \ln 2}{T_{1/2}} \frac{1}{a} \frac{da}{dE_c} \tag{3.5}$$

with

$$\frac{1}{a}\frac{da}{dE_c} = \frac{1}{W}\int dE_1 dE_2 \frac{dW}{dE_1}\frac{dW}{dE_2}\delta(E_c - E_1 - E_2) \tag{3.6}$$

where dW/WdE_c is the usual normalised spectrum described in the previous paragraphs

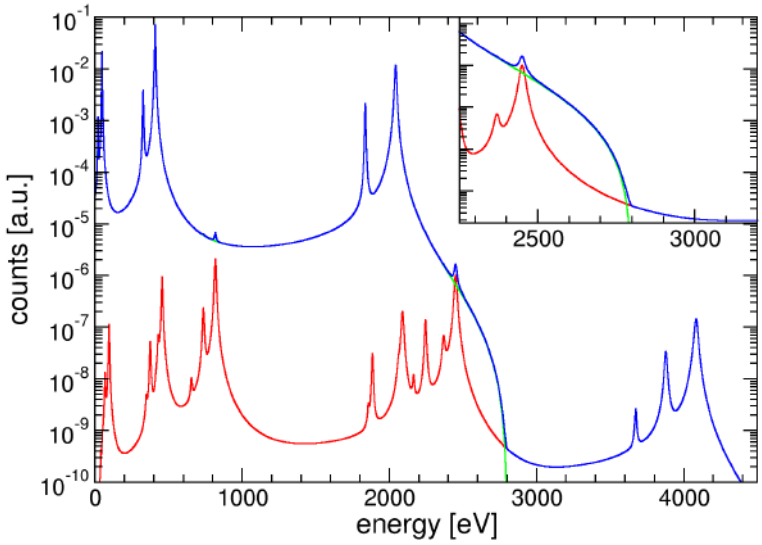

Figure 3.2: Single hit E_c spectrum and $\frac{1}{a}\frac{da}{dE_c}$ double hit pile-up spectrum

The endpoint of single hit spectrum is close to the M+N peaks of the double hit spectrum. To get a more clear overview of the relevance of unresolved pile-up, I will show the number of atoms $N(Q)$ for which single and accidental events are equally numerous in the region sensitive to the neutrino mass. The calculation is done for an experiment with detector resolution FWHM$> m_\nu$ in a region of interest ranging from Q-FHWM to Q+FWHM. For τ_R=1 μs and FWHM=1 eV, N(Q=2.8 keV)=$2\cdot10^{13}$. Even though just an exercise, the calculation gives an idea about the order of magnitude of the isotope quantity needed for performing an experiment.

The spectral shape calculated in the previous paragraph is the starting point for the simulations performed for estimating the HOLMES sensitivity, which will be described in the following chapters.

3.1.2 Two hole contributions

In recent years Robertson showed concerns [37] about the two-hole contribution being not totally negligible. During the EC process, the wave function of the non captured electrons in the original and in the daughter atom are not identical and the mismatch between them can lead to the instantaneous creation of secondary holes H′. An electron expelled from the H′ orbital could be shaken up to an unoccupied atomic level or shaken off into the continuum. The shake up signature is a peak at $E(H, H') \sim E(H) + E(H')$ while the shake off feature is a broad continuum. The following calculations for the second hole contributions have been carried out by De Rújula and Lusignoli in 2016 and they are published in [38] and by Faessler [39]. Even though the probability of a two hole process is much lower than the probability of single hole production, if the shape of the spectrum close to the end point is not known to analysts, it could lead to an erroneous result for Q and m_ν. However, given the latest measurement of Q=2.83 keV, the dangerous possibility that $E(H, H') \sim Q$ is excluded for any pair of holes. On the other hand, the large Q implies a smaller fraction of events in the region of interest, compared to the previous recommended value Q=2555±16 eV. There is reason to believe that the contribution of two hole states at energies lower than the end point could enhance the counting rate in the region of interest in an overwhelming way. The sector of the spectrum where two hole contributions become interesting is at energies above the M1 peak at E_c=2050 eV. As De Rújula and Lusignoli have stated that *though QED and weak interaction theory are well established to impressive levels of precision, dealing with atoms containing up to 67 electrons is not entirely straightforward*, I will make a brief overview of the state of the art as of 2016 of the studies of the spectral shape of ^{163}Ho.

3.1.2.1 Shake up

As Robertson pointed out, in an EC decay, not only a primary hole H is created, but there is a small probability of creating a second hole H′ in a shake up process. When the second electron is shaken up to any free orbital of energy negligible compared to $E_{tot} \sim E(H)+E(H')$, the measured calorimetric energy will peak at $E_c \sim E_{tot}$. In the approximation of no overlap of the two electron wave functions, it can be assumed that the width of the two hole state is the sum of the single partial widths $\Gamma_{tot} \simeq \Gamma(H) + \Gamma(H')$. It is then possible to evaluate the contribution of a particular two hole state to the calorimetric spectrum

$$\frac{dR[H, H']}{dE_c} = \kappa E_\nu p_\nu n_H n_{H'} BW[E_c, E_{tot}, \Gamma_{tot}] \times \sum_{n=7}^{\infty} |1 - \Pi(H, H')\phi_H(0)A(H, H', n)|^2 \quad (3.7)$$

with $E_\nu = Q - E_c$ and $\kappa E_\nu = \frac{G_F^2}{4\pi^2}\cos^2\theta_C B_H |M|^2$ where M is the nuclear matrix element and $B_H - 1$ a correction for atomic exchange and overlap of the order of 10%; $n_{H'}$ being the occupancy of the H′ shell, $\phi_H(0)$ is the wave function at the origin of the captured electron at the origin, $A(H, H')$ is the probability amplitude for the excitation electron in H′ to an unoccupied S-wave bound state with principal quantum number n4, $\Pi(H, H')$ is the exchange operator for the two electrons that antisymmetrises the product and the factor BW is defined as

$$BW[E_c, E_H, \Gamma_H] = \frac{\Gamma_H}{2\pi} \frac{1}{(E_c - E_H)^2 + \Gamma_H^2/4} \quad (3.8)$$

From the two hole contributions spectrum it is possible to study the shape of the total spectrum at the end point, which is shown in Figure 3.3

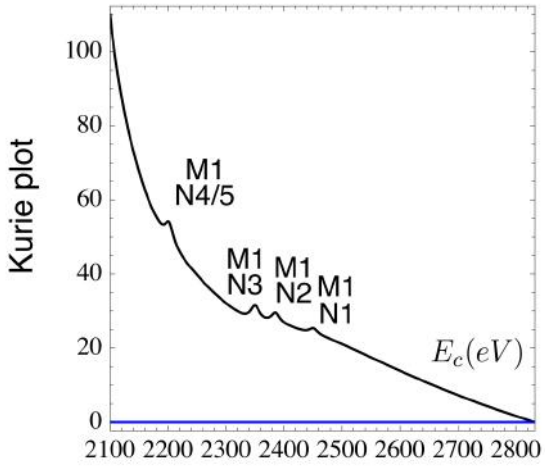

Figure 3.3: The theoretical calorimetric Kurie plot of the highest energy end of the spectrum with the two hole contribution.

3.1.2.2 Shake off

There is the chance for the second electron H' to be shaken off to an unbound state in the continuum rather than to a bound state of the decaying atom

$$Ho \longrightarrow Dy[H, H'] + e^- + \nu_e \tag{3.9}$$

The neutrino energy E_ν and the electron kinetic energy T_e are such that $E_\nu + T_e = Q - E_{tot}$ and the calorimetric energy is $E_c = T_e + E_{tot}$

Let $|Ho[H]\rangle$ be the wave function [40], in Ho, of the orbital from which the electron is captured and $|Dy[H, H'; p_e]\rangle$ the continuum wave function of the electron shaken off the daughter two-hole Dy ion. In the sudden limit the shake off distribution in electron momentum p_e or in its energy T_e can be estimated from the square of the wave function overlap:

$$\frac{dM}{dp_e} \equiv |\{1 - \Pi(H, H')\}\,\phi_H(0)\,\langle Ho[H']|Dy[H, H'; p_e]\rangle|^2, \tag{3.10}$$

$$\frac{dM}{dT_e} = \frac{m_e}{p_e}\frac{dM}{dp_e}, \tag{3.11}$$

It is easier to analyse the decay from the Equation 3.9 using the approximation of non vanishing width of the daughter holes [41], which leads to

$$\frac{dR}{dT_e} = \kappa\, E_\nu\, p_\nu\, n_H\, n_{H'}\, \frac{p_e}{4\pi^2}\, \frac{dM}{dT_e}. \tag{3.12}$$

The resulting E_c distribution is:

$$\frac{dR}{dE_c} = \int_0^{Q-E_{Tot}} \frac{dR}{dT_e}\,\delta(E_c - E_{Tot} - T_e)\,dT_e\,. \tag{3.13}$$

To take into account the non-zero-width, one has to substitute the above δ function with $BW[E_c - T_e, E_{Tot}, \Gamma_{Tot}]$.

Using the sudden approximation it is possible to calculate the probability of a M1 capture followed by a N1 shake off (M1N1c, o) process, which is the most relevant at the end point [38]. The starting point of the calculations is to consider the absent proton and the absent electron after the EC, as a perturbation to the Coulomb potential. It is then possible to write the matrix element for a shaken off electron at a given T_e

$$\frac{dM}{dT_e} = \frac{m_e}{4\pi^2 p_e} |\{1 - \Pi(M1, N1)\}\,\phi_{M1}(0) B_{off}(p_e)|^2 \tag{3.14}$$

with

$$B_{off}(p_e) \equiv \frac{\alpha}{E_{N1} + T_e} \int d^3r \phi^*(p_e, r)\phi_{N1}(r) b(r) \tag{3.15}$$

and

$$b(r) = \frac{1}{r} - \int d^3r \frac{|\phi_{M1}(r_1)|^2}{|\vec{r} - \vec{r_1}|} \tag{3.16}$$

is the perturbation to the Coulomb potential used for the calculation. As for the calculation the shape of dM/dT_e non relativistic wave functions have been used, leading to the spectrum for the 2800-1600 eV region shown in Figure 3.4

Preliminary data from Echo [42] and NuMECS [43] have been used for testing the agreement of the theory. In the ECHo data, a peak is present in the expected position of a contribution from N1 capture and O1 shake up and in both experiments there is evidence of a shoulder above the theoretical predictions for the region 480 eV $< E_c <$ 550 eV. It is rather complicate to accommodate all the observed features within a theoretical model without modifying the single peak contribution by factors of ~ 3. At the moment the predictions of the subdominant spectral features due to two hole phenomena are to be taken with precaution.

Besides the above mentioned calculations, there is also recent work by Faessler et al. [39], who calculated the wave functions of Ho and Dy* selfconsistently with the antisymmetrized relativistic Dirac-Hartree-Fock approach, unlike the screened non-relativistic wave functions used by De Rújula; Faessler results disagree with De Rújula's: the conclusion in [39] is that the shake-off contributions, calculated for the different 2-hole states are about two orders of magnitude smaller than the one-hole states. The shake-off spectrum can hardly be seen on such a scale in the total spectrum. Compared to the one-hole peaks it is at least two orders smaller. Briefly this work shows that one has not to worry about the shake-off process in the determination of the neutrino mass from electron capture in ^{163}Ho.

It is of crucial importance to gather experimental data in order to provide theorists a solid input for tuning the model of two hole production and provide a solid prediction for the spectral shape at end point, especially of the contribution of shake off, which may ultimately enhance the rate and hence the sensitivity to neutrino mass. This is indeed the prime physics goal of the HOLMES-32 measurement, which will be performed in 2017.

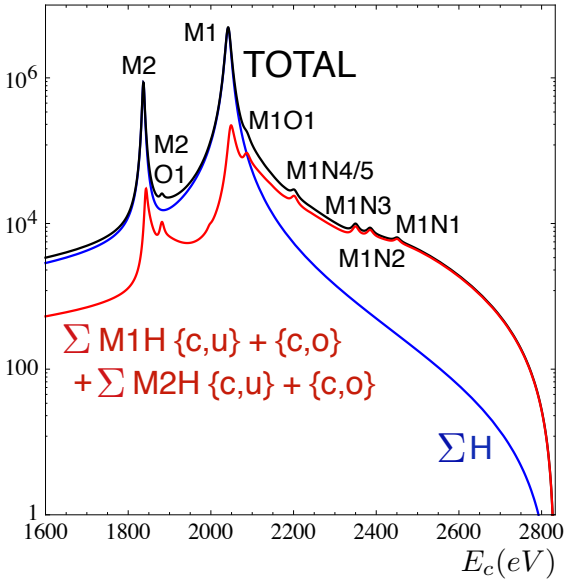

Figure 3.4: The theoretical calorimetric spectrum in the M region from [38]. In blue single-hole contribution ΣH are plotted. In red the two-hole shake-up plus shake-off contributions, with one of the holes being M1 or M2 are shown. In black, the sum of all contributions.

PART II

HOLMES, AN EXPERIMENT FOR A DIRECT SEARCH OF NEUTRINO MASS

Chapter 4

HOLMES

In the following chapter I will describe HOLMES, the core of my PhD programme. HOLMES ultimately aims at performing a measurement of the neutrino mass with a sensitivity as low as 1 eV. Even though is not directly competitive compared to KATRIN, HOLMES will set the grounds for future larger scale experiments with sub-eV sensitivity. I will outline all the tasks that have to be undertaken before the embedding of the isotope in the detectors absorbers, which namely are the isotope production and purification and the metallisation in order to produce the target that will be finally used for implantation.

4.1 Sensitivity goal

For years, laboratory experiments based on the study of proper nuclear processes have been used to directly measure the neutrino masses. In particular, single beta decay has been, historically, the traditional and most direct method to investigate the electron (anti)neutrino mass. In 1982 the use of the EC decay of ^{163}Ho was proposed as an alternative to single beta decay to be used in a calorimetric experiment. ^{163}Ho decays by EC to ^{163}Dy with a half life of about 4570 years and with the lowest known Q-value, which allows captures only from the M shell or higher. Because of the high specific activity of ^{163}Ho (about 2×10^{11} ^{163}Ho nuclei give one decay per second) the calorimetric measurements can be achieved by introducing relatively small amounts of 163 Ho nuclei in a calorimetric detector. Since the isotope quantity can be easily accommodated in the detectors absorber, the only physical constraint on the design of the detector itself come from the containment of the de-excitation radiation and on the dynamical parameters for an optimal detection. When measuring the energy emitted by an EC decaying isotope such as ^{163}Ho with a calorimetric detector, all the energy released in the decay is detected. The information on neutrino mass is carried in the upper end of the spectrum, just as in a single beta decay. In the EC capture spectrum the neutrino mass term appears in the phase factor, which is the same as in a single beta decay, with the total deexcitation energy E_c replacing the kinetic energy of the electron E_e . The de-excitation energy E_c is the total energy released by all the atomic transitions, subsequent to the capture of the electron, that fill the vacancy left by the EC process. Electrons with energies up to about 2 keV are most likely to be emitted (the fluorescence yield is less than 10^{-3}) [33].

The calorimetric spectrum appears as a series of lines at the ionization energies E_i of the captured electrons. These lines have a natural width of a few eV and therefore the actual spectrum is a continuum with marked peaks with Breit–Wigner shapes. The distribution in de-excitation (calorimetric) energy E_c is

$$\frac{d\lambda_{EC}}{dE_c} = \frac{G_\beta^2}{4\pi^2}(Q-E_c)\sqrt{(Q-E_c)^2-m_\nu^2}\times \sum_i n_i C_i \beta_i^2 B_i \frac{\Gamma_i}{2\pi}\frac{1}{(E_c-E_i)^2+\Gamma_i^2/4}, \quad (4.1)$$

where $G_\beta = G_F \cos\theta_C$ (with the Fermi constant G_F and the Cabibbo angle θ_C), E_i is the binding energy of the i-th atomic shell, Γ_i is the natural width, n_i is the fraction of occupancy, C_i is the nuclear shape factor, β_i is the Coulomb amplitude of the electron radial wave function (essentially, the modulus of the wave function at the origin) and B_i is an atomic correction for electron exchange and overlap. The spectrum with no processes arising from second order effects is shown in Figure 4.1

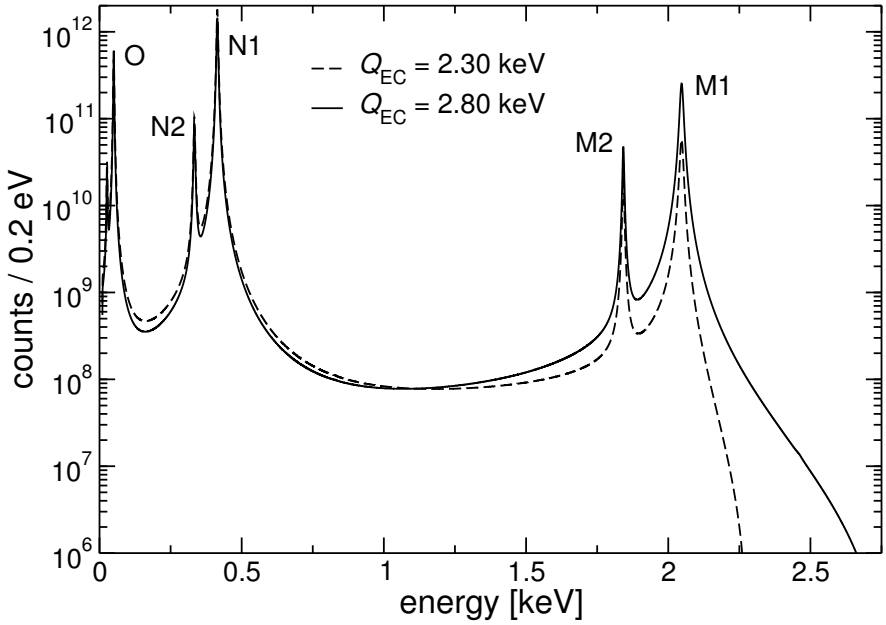

Figure 4.1: ^{163}Ho total absorption spectrum calculated for an energy resolution ΔE_{FWHM} = 1,eV

The sensitivity to neutrino mass depends on the fractions of events with energy close to the end point, which is dependent on the actual Q-value. The closer the Q-value of the decay to one of the E_i, the larger the resonance enhancement of the rate near the end-point, where the neutrino mass effect is relevant. The resulting functional dependence of the end-point rate on the Q-value for the EC case is steeper than the $1/Q^3$ one observed for beta decay spectra.

The enhancement of the number of events at the end point of the EC decay spectrum of ^{163}Ho sets it as the ideal isotope for a future direct neutrino mass measurement experiment that would allow to push the sensitivity to neutrino mass below 1 eV. HOLMES will

set an important milestone towards an eventual sub eV scale experiment, thanks to the its technological and physics measurements breakthroughs.

HOLMES aims at reaching a 1 eV sensitivity on neutrino mass. At the time of the initial proposal there was a relatively large uncertainty on the Q-value of the transition within an interval ranging from 2.3 keV to 2.8 keV. Recent measurements of the mass difference between ^{163}Ho and ^{163}Dy performed with a Penning trap mass spectrometer by Eliseev et al [30] shifted the Q-value to 2.833 $\pm$30(stat)$\pm$15(sys) keV. The mass difference result worsens the perspectives for any neutrino mass measurement with ^{163}Ho, yet there still are second order processes to be considered, such as shake off, that could eventually enhance the event rate at the end point.

Monte Carlo simulations have been performed by Nucciotti in [44] in order to address the sensitivity of a calorimetric experiment for a direct mass measurement. From these simulations it is possible to set the target for HOLMES and hence the performance to be matched by the detectors can be established. It is a major concern to establish the number of events to be gathered around the end point in order to determine the quantity of ^{163}Ho needed for a three year long experiment.

This issue was adressed using a frequentist Monte Carlo code that consists in the simulation of the spectra that would be measured by a large number of experiments carried out in a given configuration. The spectra are then fit as the real ones and the statistical sensitivity is deduced from the distribution of the obtained m_ν^2 parameters. This method is extremely powerful since it allows to include all relevant experimental effects, such as energy resolution, pile-up and background, which are the main concerns while designing a calorimeter for a high rate measurement.

The parameters describing the experimental configuration are the total number of ^{163}Ho decays N_{ev}, the FWHM of the Gaussian energy resolution ΔE_{FWHM}, the fraction of unresolved pile-up events f_{pp} and the radioactive background B(E). The total number of events is given by

$$N_{ev} = N_{det} \cdot A_{EC} \cdot t_M \tag{4.2}$$

with N_{det} being the total number of detectors, A_{EC} the EC decay rate in each detector and t_M the live time of the measurement.

The pile-up fraction f_{pp} can be evaluated as $f_{pp} = \tau_R \cdot A_{EC}$ with τ_R being the time resolution of the detector. Pile-up occurs when two events occur within a time interval shorter than the time resolution of the detector. Pile-up is a serious issue because the pile-up events are the main contribution to background at the end point since the pile-up spectrum can be estimated from the convolution of the EC decay spectrum with itself. The pile-up spectrum is a superposition of several peaks and it reaches energies up to 2·Q-value.

The $B(E)$ function is usually taken as a constant $B(E) = bT$, where b is the average background count rate for unit energy and for a single detector, and $T = N_{det} \times t_M$ is the experimental exposure.

$$\begin{aligned} S(E_c) &= [N_{ev}(N_{EC}(E_c, m_\nu) + f_{pp} \times & (4.3)\\ &\quad N_{EC}(E_c, 0) \otimes N_{EC}(E_c, 0)) + B(E_c)] \otimes R_{\Delta E}(E_c) & (4.4) \end{aligned}$$

The theoretical spectrum $S(E_c)$ used in the generation of the toy experiments is the sum of the primary decay spectrum and the pile-up spectrum multiplied by the detector response

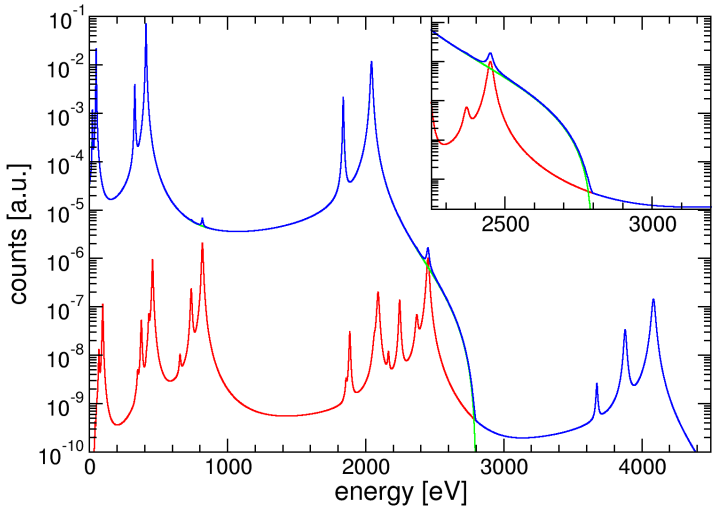

Figure 4.2: Full ^{163}Ho decay experimental spectrum simulated for $Q = 2200$ eV, $N_{ev} = 10^{14}$, $f_{pp} = 10^{-6}$, $\Delta E_{FWHM} = 2$ eV, $m_\nu = 0$. The bottom curve is a fit of the pile-up spectrum. The insert shows the end-point region of the spectrum.

$R_{\Delta E}(E_c)$, which is assumed to be gaussian

$$R_{\Delta E}(E_c) = \frac{1}{\sigma\sqrt{2\pi}} e^{-\frac{E_c^2}{2\sigma^2}} \tag{4.5}$$

with standard deviation $\sigma = \Delta E_{FWHM}/2.35$.

In order to asses the sensitivity of the calorimetric experiment, a set of toy Monte Carlo simulations was performed. Each toy experiment measured a theoretical spectrum $S(E_c)$, shown in Figure 4.2. The set of simulated spectra (between 100 and 1000) are obtained by fluctuating $S(E)$ according to Poisson statistics. Each spectrum was fitted using equation 4.1 with m_ν^2, Q, N_{ev}, f_{pp} and b as free parameters. For the simulations, the E_i, Γ_i, n_i, C_i, B_i, and β_i in 4.3 are taken from [45] and shown in Tables 4.1 and 4.2.

Level	E_i [eV]	Γ_i [eV]
M1	2047	13.2
M2	1842	6.0
N1	414.2	5.4
N2	333.5	5.3
O1	49.9	
O2	26.3	

Table 4.1: Energy levels of the captured electrons, with their widths, for ^{163}Dy

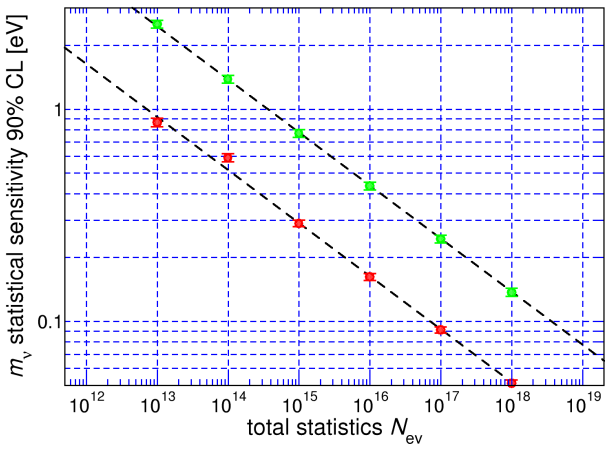

Figure 4.3: ^{163}Ho decay experiments statistical sensitivity dependence on total statistics N_{ev} with ΔE_{FWHM}=1 eV, $f_{pp} = 10^{-5}$, and $b = 0$ count/eV/s/detector.

Level	Ratio
M2/M1	0.0526
N1/M1	0.2329
N2/M1	0.0119
O1/M1	0.0345
O2/M1	0.0015
P1/M1	0.0021

Table 4.2: Electrons squared wave functions at the origin β_i^2 relative to β_{M1}^2

During the HOLMES data taking special high statistics measurements will be performed in order to asses the atomic parameters describing the Breit-Wigner peaks. For the determination of the neutrino mass it is correct to leave free the parameters relative to the M1 peak. From a more complex versions of the simulations leaving position E_{M1}, width Γ_{M1}, and relative intensity free it was seen that the sensitivity to neutrino mass with this approach would be less 10 % worse. The details of the Monte Carlo simulation can be found in [44]: each fit of the toy experimental spectra is performed between 1500 eV and 3500 eV. The simulations were performed for Q-s ranging from 2200 eV to 2800 eV. The first result is the dependence of the sensitivity on the number of the gathered statistics, as shown in Figure 4.3.

From the simulation the total number of events needed for reaching 1 eV sensitivity on neutrino mass was calculated: HOLMES will need to record 10^{13} events during its three year long data taking. In order to gather the desired N_{ev}, the detectors and the readout will need to satisfy stringent requirements, which will be explained in the following paragraphs.

4.1.1 Experimental requirements

From the simulations we can understand the importance of experimental parameters such as energy resolution and unresolved pile-up fraction, therefore setting the detector design and performance. From the simulations we see that the sensitivity on neutrino mass is not strongly dependent on the effective energy resolution, but rather on the pile-up fraction. In the left graph shown in Figure 4.4 the sensitivity is plotted as a function of the pile-up fraction for constant energy resolution, while in the right graph of Figure 4.4 the sensitivity is plotted as a function of ΔE_{FWHM} for constant pile-up fraction.

It is clear that pile up plays a more crucial role compared to an eventual loss of energy resolution in reaching a better sensitivity. Qualitatively this latter effect can be understood in the following way: as the pile-up increases and takes over the signal at Q, the significant interval for the fit broadens, hence the energy resolution weights less. However, it is worth noting that the time resolution depends on the detector signal-to-noise ratio at high frequency and therefore at constant bandwidth - that is at constant detector rise time - an energy resolution deterioration unavoidably turns in a worse time resolution. This effect it is not considered in the simulation.

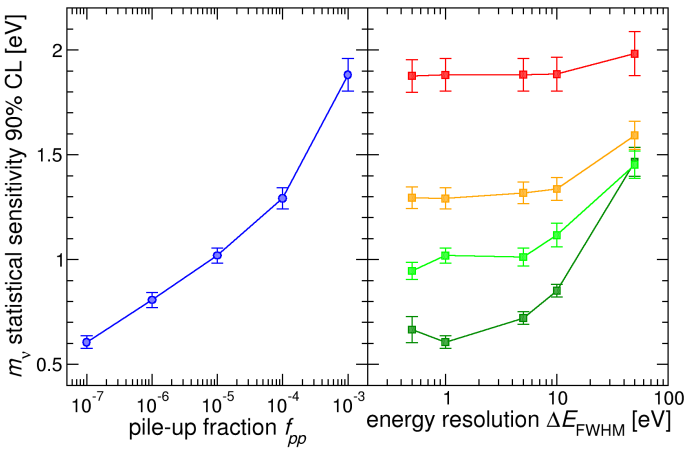

Figure 4.4: ^{163}Ho decay experiments statistical sensitivity dependence on pile-up fraction f_{pp} and energy resolution ΔE_{FWHM} for $Q = 2.83$ keV, $N_{ev} = 10^{14}$, and $b = 0$ count/eV/s/detector. Left: Energy resolution is fixed to $\Delta E_{FWHM} = 1$ eV. Right: Pile-up fraction taken as (from bottom to top) $f_{pp} = 10^{-7}$, 10^{-5}, 10^{-4}, and 10^{-3}.

It is worth noticing that since the sensitivity on m_ν is so strongly dependent on the total acquired statistics, in a real experiment with a fixed experimental exposure T and with a finite number of detectors with finite performance f_{pp} and ΔE_{FWHM} it is more convenient to keep the single detector activity A_{EC} as high as possible. It is clear that a limitless activity can not be pursued due to the effect of ^{163}Ho in the absorber lattice or due to cross-talk and dead time considerations. For instance, in a calorimetric experiment, embedding enough

^{163}Ho atoms that would allow to reach activities of the order of $A_{EC} = 300$ decays/s is feasible without enlarging the absorber, causing a degradation in performance. There are some issues that simulations cannot assess though, and need to be addressed experimentally, such as the thermal capacity variation of the detectors after the implantation process. Even though the implantation process was designed to simultaneously sputter Gold while implanting the ^{163}Ho in order to limit the local concentration of ^{163}Ho atoms, it will be necessary to perform a special cryogenic measurement in order to check that the detector performances have remained unchanged after the implantation process. The possibility of an excess of heat capacity in the absorber of the detectors will be investigated before the implantation by measuring some especially designed detectors with extra heat capacity.

4.1.1.1 Effect of background

Because of the very low fraction of decays in the region of interest close to Q, the background may be a critical issue in end-point neutrino mass measurements. The Monte Carlo simulations here are done with the hypothesis of a constant background b. A constant background is negligible as long as it is much smaller than the pile-up spectrum, that is when $b \ll A_{EC} f_{pp}/2Q$. Figure 4.5 confirms this simple considerations and shows that this is another good reason to have detectors with the highest possible activity. For large activities and correspondingly large pile-up rate, experiments should be relatively insensitive to cosmic rays and to environmental radioactivity. In a typical experiment with low temperature microcalorimenters, detectors have a sensitive area exposed to cosmic rays of the order of $10^{-8}\,m^2$ and a thickness of few micrometers: at sea level this translates in a cosmic ray interaction rate of about one per day with an average energy deposition of 10 keV, which, in turns, means $b \lesssim 10^{-4}$ count/eV/day/detector. All the above considerations should be complemented with an analysis of the effect of contaminations in the bulk of the detector – especially β and EC decaying isotopes – and of the fluorescent X-ray and Auger emission from the material closely surrounding the detectors. The ^{163}Ho isotope production and its detector embedding are also likely to add radiactive contaminants internal to the detector: one example of dangerous isotope is ^{166m}Ho (β decay, $Q_\beta = 1854$ keV, $\tau_{1/2} = 1200$ year) which is produced together with ^{163}Ho in many of the production routes which have been proposed [46].

In order to separate any possible contaminants from the enriched ^{163}Ho before the embedding process in the detectors, several purification steps are required. In the following paragraphs an overview of the processes that will lead to the final implantation process is given.

The results of the simulations are the starting point from which design a suitable detector for a high statistics and high rate neutrino mass measurement.

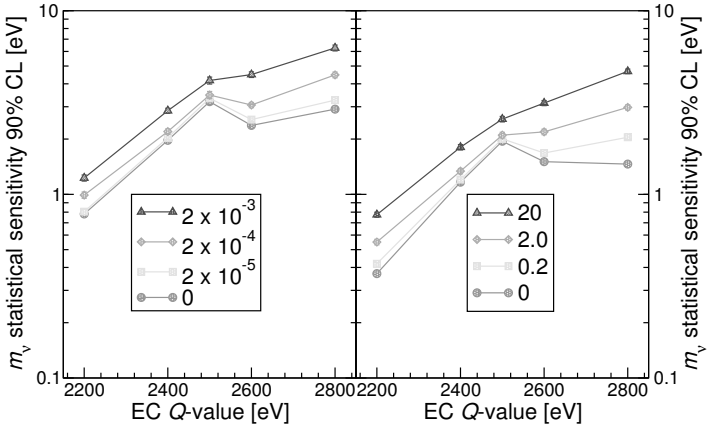

Figure 4.5: Effect of background on statistical sensitivity for $N_{ev} = 10^{14}$ and $\Delta E_{FWHM} = 1$ eV. Left: $A_{EC} = 3$ Hz/det and $f_{pp} = 3 \times 10^{-6}$, Right: $A_{EC} = 300$ Hz/det and $f_{pp} = 3 \times 10^{-3}$. The background levels in the boxes are in count/eV/day/detector units.

t

Chapter 5

TES for neutrino mass measurement

In the previous chapter I have described the necessary processes before the embedding process of ^{163}Ho in the absorber of a low temperature calorimeter. In the next chapter I will describe the detectors that will perform the HOLMES measurement. The Transition Edge Sensors are based on a well established technology and currently are the most promising detectors that meet the stringent requirements set by HOLMES in terms of speed, energy resolution and multiplexing capability. In the latter part of the chapter I will indeed describe the rf-SQUID and the multiplexing system that will allow us to read as many as 1000 detectors operated at ~60 mK.

5.1 Transition Edge Sensors

In the last decades superconducting Transition Edge Sensors (TES) have emerged as a very powerful tools for high resolution detection of photons with energies ranging from mm wavelength to gamma rays. The TES is a thermal sensor that measures an energy deposition in a coupled absorber by the increase of resistance of a superconducting film biased within the superconducting to metal transition. A proper and detailed description of superconductive films used as temperature sensors can be found in the chapter by Irwin and Hilton in [47].

The feature that makes the TES such an interesting device is the very steep dependence of the resistance on temperature during the transition phase. For instance, the logarithmic sensitivity $\alpha = \frac{dlogR}{dlogT}$ can be two orders of magnitude more sensitive compared to a semiconductor thermistor. Being such a sensitive device much care has to payed in design and fabrication in order to prevent detector instability during operation and in order to obtain a high enough saturation energy that allows to measure thermal signals keeping the superconductor within the transition.

In the last two decades, the use of superconducting quantum interference device (SQUID) coupled to TES has open the way to a very wide application of large TES array; the SQUID is a current amplifier which can be easily impedance-matched to the small resistance of the TES. In the following paragraphs I will make a very brief introduction to superconductors and I will derive the equations for small signal in a TES following the approach by Irwin.

5.1.1 Superconductors

Superconductivity is a phenomenon that occurs in s material when electrons bind in *Cooper* pairs acting like a 0 spin boson instead of a 1/2 spin fermion. Being in a bound state state allows the electrons to move freely through the lattice without any scattering on ions, hence with no resistance. The binding energy is due indeed to the phonon mediated interaction of the electrons with the positive ions in the lattice. The size of the wave function of a Cooper pair is called coherence length, and for zero temperature its value is $\xi(0) \approx 0.18 v_F/(k_B T_c)$. At temperature above the transition temperature T_c, thermal energies of the order of $k_B T$ spontaneously break Cooper pairs so that the transition temperature T_c is related to the energy gap E_{gap} by $E_{gap} = 2\Delta(0) \approx 3.5 k_B T_c$. In addition to zero resistivity superconductors show also a screening effect to magnetic fields inside the superconductive, called the Meissner effect. An external magnetic field is exponentially attenuated by the Cooper pairs supercurrent it induces in the material with an effective penetration depth $\lambda_{eff}(T)$.

Superconductors are classified according to the Ginzburg-Landau dimensionless parameter $\kappa \equiv \lambda_{eff}(T)/\xi(T)$; if $\kappa < 1/\sqrt{2}$ the superconductor is of Type I and the free energy is minimised when the magnetic flux penetrating the material clumps together; while if $\kappa > 1/\sqrt{2}$, the superconductor is of Type II and the magnetic flux inside the materials separates into single flux quanta $\Phi_0 = h/2e = 2.0678 \times 10^{-15}$ Wb that repel each other. Commonly, TESs used for X-ray detection are Type I superconductors.

5.1.2 TES response to a thermal signal

In order to understand the response of a TES to a thermal variation it is useful to define some variables.

$$\alpha_I \equiv \left.\frac{\partial \log R}{\partial \log T}\right|_{I_0} = \left.\frac{T_0}{R_0}\frac{\partial R}{\partial T}\right|_{I_0} \tag{5.1}$$

$$\beta_I \equiv \left.\frac{\partial \log R}{\partial \log I}\right|_{T_0} = \left.\frac{I_0}{R_0}\frac{\partial R}{\partial I}\right|_{T_0} \tag{5.2}$$

$$\tag{5.3}$$

When coupled to a SQUID a TES is usually biased at constant voltage, in order to reduce the loading effects due to extra current flowing in the TES branch, that increase the relative noise of the SQUID and, most important, to provide negative electro-thermal feedback. This is achieved by connecting a resistance R_{SH} called the *shunt* in parallel to the TES branch of the bias circuit in order to connect several TESs in series, as shown in Figure 5.2

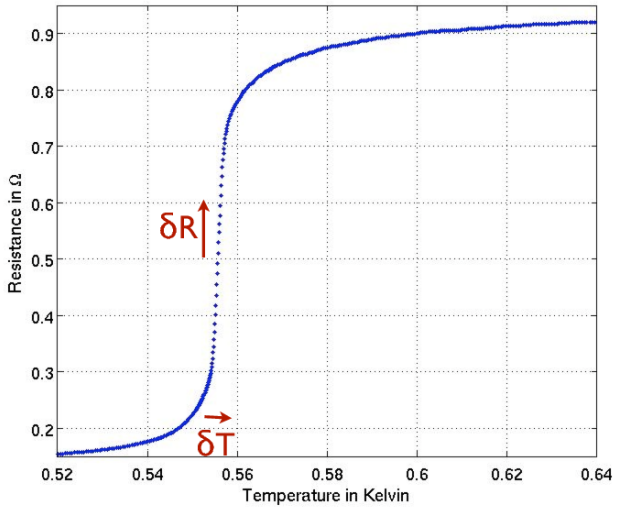

Figure 5.1: Example of a TES resistance vs temperature transition

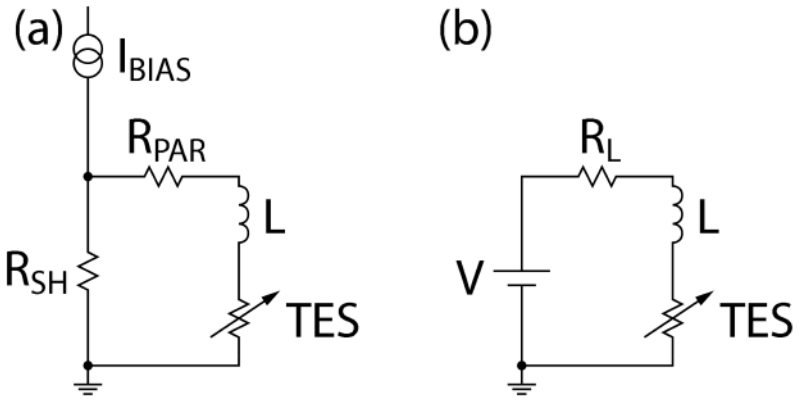

Figure 5.2: TES input circuit and its Thevenin equivalent. (**a**) bias current $\mathrm{I_{bias}}$ flows through the shunt resistor $\mathrm{R_{SH}}$ in parallel with a parasitic resistance $\mathrm{R_{PAR}}$, and inductance L which accounts both for the SQUID and the stray inductance, and a TES. (**b**) The Thevenin equivalent of the circuit in (**a**); a bias $V = \mathrm{I_{BIAS}} \mathrm{R_{SH}}$ is applied to a load resistor $\mathrm{R_L} = \mathrm{R_{SH}} + \mathrm{R_{PAR}}$, the inductance L and the TES.

The response of the TES is obtained by solving the two coupled differential equations for the thermal and the electrical circuit in order to obtain the time dependence of T and I.

Ignoring the noise terms, the thermal equation is

$$C\frac{dT}{dt} = -P_{bath} + P_j + P \tag{5.4}$$

where C is the heat capacity of the TES and the coupled absorber, T is the temperature of the TES, P_{bath} is the power flowing from the TES to the thermal bath, P_J is the Joule dissipation and $P(t)$ is the signal power due to an eventual energy deposition. For the power flow toward the heat sink, we assume a power dipendence

$$P_{bath} = K(T^n - T_{bath}^n) \tag{5.5}$$

where $n = \beta + 1/\beta$ and $K = G/n(T^{n-1})$

Ignoring any noise power spectrum, the electrical differential equation becomes:

$$L\frac{dI}{dt} = V - IR_L - IR(T, I) \tag{5.6}$$

where L is the inductance, V is the Thevenin equivalent bias voltage, I is the electrical current through the TES and $R(T, I)$ is the resistance of the TES. The two equations are complicated by several non linear terms which depend on both resistance and temperature. These terms can be linearised by applying a small signal limit around the steady state values of resistance, temperature and current: R_0, T_0, I_0. In the small signal limit we use the steady state values of C, and thermal conductance G. We will describe the linearisation of the power flow towards the heat sink, the non linear TES resistance and the Joule power dissipation, and therefore derive the linear form of the above differential equations.

In order to study the system response to small signals we need to expand the variables with respect to small variation $\delta T \equiv T - T_0$ and $\delta I \equiv I - I_0$. Equation 5.5 can be expanded

$$P_{bath}(T) \approx P_{bath}|_{T_0} + G\delta T \tag{5.7}$$

The TES resistance can be expanded around R_0, T_0 and I_0 to first order

$$R(T, I) \approx R_0 + \left.\frac{\partial R}{\partial T}\right|_{I_0} \delta T + \left.\frac{\partial R}{\partial I}\right|_{T_0} \delta I \tag{5.8}$$

and the expression for the resistance can be written as

$$R(T, I) \approx R_0 + \alpha_I \frac{R_0}{T_0}\delta T + \beta_I \frac{R_0}{I_0}\delta I \tag{5.9}$$

The Joule power can be expanded also

$$P_J = I^2 R \approx P_{J_O} + 2I_0 R_0 \delta I + \alpha_I \frac{P_{J_0}}{T_0}\delta T + \beta_I \frac{P_{J_0}}{I_0}\delta I \tag{5.10}$$

and we can also define the low frequency loop gain under constant current

$$\mathscr{L}_I \equiv \frac{P_{J_0}\alpha_I}{GT_0} \tag{5.11}$$

and the natural thermal time constant in non feedback regime

$$\tau \equiv \frac{C}{G} \tag{5.12}$$

We can finally write the linear differential equations by substituting 5.7, 5.9, 5.10 and 5.12 into 5.6 and 5.4, substitute the small signal values $\delta T \equiv T - T_0$ and $\delta I \equiv I - I_0$ and we get

$$\frac{d\delta I}{dt} = -\frac{R_L + R_0(1+\beta_I}{L}\delta I - \frac{\mathscr{L}_I G}{I_0 L}\delta T + \frac{\partial V}{L} \tag{5.13}$$

$$\frac{d\delta T}{dt} = -\frac{I_0 R_0(2+\beta_I)}{C}\delta I - \frac{1-\mathscr{L}_I}{\tau}\delta T + \frac{\partial P}{C} \tag{5.14}$$

and $\partial P \equiv P - P_0$ represents the small power signals that move the system around the steady state power load P_0, and $\partial V \equiv V_{bias} - V_0$ represents the small voltage changes around V_0. There are some limit cases in which the equations become simpler; in the limit for $\mathscr{L}_I = 0$ 5.13 decouples from δT and integrating it we find the exponential decay of current to steady state with the bias circuit time constant

$$\tau_{el} = \frac{L}{R_L + R_0(1+\beta_I)} \tag{5.15}$$

The differential equations 5.13 and 5.14 can be solved with a variable substitution in order to diagonalise the matrix hence decoupling the two equations. Once the equations are decoupled they can be integrated and solutions in form of exponential functions cna be found; the solutions can be re-written in function of T and I. substituting in 5.14, 5.13 and 5.15 we can write the matrix form of the differential equation

$$\frac{d}{dt}\begin{pmatrix}\delta I\\ \delta T\end{pmatrix} = -\begin{pmatrix}\frac{1}{\tau_{el}} & \frac{\mathscr{L}G}{I_0 L}\\ -\frac{I_0 R_0(2+\beta_I)}{C} & \frac{1}{\tau_I}\end{pmatrix}\begin{pmatrix}\delta I\\ \delta T\end{pmatrix} + \begin{pmatrix}\frac{\delta V}{L}\\ \frac{\delta P}{C}\end{pmatrix} \tag{5.16}$$

Integrating we find the homogeneous solutions

$$\begin{pmatrix}\delta I\\ \delta T\end{pmatrix} = A_+ e^{-\lambda_+ t}\mathbf{v}_+ + A_- e^{-\lambda_- t}\mathbf{v}_- \tag{5.17}$$

with the $A_\pm$ are unitles constants. The two eigenvalues are

$$\frac{1}{\tau_\pm} \equiv \lambda_\pm = \frac{1}{2\tau_{el}} + \frac{1}{2\tau_I} + \frac{1}{2}\sqrt{\left(\frac{1}{\tau_{el}} - \frac{1}{\tau_I}\right)^2 - 4\frac{R_0}{L}\frac{\mathscr{L}_I(2+\beta_I)}{\tau}}s \tag{5.18}$$

with $\tau_\pm$ as the inverse eigenvalues. The two eigenvectors are

$$\mathbf{v}_\pm = \begin{pmatrix}\frac{1-\mathscr{L}_I-\lambda_\pm\tau}{2+\beta_I}\frac{G}{I_0 R_0}\\ 1\end{pmatrix} \tag{5.19}$$

The interesting result is the solution for a delta like impulse, which describes the detector response to an energy deposition from a photon interaction. Within this approximation, we

can calculate the $A_\pm$ factors using the condition $\delta T(0) = \Delta T = E/C$ and the initial current $\delta I(0) = 0$.

$$\begin{pmatrix} 0 \\ \Delta T \end{pmatrix} = A_+ e^{-\lambda_+ t}\mathbf{v}_+ + A_- e^{-\lambda_- t}\mathbf{v}_- \tag{5.20}$$

from which we can calculate the coefficients

$$A_\pm = \pm \Delta T \frac{\frac{1}{\tau_I} - \lambda_\mp}{\lambda_+ - \lambda_-} \tag{5.21}$$

Substituting the coefficients in the solution equation and using the time constants $1/\tau_\pm \equiv \lambda_\pm$

$$\delta I(t) = \left(\frac{\tau_I}{\tau_+} - 1\right)\left(\frac{\tau_I}{\tau_-} - 1\right)\frac{1}{(2+\beta_I)}\frac{C\Delta T}{I_0 R_0 \tau_I^2}\frac{\left(e^{-t/\tau_+} - e^{-t/\tau_-}\right)}{(1/\tau_+ - 1/\tau_-)} \tag{5.22}$$

$$\delta T(t) = \left(\left(\frac{1}{\tau_I} - \frac{1}{\tau_+}\right)e^{-t/\tau_-} + \left(\frac{1}{\tau_I} - \frac{1}{\tau_-}\right)e^{-t/\tau_+}\right)\frac{\Delta T}{(1/\tau_+ - 1/\tau_-)} \tag{5.23}$$

From the mathematical form of the current response $\delta I \propto (e^{-t/\tau_+} - e^{-t/\tau_-})$ we can identify the time constants as the rise time τ_+ and the fall time τ_- of the pulse arising from a delta function like interaction. The case of $\tau_+ \ll \tau_-$ which occurs when the inductance L is small, is interesting because $\tau_\pm$ are limited by the operational parameters of the system

$$\tau_- \rightarrow \tau_{el} \tag{5.24}$$

$$\tau_+ \rightarrow \tau \frac{1 + \beta_I + R_L/R_0}{1 + \beta_I + R_L/R_0 + (1 - R_L/R_0)(L)} = \tau_{eff} \tag{5.25}$$

which are the electrical time constant and the effective thermal constant of the detector.

An interesting case is *critical damping*, which is achieved when $\tau_- = \tau_+$. The expression 5.22 becomes

$$\delta I(t) = \left(\frac{\tau_I}{\tau_\pm} - 1\right)^2 \frac{1}{(2+\beta_I)}\frac{C\Delta T}{I_0 R_0 \tau_I^2}\left(-te^{-t/\tau_\pm}\right) \tag{5.26}$$

This is a common way to optimise the trade-off between energy resolution or noise power and a sufficiently slow pule rising edge compatible with the effective sampling rate of read-out electronics. We can also calculate the current responsivity of the TES, which will be used in the evaluation of the noise of the detector, from the the solution

$$s_I(\omega) = -\frac{1}{I_0 R_0}\frac{1}{(2+\beta_I)}\frac{(1 - \tau_+/tau_I)}{(1 + i\omega\tau_+)}\frac{(1 - \tau_-/tau_I)}{(1 + i\omega\tau_-)} \tag{5.27}$$

5.1.3 Regime of operation

The stable operation at high $\mathscr{L}_I$ was the reason for introducing the constant bias of the TES. I will briefly show the constraints on the design parameters in order to to ensure a stable operation of the TES. If the time constants $\tau_\pm$ in 5.18 are real, the solution of 5.22 is purely exponential with no oscillating terms and it is called damped or overdamped. The response of the calorimeter is overdamped at $\tau_+ < \tau_-$ and critically damped if $\tau_+ = \tau_-$.

Since the inductance in the bias circuit determines the regime of operation, in order to have real time constants, we must set constraints on the inductance. We solve the critical damping case 5.18 for the inductance:

$$L_{crit\pm} = \left\{ \mathscr{L}_I \left(3 + \beta_I - \frac{R_L}{R_0}\right) + \left(1 + \beta_I + \frac{R_L}{R_0}\right) \pm 2\sqrt{(L)_I(2+\beta_I)\left[(L)_I\left(1 - \frac{R_L}{R_0}\right) + \left(1 + \beta_I + \frac{R_L}{R_0}\right)\right]} \right\} \times \times \frac{R_0\tau}{((L)_I} \quad (5.28)$$

There are three regions of operation: for very large L the response of the calorimeter is overdamped; for $L_{crit_-} < L < L_{crit_+}$ the response is underdamped. The best regime for constant voltage bias operation is $L < L_{crit_-}$. At $L < L_{crit_-}$ the responsivity is maximum. In strong feedback regime with $\mathscr{L}_I \gg 1$ and $R_L = 0$, we can simplify the expression 5.28 to

$$\frac{L_{crit\pm}}{R_0} = \frac{\tau}{\mathscr{L}_I}\left(3 \pm 2\sqrt{2}\right) \quad (5.29)$$

The response of the calorimeter is then stable and tends to relax back to steady state over time if the real part of both time constants $\tau_\pm$ are positive. With this final constraint satisfied, from 5.15 we obtain

$$R_0 > \frac{((L)_I - 1)}{(\mathscr{L}_I + 1 + \beta_I)} R_L \quad (5.30)$$

which is the criterion for stability for an overdamped TES.

The constraints on the load resistor R_L values is necessary to prevent thermal runway due to the closed loop gain $\mathscr{L}_I > 1$. It is usually satisfied when $R_0 > R_L$.

5.1.3.1 Negative Electrothermal feedback

The thermal and electrical circuits of a TES interact due to equations 5.13 and 5.14. When operating large arrays of detectors, as HOLMES will, features like stability at high $\mathscr{L}_I$, reduced sensitivity to TES parameter variation, fast response time, self biasing and self calibration, become crucial. A strong electrothermal feedback at constant voltage bias is the proper operation method. A temperature signal in the TES is transduced into an electrical signal by the change in resistance of the TES. In turn, the electrical signal in the TES is fed back into a temperature signal by a reduction of Joule dissipation in the TES. This Electro Thermal Feedback (ETF) is the process that allows to run TES arrays. Under constant voltage bias condition i.e. $R_L \ll R$, with the increase of temperature and resistance, the Joule power $P_J = V^2/R$ decreases and the feedback is negative. When a TES is voltage biased, it is stable against thermal runaway even at high $\mathscr{L}_I$. As the temperature is increased, the drop in Joule power dissipation restores the working point. Most important, when used in large arrays, the voltage biased TES is self biased in temperature within the transition. If several pixels have superconductive transitions that do not overlap perfectly in temperature, it is possible to bias them all at the same temperature. If they are voltage biased and the bath temperature is much lower than the transition temperature, the Joule dissipation causes each chip to bias itself within the transition.

5.1.4 TES Noise

The TES is a very sensitive detector but, as a thermal detectors its resolution is limited by the thermodynamic fluctuations of its state variables. There are two main contributions to noise in a TES, the thermodynamic fluctuations of charge carriers in a resistance, known as Johnson or Nyquist noise and fluctuations arising from thermal impedance, which are referred as thermal fluctuation noise. When instead of the delta function we analyse the differential equation 6.7 and 6.6 with a stochastic signal due to correlated variations of I and T, the differential equations are called Langevin equations. These equations describe the response of the detector to random forces. The coupled equations can be analysed using the Fluctuation-Dissipation Theorem; it is necessary to properly identify the state variables and each conjugate force in order to proceed to a solution. The force associated with the current I state variable is the voltage V. If we imagine a resistor in a circuit with an inductance L with the circuit connected to a constant temperature bath, the fluctuations in the current will show a canonical (Gibbs) distribution. The free energy is the energy stored in the inductor $F = LI^2/2$; the conjugated momentum is $p = \partial F/\partial I = LI$ and the associated force $dp/dt = LdI/dt = V$. In the thermal analysis the temperature is the variable free to oscillate. In the thermal model the heat capacity of the TES is connected to a heath bath via a thermal conductance and heat is allowed to flow through the thermal link. When heat dQ flows, there is free energy change $dF = -SdT$ where S is the entropy, and $p = \partial F/\partial T = -S$ is the conjugated momentum; the conjugate force is $dp/dt = -(1/T)dQ/dT = -P/T$. Instead of the differential equation matrix used before we can write an impedance matrix $Z_{ext_{ij}}$ as in [47], that connects the state variable vector to the conjugate forces vector which accounts for the external forces

$$Z_{ext} = \begin{pmatrix} \left(\frac{1}{\tau_{el}} + i\omega\right) L & \frac{\mathscr{L}_I G}{T_0} \\ [-I_0 R_0(2+\beta_I)]\,\frac{1}{T_0} & \left(\frac{1}{\tau} + i\omega\right)\frac{C}{T_0} \end{pmatrix} \tag{5.31}$$

This expression does not include the internal voltage sources such as the power dissipation in the TES. In order to take into account the internal forces we need to write the internal impedance matrix

$$Z_{int} = \begin{pmatrix} \left(\frac{1}{\tau_{el}} + i\omega\right) L & \frac{\mathscr{L}_I G}{T_0} \\ [I(R_L - R_0) + I\omega L I_0]\,\frac{1}{T_0} & \left(\frac{1}{\tau} + i\omega\right)\frac{C}{T_0} \end{pmatrix} \tag{5.32}$$

with the coupled thermal electrical differential:

$$Z_{int,ext}\begin{pmatrix} I_\omega \\ T_\omega \end{pmatrix} = \begin{pmatrix} V_{int,ext_\omega} \\ \frac{P_\omega}{T_0} \end{pmatrix} \tag{5.33}$$

The impedance matrix determines the thermodynamic fluctuations of the state variables; any impedance linking a variable to a conjugate force causes correlation for every non zero matrix element. According to the fluctuation dissipation theorem, assuming to have small fluctuations, the power spectral density of the fluctuations in the u variable are

$$S_u(\omega) = 4k_B T Re[Y(\omega)] \tag{5.34}$$

where $Y(\omega) \equiv Z^{-1}(\omega)$. The source of these correlation can be modelised as a fictional random force F with power spectral density

$$S_F(\omega) = 4k_B T Re[Z(\omega)] \tag{5.35}$$

and the corresponding matrix form is

$$S_{u_i}(\omega) = 4k_B T Re[Y_{ii}(\omega)] \tag{5.36}$$

These predictions are not fully consistent with experimental results, that is because they were withdrawn from the initial hypothesis of thermodynamic equilibrium, which is not the case for a TES operating at a different temperature with respect to the thermal bath. In order to overcome this problem, an approximation by Mather [48] can be used: it states that the fictional random forces at equilibrium (at zero current) and with linear elements (with resistances non dependent from neither current or temperature) is the same as the fictional random forces responsible for the fluctuations in non linear resistors. This is equivalent to the well known model that associates the random voltage fluctuations across a resistor with spectral power density $S_V = 4k_B T/R$. At equilibrium, the real components of the terms in 5.33 are

$$Re[Z_{int}] = \begin{pmatrix} R_0 + R_L & 0 \\ 0 & \frac{G}{T_0} \end{pmatrix} \tag{5.37}$$

Then, applying the fluctuation dissipation theorem as before, the power spectral densities of the fictional forces are determined by the diagonal elements of the equilibrium impedance matrix 5.37

$$\begin{pmatrix} S_V \\ \frac{S_{P_{TFN}}}{T_0^2} \end{pmatrix} = 4k_B T_0 \begin{pmatrix} R_0 + R_L \\ \frac{G}{T_0} \end{pmatrix} \tag{5.38}$$

With $S_V = S_{V_{TES}} + S_{V_L}$ and, as stated before, the Nyquist voltage of the TES is $S_{V_{TES}} = 4k_B T_0 R_0$ and $S_{V_L} = 4k_B T_0 R_L$ is the Nyquist voltage of the load resistor and $S_{P_{TFN}} = 4k_B T_0^2 G$ is the noise fluctuation across the thermal link G. Yet, in this model we do not consider the temperature and current dependence of the resistance and second order processes of thermal conductance, such as phonon reflections. In order to include the current dependence we need to express

$$R_0 \equiv \frac{V}{I} = r + \frac{1}{2}\gamma I \tag{5.39}$$

with r being the value at which R_0 approaches for low current and γ is a non linearity factor. Hence we can write

$$\beta_I \equiv \frac{I}{R}\frac{dR}{dI} = \gamma \frac{1}{2R_0} \tag{5.40}$$

and the noise power spectrum is

$$S_V = 4k_B T R_0 [1 + 2\beta_I + \mathcal{O}(I^2)] \tag{5.41}$$

While for the thermal conductance, we need to add a multiplicative unitless factor $F(T_0, T_{bath}$ which typically ranges from 0.5 to 1 according to the thermal conductance exponent and

whether the phonon reflection from the boundaries is specular or diffuse. Its current expression including the non linearity terms becomes

$$S_I = \frac{4k_B T}{R_0} + \mathcal{O}(V^2) \tag{5.42}$$

The power spectral density of the current noise can be divided into internal and external noise voltages and we can use 5.33 in order to find both internal and external noise voltages. We refer to 5.32 to determine the internal admittance $Y_{int}(\omega)$, or the inverse of the impedance

$$Y_{int}(\omega) \equiv \frac{I(\omega)}{V_{int}(\omega)} = -s_I(\omega) I_0 \frac{1}{\mathscr{L}_I}(1 + i\omega\tau) \tag{5.43}$$

and to 5.31 to determine the external admittance

$$Y_{int}(\omega) \equiv \frac{I(\omega)}{V_{ext}(\omega)} = -s_I(\omega) I_0 \frac{\mathscr{L}_I - 1}{\mathscr{L}_I}(1 + i\omega\tau) \tag{5.44}$$

Now, if all the noise sources we are considering, which namely are internal, external, noise due to fluctuations in the thermal conductance and amplifier noise, are uncorrelated we can write the expression for the overall power-referred noise in a TES

$$S_P(\omega) = \frac{S_I(\omega)}{|s_I(\omega)|^2} \tag{5.45}$$

with

$$S_I(\omega) = S_{V_{ext}}(\omega)|Y_{ext}(\omega)|^2 + S_{V_{int}}(\omega)|Y_{int}(\omega)|^2 + S_{P_{TFN}}(\omega)|s_I(\omega)|^2 + S_{I_{amp}}(\omega) \tag{5.46}$$

where $s_I(\omega)$ is the power to current responsivity in 5.27. We will now compute explicitly the current referred noise for the four main contributions in a TES: the Johnson noise of the TES itself, the Johnson noise of the load resistor, the thermal fluctuation noise and the SQUID noise. The TES power spectral density, due to a voltage noise power spectrum $S_{V_{TES}} = 4k_B T_0 I_0^2 R_0 \xi(I)$ is

$$S_{P_{TES}} = 4k_B T_0 I_0^2 R_0 \frac{\xi(I)}{\mathscr{L}_I^2}(1 + \omega^2\tau^2) \tag{5.47}$$

with $\xi(I)$ being a non linearity term. We can do the same for the load resistor contribution

$$S_{P_L} = 4k_B T_L I_0^2 R_L \frac{(\mathscr{L}_I - 1)^2}{\mathscr{L}_I^2}(1 + \omega^2\tau_I^2) \tag{5.48}$$

The thermal fluctuation noise current, taken from [47]

$$S_{P_{TFN}} = 4k_B T_0^2 G \times F(T_0, T_{bath}) \tag{5.49}$$

The total noise of the TES $S_{P_{tot}}(\omega)$ is the sum of 5.47, 5.48 and 5.49 From this expression we can calculate the theoretical resolution of a TES calorimeter

$$\Delta E = 2.355 \left(\int_0^\infty \frac{4}{S_{P_{tot}}(\omega)} d\omega \right)^{-1/2} \tag{5.50}$$

5.2 rf-SQUID

The Superconducting QUantum Interference Device (SQUID) operated in RF-mode is a device that can be easily adapted for large arrays operation, such as HOLMES; indeed it does not need a feedback loop per detector for readout, as a regular DC SQUID needs. It is suitable for reading out larger arrays of TES since the readout needs only two coax cables for N detectors instead of $\sqrt{N}$ wires and it has less dissipation per SQUID. HOLMES will deploy an array of 1000 detectors inside a $^3He - ^4He$ dilution refrigerator, and it is crucial to limit the number of wires running from room temperature to the cold point, where the detectors are hosted. An array of rf-SQUIDs operating in flux ramp modulation meets this requirements since the whole array can be coupled to the same flux ramp circuit and read out with several RF resonantors coupled to a common feedline. Such an arrangement can be read out with just a couple of wires. In the following paragraphs I will report some very introductory functioning concepts of the SQUID taken from a review by Ryhaänen and Seppä from 1989 and from the PhD thesis of Mates, submitted in 2011 [49].

The SQUID is a superconductive ring interrupted by a thin insulating barrier, called a Josephson junction. The current through the barrier is

$$I = I_C \sin\theta \tag{5.51}$$

with I_C the critical current of the superconductor and θ the phase difference of the wave function across the junction. In Ginzburg-Landau theory the wave function of a superconductor is $\psi = \sqrt{n_s}e^{i\phi}$ where n_s is the density of Cooper pairs and ϕ is the phase. Integrating the supercurrent $\mathbf{j} = (e\hbar/2im)[\psi^* \bigtriangledown \psi - \psi \bigtriangledown \psi^*] - (2e^2/m)|\psi|^2$ along the closed path $\mathscr{L}$ of the loop containing the junction we obtain

$$\frac{2e}{\hbar}\Phi + \theta \equiv \frac{2e}{\hbar}\oint_{\mathscr{L}} \mathbf{A}\cdot d\mathbf{l} + \frac{2m}{n_s e\hbar}\int_{\text{junction}} \mathbf{j}\cdot d\mathbf{l} = n2\pi \tag{5.52}$$

where Φ is the flux in the ring, θ is the phase difference across the junction and $\mathbf{A}$ is the potential of the magnetic field $\mathbf{B}$. For $\theta = 0$ the circulating current is $I_S = I_C \sin\theta = 0$ and $\Phi = nh/2e = n\Phi_0$. In general the total flux $\Phi = \Phi_a + L_S I_C$ is equal to the externally applied flux Φ_a plus the flux contribution due to the self inductance of the SQUID L_S. We can combine 5.51 and 5.52 and write the adiabatic expression

$$\Phi_a = \Phi - L_S I_C \sin(2\pi\Phi/\Phi_0) \tag{5.53}$$

with $\Phi_0 = h/2e \simeq 2\times 10^{-5}$ Wb being the quantum of magnetic flux.

The expression can be re-written if we define $L_J \equiv \Phi_0/2\pi I_c$

$$\phi_a = \phi - \frac{L_s}{L_J}\sin\phi \tag{5.54}$$

with $\phi = 2\pi\Phi/\Phi_0$ and $\phi_a = 2\pi\Phi_a/\Phi_0$ being the normalised total and applied flux in the SQUID and $\lambda \equiv L_S/L_J = 2\pi L_S I_c/\Phi_0$. In order to have a non hysteretic SQUID we want $d\Phi_a/d\Phi > 0$ so we want $\lambda < 1$ as shown in Figure 5.3.

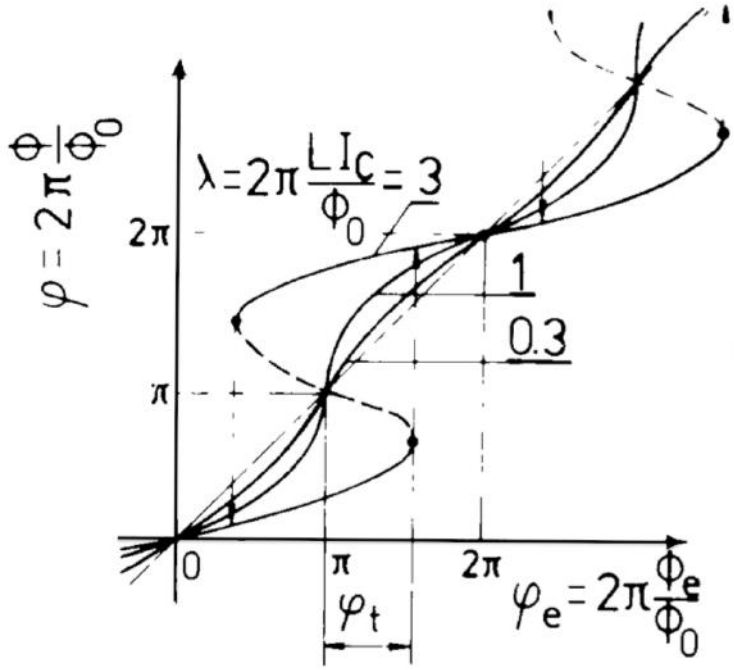

Figure 5.3: The SQUID flux response Φ to an external applied flux Φ_e for different values of $\lambda = 2\pi LI_c/\Phi_0$; for $\lambda < 1$ the response is non hysteretic; for $\lambda > 1$ the response is hysteretic

Since we want to use as many as 1000 SQUIDs coupled directly to the cold stage of the dilution refrigerator, each channel must dissipate very little power so not burden the 10 mK stage with a prohibitive heat load. In order to limit the heat load, no shunts can be employed for stabilising a hysteretic SQUID so, in order to operate large dissipationless SQUID arrays, a $\lambda \approx 1/3$ is desirable.

In order to read out the SQUID flux variation we couple the SQUID to an RF-resonator so that the current induced in the SQUID changes the load of the resonator as shown in Figure 5.4.

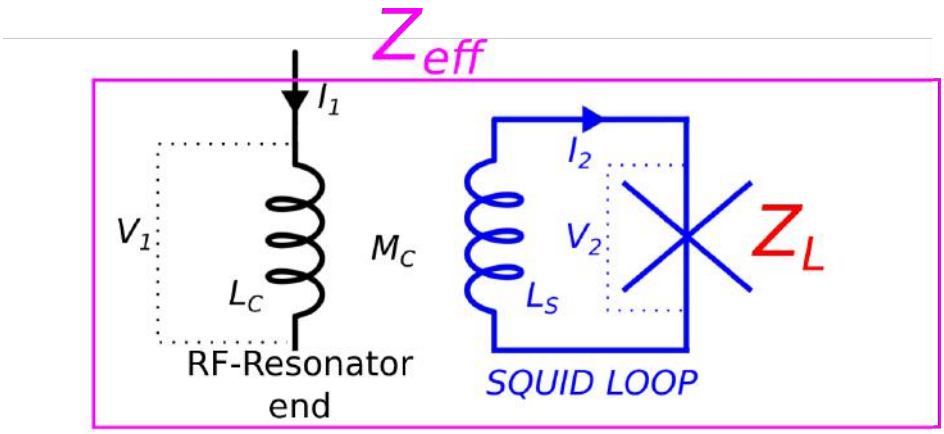

Figure 5.4: Circuit scheme of an rf-SQUID coupled to the load of a resonator

We have to calculate the effective impedance Z_{eff} of the resonant circuit (drawn in black in Figure 5.4); we have to evaluate the current in the first circuit, in order to do so we have to solve the coupled equations

$$V_1 = i\omega I_1 L_c - i\omega I_2 M_c \tag{5.55}$$

$$V_2 = -i\omega I_2 L_S + i\omega I_1 M_c = I_2 Z_L \tag{5.56}$$

We can write the current I_1 induced at the resonator end in terms of the current in the SQUID

$$I_1 = I_2 \frac{i\omega L_S + Z_L}{i\omega M_c} \tag{5.57}$$

and use it to evaluate the voltage drop across the inductor L_C

$$V_1 = i\omega I_1 \left(L_c - \frac{Mc^2}{L_S + Z_L/i\omega} \right) \tag{5.58}$$

which determines the effective impedance Z_{eff} of the resonator coupled to the SQUID

$$Z_{eff} = i\omega \left(L_c - \frac{Mc^2}{L_S + Z_L/i\omega} \right) \tag{5.59}$$

which ultimately depends on Z_L, the SQUID impedance. We want to calculate the inductance variation $L(\phi)$ in resonator as a function of the field Φ in the SQUID. To do so, we first need an evaluation of Z_L, so we need to take into account the capacitance C_J of the Josephson Junction and the leakage resistance R_{sg} which shunts the junction inductance.

We can define $y \equiv i\omega L_J Y_S$ the admittance of the parallel circuit shown in Figure 5.5

$$Z_{eff} = i\omega \left(L_c - \frac{Mc^2}{L_S + \frac{L_J}{\cos\phi + y_s}} \right) \tag{5.60}$$

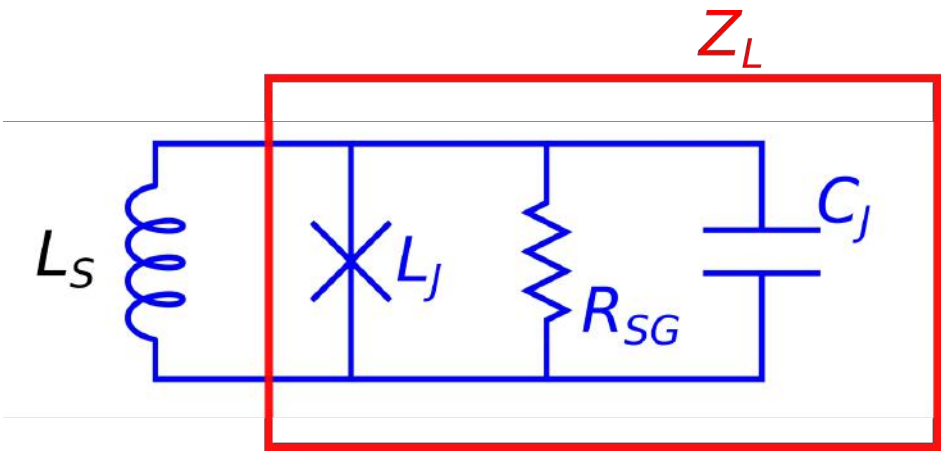

Figure 5.5: Circuit model of an rf-SQUID including leakage resistance R_{sg} and junction capacitor C_J

If we consider y_s to be small enough we can apply the perturbation theory and, at the second order we obtain

$$\Delta Z_{eff} \approx \frac{(\omega Mc)^2 Y_S}{(1+\lambda cos\phi)^2} \tag{5.61}$$

which is maximised by $cos\phi = 1$ giving

$$\Delta Z_{eff} \approx \frac{(\omega Mc)^2 Y_S}{(1+\lambda)^2} \tag{5.62}$$

The read-out inductor has an effective self inductance that changes with the flux in the SQUID

$$L(\phi) = L_c - \frac{M_c^2}{L_S + L_J sec\phi} = L_c - \frac{M_c^2}{L_S}\frac{\lambda cos\phi}{1+\lambda cos\phi} \tag{5.63}$$

For small values of λ, as it is in our case, the inductance variation $L(\phi)$ can almost be considered sinusoidal, with a peak-to-peak variation

$$\begin{aligned} L_p p &= \frac{M_c^2}{L_S}\left(\frac{1}{1+1/\lambda} - \frac{1}{1-1/\lambda}\right) \\ &= \frac{M_c^2}{L_S}\frac{2\lambda}{1-\lambda^2} \end{aligned}$$

The maximum inductance change is a crucial factor because it sets the gain of the SQUID, which can be evaluated

$$\frac{dL}{d\phi_{max}} = -\frac{M_c^2}{L_S}\frac{\lambda sin\phi}{(1+\lambda cos\phi)^2} \tag{5.64}$$

which, for $\phi = \pi/2$ is maximum woth a value $dL/d\phi = -\frac{\lambda M_c^2}{L_S}$

5.3 SQUID RF-read out and multiplexing

The rf-SQUID is naturally multiplexed by coupling the SQUID to the inductor of an RF resonator and the resonator capacitively to a common feedline. With the resonant circuit it is possible to convert the inductance variation of the SQUID into a frequency (hence phase) variation of the resonant circuit itself. In the following paragraph we shall calculate the frequency shift with respect to the flux variation.

The resonators used for the multiplexed readout in HOLMES are quarter-wavelength, i.e. the length of each resonator is tuned so that only a stationary wave with $\lambda = (2n+1)\lambda/4$ only can travel through the resonator. The resonator is shorted at one point, where the voltage is zero, and coupled capacitively to the feedline at the other end, where the current is zero.

We can write the equations of the current $I(z)$ and of the voltage $V(z)$ as a function of the distance z from the grounding point, keeping in mind that the condition for a stationary wave on a l long transmission line is

$$f_1 = \frac{v_p}{4l} \tag{5.65}$$

and we name f_1 the natural frequency of the bare resonator, in contrast to f_0 which is the resonant frequency of the coupled resonator. Voltage and current oscillating at frequency ω on a transmission line propagating with phase velocity v_p, are

$$V(z) = V_0^+ e^{-i\beta z} + V_0^- e^{i\beta z} \tag{5.66}$$

$$I(z) = \frac{V_0^+}{Z_1} e^{-i\beta z} - \frac{V_0^-}{Z_1} e^{i\beta z} \tag{5.67}$$

with beta $\beta \equiv \frac{\omega}{v_p}$.

At the shorted point at $z = 0$ we have $V(0) = 0$ and $I(0) = V_0^+/Z_1 + V_0^-/Z_1 \equiv I$, where I is the amplitude of the current oscillations at the shorted end. The equation of the current and the voltage along the transmission line are

$$V(z) = -iIZ_1 \sin(\beta z) \tag{5.68}$$

$$I(z) = I\cos(\beta z) \tag{5.69}$$

We will now couple the quarter wavelength resonator to a transmission line with a small capacity. The new resonance frequency is the frequency at which the resonators shorts the feedline; this happens when the reactance of the capacitor cancels the reactance of the quarter wavelength line. The load impedance of the l length line is [50]

$$Z = iZ_1 \tan\left(\omega \frac{l}{v_p}\right) \tag{5.70}$$

The condition for resonance is satisfied when

$$\frac{1}{i\omega_0 C_c} + iZ_1 \tan\left(\omega_0 \frac{l}{v_p}\right) = 0 \tag{5.71}$$

which means that ω_0 needs to satisfy

$$\omega_0 C_c Z_1 = \cot\left(\omega_0 \frac{\pi}{2\omega_1}\right) \tag{5.72}$$

with $\omega_1 = 2\pi/f_1$. The equation can not be directly solved, but for small $\omega_0 C_c Z_1$ we can expand the cotangent around $\pi/2$ and obtain

$$\omega_0 \approx \frac{\omega_1}{1 + 2\omega_1 C_c Z_1/\pi} \tag{5.73}$$

The coupling reduces the resonance frequency

$$f_0 = \frac{f_1}{1 + 4f_1 C_c Z_1} \tag{5.74}$$

For weak capacitance the resonant frequency remains unchanged after coupling the resonator to the line.

The next step is to add the inductively coupled SQUID at the other end of the resonator. The SQUID inductance changes with the applied flux. By coupling the SQUID to the resonator we can transduce this inductance change into a resonance frequency change. We can rewrite the resonance condition adding the extra term in the impedance equation

$$\frac{1}{i\omega_0 C_c} + Z_1 \frac{i\omega_0 L \cot\left(\omega_0 \frac{l}{v_p}\right) + iZ_1}{Z_1 \cot\left(\omega_0 \frac{l}{v_p}\right) - \omega_0 L} = 0 \tag{5.75}$$

We can expand around the quarter wavelength resonance ω_1

$$\frac{\omega_0}{\omega_1} = \frac{1 - \omega_1^2 L C_c}{1 + 2\omega_1 C_c Z_1/\pi + 2\omega_1 L/\pi Z_1 - \omega_1^2 L C_c} \tag{5.76}$$

If we design the coupling to be $\frac{1}{\omega_1 C_c} \gg Z_1$ and the load inductor so that $\omega_1 L \ll Z_1$ we can discard second order terms

$$f_0 = \frac{f_1}{1 + 4f_1 C_c Z_1 + 4f_1 L/Z_1} \tag{5.77}$$

Finally, we can calculate the frequency variation $\partial F_0/\partial L$ for an inductance variation

$$\frac{\partial F_0}{\partial L} = -\frac{4f_0^2}{Z_1} \tag{5.78}$$

We can substitute 5.64 and calculate the frequency variation with respect to the flux variation in the SQUID

$$F_0(\phi) \approx f_1 - 4f_1^2 C_c Z_1 - \frac{4f_1^2 L_c}{Z_1} + \frac{4f_1^2 \lambda M_c^2}{Z_1 L_S} \cos\phi \tag{5.79}$$

So, in order to measure the flux linked to the SQUID we have to read out a frequency variation of a resonant circuit coupled to the SQUID itself. It is important to design the coupling Q_c of the resonator to the feedline so that the total bandwidth of the coupled resonator is matching with the peak to peak frequency of the SQUID operated in flux ramp modulation.

5.3.1 Flux ramp modulation

The periodic response of the SQUID has to be linearised so that the signal can be properly reconstructed. The linearisation has to be achieved using a common method for all the SQUIDs, in order to avoid coupling each SQUID to an independent feedback loop wired all the way to the warm electronics outside the cryostat.

The method for linearising the response of an array of rf-SQUIDs is the flux ramp modulation: a common line is coupled to every SQUID. A periodic voltage ramp is sent through the line in order to sweep the SQUID for several flux quanta. The oscillation pattern of the SQUID is constant in time if no extra flux is applied from the TES circuit. On the other hand if there is a current variation in the TES, it will add extra flux to the SQUID that will result in a phase shift with respect to the oscillation with the unbiased TES, which is used as a reference for demodulation. The demodulation itself is achieved though a few steps that allows us to evaluate the phase shift as a function of time, so that the thermal pulses can be properly reconstructed. An example is shown in Figure 5.6. Within this framework, each ramp period represents an effective sample of the pulse.

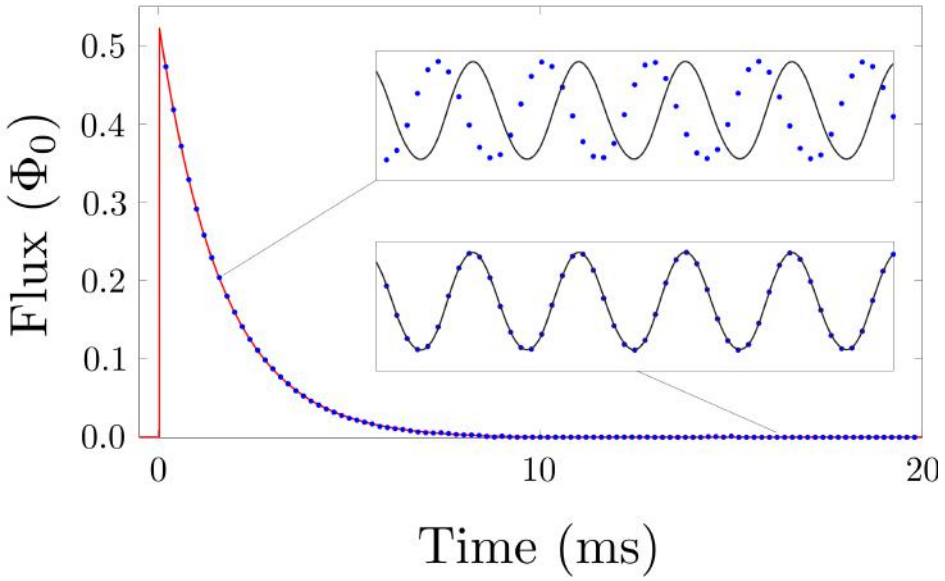

Figure 5.6: Simulated pulse reconstructed with rf-multiplexing with flux ramp modulation

The flux ramp modulation also allows us to move the bandwidth of the TES signal to higher frequencies where the two level system noise, which scales roughly as $1/f$ is lower than the HEMT amplifier noise. With the flux modulation we measure a phase shift of the SQUID response over time for all the SQUIDs

$$\phi = \arctan\left(\frac{-\sum x(t)\sin\omega_m t}{\sum x(t)\cos\omega_m t}\right) \tag{5.80}$$

The phase modulation eliminates the noise components arising from the critical current I_C fluctuations, which induces fluctuations in the amplitude of the SQUID oscillations, and the

noise components arising from the two-level system, which causes an offset fluctuation of the SQUID response. The phase extraction does not depend on the oscillation shape and the information is extracted only from the first Fourier harmonic; the information in the higher order harmonics can be discarded if the resonator coupling is well matched to the SQUID response, so that the phase shift is carried in the lower order harmonics.

The goal for HOLMES is to use flux ramp at 500 kHz, in order to be able to properly sample the 10 μs fast pulses. In order to make the best use of the whole available digitiser bandwidth we need to run the demodulation algorithm with no more than two SQUID oscillations per ramp.

Operating the rf-SQUID at frequencies up to 500 kHz needs a specially designed quarter wavelength withn resonators with 2 MHz bandwidt. The bandwidth of a resonator BW is correlated to its quality factor Q_{tot} by

$$BW = \frac{f_{res}}{Q_{tot}} \tag{5.81}$$

with f_{res} being the central frequency of the resonator. The variable that needs to be tuned in order to adjust the resonator bandwidth with the one of the rf-SQUID is the quality factor Q_{tot}. The quality factor Q_{tot} is the sum

$$\frac{1}{Q_{tot}} = \frac{1}{Q_c} + \frac{1}{Q_i} \tag{5.82}$$

with Q_i being the internal quality factor of the superconducting material, Ni in the case of HOLMES, and Q_c being the coupling quality factor of the resonator to the feedline. The latter needs to be precisely tuned in order to provide the necessary bandwidth of the resonator. The design and the production process of the resonator chip have been successfully carried out at NIST.

Once the bandwidth of each resonator has been set in order to properly sample the TES pulses, one can design the multiplexed readout electronics.

5.3.2 Multiplexing factor

The aim of HOLMES is to collect as much data as possible in the region of interest of the EC decay spectrum of ^{163}Ho. The challenge is to maximise the activity of each pixel, yet we have to ensure a low pile-up rate, since the unresolved pile-up events are the main contribution to background at the end point of the spectrum. The pile-up is kept in check by fast detectors with exponential rise time $\tau_{RT} \sim 10\mu s$ sampled at 500 kHz. The high sampling rate is essential for efficiently applying the pile up rejection algorithms; at the same time, the sampling rate is a limiting factor for multiplexing. At the moment, the desired sampling rate of 500 kHz sets the limit on the number of multiplexable channels per each digitiser board. An estimation of the multiplexing factor can be done assuming to be using an acquisition system (the ROACH-2, described in chapter 7) with a 550 MHz digitiser bandwidth. There are several factors which need to be taken into account in the calculation in order to limit the roll off, the cross talk and the non linearity:

- f_{sample} sampling frequency of the signals i.e. the ramp frequency

- n_{Φ_0} number of SQUID oscillations per each ramp
- S resonance spacing (~ 10)
- 2 two side band of each resonance

With these factors, the number of multiplexable channels on a 550 MHz bandwidth board will be

$$N_{detectors} = \frac{BW}{f_{sample} \times n_{\Phi_0} \times S \times 2} \tag{5.83}$$

with a total available bandwidth $BW = 550$ MHz, an effective sampling rate $f_{sample} = 500$ kHz, using $n_{\Phi_0} = 2$ per each ramp, a total of $N_{detectors} \approx 30$ is multiplexable on each digitiser board.

5.3.3 Flux noise

Besides the TES noise sources described in the previous paragraphs, the SQUID itself has noise components which could contribute to the total power spectrum of the detectors. The noise sources are the Johnson noise in the flux input circuit, the intrinsic flux noise in the SQUID, the HEMT amplifier noise, and two-level system (TLS) noise in the resonator. The contribution of the TLS noise is significant at low frequencies, and it is completely negligible while operating the SQUID with flux ramp modulation since the working bandwidth is shifted to higher frequencies by the ramp modulation itself, where the TLS contribution is small.

5.3.3.1 Johnson noise

The circuit that finally couples inductively to the SQUID may have an impedance with a real component. Microwave power in the resonator may therefore dissipate in the input circuit. The power dissipation can induce noise currents through the SQUID input coil with power density $S(I) = 4k_B T/R_{input}$. The choice of R_{input} has to be such that this noise is small compared to the other sources of noise in the system.

5.3.3.2 SQUID noise

In a dissipationless SQUID there a two different mechanisms that present a source of noise. The noise arises from fluctuations in the critical current across the junction and from the flipping of magnetic dipoles on the SQUID loop. In either cases the spectral density scales as $1/f$. Measurements at NIST using DC-SQUIDs showed that the sum of the two contributions showed no significant dependence on Φ, so since the fabrication process has remained unchanged we can safely assume that neither of these two noise sources represent a threat.

5.3.3.3 Two Level Systems

Superconducting microwave microresonators are known to have a source of noise, due to two level systems (TLS) [51, 52, 53, 54]. Noise originates from interactions with dielectric

layers on the surfaces [55]. The fluctuation of these two-level systems introduces a power spectral density that varies with frequency as $f^{-1/2}$, caused by the coupling of the TLS electric dipole moments to the electric field inside the resonator. It was experimentally proved that the TLS noise is generated in the capacitative section of the resonator [56]. This implies that the TLS noise could be dramatically reduced by decreasing the surface layer to volume ratio of the capacitors, for instance by using interdigitated capacitors (IDC) with large spacing between their fingers.

Despite a microscopic theory of TLS noise is not yet available, there is a semi empirical model that describes the contribution of the TLS to the power spectral density of the fractional frequency shift as a function of the driving power P_g and temperature T [54]. The spectral density varies as $P_g^{-1/2}$ and T^{β}, with β=1.5-2 [57]. We evade this noise by using flux-ramp modulation.

5.3.4 Amplifier noise

The radio frequency signal coming from the resonators is amplified by a HEMT microwave amplifier coupled on a cold stage of the refrigerator (4 K), in order to keep the amplifier noise as low as possible. Despite that, amongst all the sources of noise, the cold amplifier noise is by far the most significant component that affects the SQUID readout. Its noise power spectrum referred to the flux output of the SQUID is

$$S_{\Phi}|_{f=f_0,\Phi=Phi_0/2} = \frac{4k_B T_N L_J}{\pi f_0} \tag{5.84}$$

as an example, for T_N=6 K, at a readout frequency f_0=6 GHz and L_J=60 pH the HEMT amplifier noise is 0.6 $\mu\Phi_0/\sqrt{Hz}$.

5.3.5 Multiplexing

The multiplexing of large array of rf-SQUIDs is done in frequency domain and it is achieved by coupling each SQUID to a different resonator which has a unique resonance frequency; the resonators are subsequently read by coupling all the resonators to a common feedline. The multiplexing chip, where the rf-SQUIDs and the resonators are placed has been designed and producedat NIST. The challenge of this task was to design resonators that resonate in the microwave domain (3 to 8 GHz) and tune the design parameters in order to avoid the overlap of resonances and in order to ensure that each resonance has a sufficient bandwidth for reading out the TESs of HOLMES. It is worth stressing out that in order to achieve the required 1 μs time resolution it is vital to have detectors as fast as 10 μs exponential rise time sampled at 500 kHz; this means that the bandwidth of each resonator needs to be at least 1 MHz. Ideally one would like to have the resonances one as close as possible to the adjacent one, in order to maximise the multiplexing factor given a fixed digitiser bandwidth, which in the case of HOLMES will be 550 MHz for each ROACH-2 board, yet if the tails of their Lorentzian shape overlap, crosstalk phenomena can occur.

We will therefore calculate the frequency separation of two Γ_1 and Γ_2 wide resonance.

Considering a voltage wave traveling trough the feedline coupled to neighbouring resonances; the transmission coefficient including first order reflections is:

$$S_{21} = (1+\Gamma_1)(1+\Gamma_2)(1+\Gamma_1\Gamma_2+\Gamma_1^2\Gamma_2^2+\cdots) \tag{5.85}$$

$$= \frac{(1+\Gamma_1)(1+\Gamma_2)}{1-\Gamma_1\Gamma_2} \tag{5.86}$$

$$= \frac{(\Gamma_1^{-1}+1)(\Gamma_2^{-1}+1)}{\Gamma_1^{-1}\Gamma_2^{-1}-1} \tag{5.87}$$

$$= \frac{4\frac{Z_{R1}Z_{R2}}{Z_0^2}}{4\frac{Z_{R1}Z_{R2}}{Z_0^2}+2\frac{Z_{R1}}{Z_0}+2\frac{Z_{R2}}{Z_0}} \tag{5.88}$$

$$= \frac{2}{2+\frac{Z_{R1}}{Z_0}+\frac{Z_{R2}}{Z_0}} \tag{5.89}$$

Assuming loss free resonators with high coupling Q, so that $Z_R \propto i\delta\omega$, S_{21} can be expressed in terms of the bandwidth BW

$$S_{21} = \frac{2}{2-i\left(\frac{BW}{\omega-\omega_1}+\frac{BW}{\omega-\omega 2}\right)} \tag{5.90}$$

The contribution to crosstalk can be evaluated by considering the shift of one resonance, for instance ω_2, and measure the associated shift at $\omega = \omega_1$, at a resonator n bandwidths away from ω_2:

$$S_{21} = \frac{i}{2n^2\left(1+i\left(\frac{BW}{2\Delta\omega_1}+\frac{1}{2n}\right)\right)^2}\frac{\Delta\omega_2}{BW} \tag{5.91}$$

It is possible to show that the crosstalk into the imaginary component of S_{21} is maximised for $\frac{BW}{2\Delta\omega_1}+\frac{1}{2n}=\sqrt{3}$, so that the crosstalk is

$$Im\left[\Delta S_{21}\right] \approx \frac{-1}{16n^2}\frac{\Delta\omega_2}{BW} \tag{5.92}$$

In order to keep crosstalk between neighbouring at less than 1/1000, we need to keep the resonance spaced by at least ten times their bandwidth, i.e. 10 MHz.

5.4 ROACH-2 read out

Currently we are using an analogical two channel multiplexing, which was described in the previuos paragraphs, however, for the HOLMES 1000 detector array a digital system for RF generation and down-conversion is required. In its final configuration HOLMES will realize a SDR multiplexed read-out exploiting the Reconfigurable Open Architecture Computing Hardware (ROACH2) board with a Xilinx Virtex6 FPGA. The complete system is composed of a digital signal processing board (ROACH2), a DAC (for comb generation) and ADC (512 MS/s, 12 bit, 2 channels) boards, an IF board (for signal up- and down-conversion),

and SFP+GbE interfaces optically decoupled for fast data transfer. Software, firmware and set-up are developed in collaboration with NIST. Tests with a preliminary version of the firmware for the multiplexing of 4 channels showed encouraging results. An expanded version for 32 channels is in development and it will be ready in 2017. To read-out the full 1024 pixel array a total of 32 ROACH2-based systems is required.

Chapter 6

HOLMES detectors

In the previous chapter I have outlined the characteristics and the working principle of a TES coupled to a rf-SQUID. In the following chapter I will describe the TESs especially produced for HOLMES at NIST. The detectors are produced at NIST, then they are shipped to Genova, where ^{163}Ho is embedded and the final Gold layer is laid; finally the implanted detectors will undergo the last processing step, namely the membrane release. In order to establish the most suitable configuration for the detectors and for the readout, extensive simulations have been performed aiming at identifying the proper absorber thickness, therefore the number of atoms to be implanted in each absorber in order to reach the desired event rate and finally, few pile up rejection algorithms have been studied in order to be able to identify nearly coincident evets, which represent a major threat for HOLMES.

6.1 Detector design

In order to be sensitive to the neutrino mass, the detectors of HOLMES have to fulfill very stringent demands, which include, an energy resolution of the order of ~1 eV at 2.8 keV, a rise time $\tau_R \equiv \tau_+ \sim 10$ µs and a decay time $\tau_D \equiv \tau_- \sim 150$ µs, so that the fraction of dead time is negligible.
The resolution and the time constants require us to design the TES with peculiar characteristics. From the solution of the coupled differential equations showed in the previous chapter recall that

$$\Delta E \propto \sqrt{\frac{4k_B T^2 C(1+\beta)}{\alpha}} \tag{6.1}$$

$$\tau_R \approx \frac{L}{R_L + R_0(1+\beta)} \tag{6.2}$$

$$\tau_D \approx \frac{C}{G}\frac{1+\beta}{1+\beta+\frac{\alpha P_J}{G T_C}} \tag{6.3}$$

This set of equations will set the constraints that the parameters C, G, α and β will need to fulfill in order to reach the desired 1 eV sensitivity on neutrino mass.

6.1.1 Detector requirements

The HOLMES detectors will be TES coupled to a Gold absorbers in which the isotope ^{163}Ho will be implanted. The first parameter to be fixed is the thickness of the absorber, which determines the detection efficiency, i.e. the fraction of events fully contained in the absorber. Being a crucial parameter for the sensitivity of the experiment, several GEANT-4 based Monte-Carlo simulations have been performed in order to address the detection efficiency for different values of Gold or Bismuth absorbers and their thickness. The thickness determines the heat capacity of the absorber, which is a crucial parameter for tuning the TES parameters for an optimal detector response.

6.1.1.1 Detection efficiency

The sensitivity of HOLMES depends on the fraction of events gathered around the end point of the EC spectrum of ^{163}Ho. ^{163}Ho decays via EC to an excited state of ^{163}Dy; the information on the neutrino mass is carried in the energy emitted in the de-excitation of ^{163}Dy which mainly emits Auger electrons and X-ray photons, with a fluorescence yield lower than 10^{-5}, making the latter process negligible. Since the energy is divided amongst at least two electrons from shells higher than M1, the highest energy electron that can be emitted is 2 keV.

Preliminary GEANT-4 based simulations have been carried out in order to evaluate the absorption probability of these high energy 2 keV electrons as well as photons for different thickness values of the Gold absorber. A complete containment of both X-rays and Auger electrons would be ideal yet, it is important to keep the heat capacity of the absorber as low as possible for a higher thermal signal per energy deposition. A set of simulations with the emitter embedded between to symmetrical layers of Gold have been performed for both 2 keV electrons and 2 keV photons in order to estimate the fraction of events partially contained in the absorber. The results of the simulations are shown in Figure 6.1 and in Figure 6.2 and summarised in Tables 6.1 and 6.2, for 2 keV electrons and photons respectively. The full containment is estimated by the number of events in the 2 keV peak with respect to all the generated events, while the number partially contained events is evaluated from the integral of the tail towards lower energies.

Thickness ($\times$ 2) microns	tail [fraction]	peak [%]	escaping
0.05	2.00E-03	99.75	none
0.1	1.50E-04	99.99	none
0.5	1.40E-05	100.00	none
1	2.30E-06	100.00	none
2	4.00E-07	100.00	none

Table 6.1: Gold absorption probabilities for 2 keV electrons for different thickness

From the simulations the thickness of the gold absorber has been set to 1 μm for the bottom and for the top layer, which will guarantee a full containment of 2 keV electrons and a 99.62 % containment of 2 keV photons.

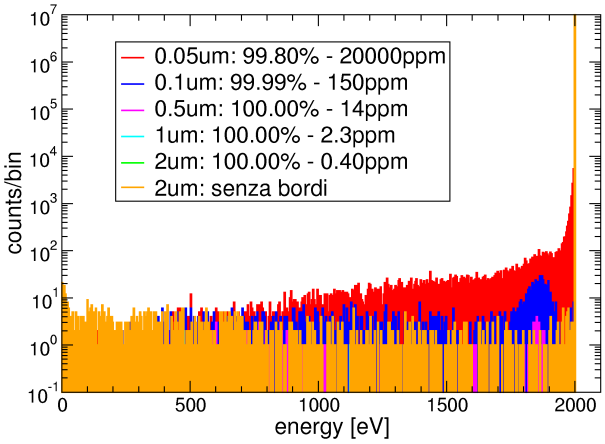

Figure 6.1: Calorimetric energy spectrum of 2 keV electron emitted in different thickness gold absorbers.

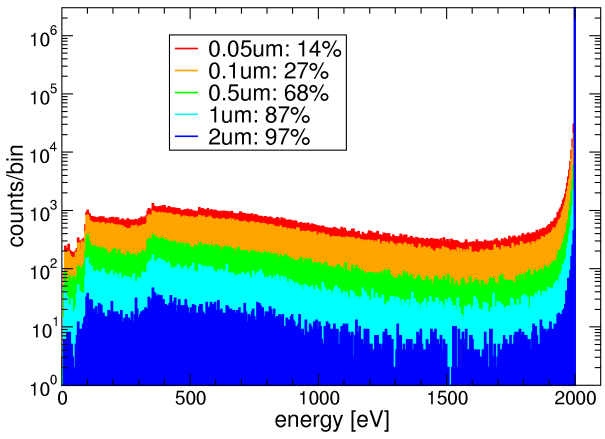

Figure 6.2: Calorimetric energy spectrum of 2 keV photons emitted in different thickness gold absorbers.

Once the thickness is adjusted in order to contain the desired fraction of events, the other dimensions of the absorber have to be set in order to obtain the desired thermal capacity C of the detector. The heat capacity has to be kept as low as possible in order to maximise the temperature increase of the absorber, hence the pulse height. The total thermal capacity of the detector is the sum of the thermal capacity of the absorber and of the thermal capacity of the TES itself $C = C_{TES} + C_{Au}$. $C_{TES} \approx 0.2$ pJ/K while C_{Au} can be easily evaluated from the geometry and the material characteristics. The pixel has to be large enough for the 10^{13} ^{163}Ho atoms that have to be impanted, without affecting the thermal properties of the detector itself.

Putting all this together, the best absorber dimension for HOLMES will be 200×200×2 μm^3 Gold.

The thermal capacity C of our devices can be now evaluated; for temperatures lower than the Debye temperature $T \ll \Theta_D$, which for Gold is $\Theta_D = 164$K, we can write the sum of the electronic and lattice contributions to the total Gold heat capacity

$$C_{el} = n\gamma T \tag{6.4}$$

$$C_{lat} = \frac{12\pi^4}{5} nR \left(\frac{T}{\Theta_D}\right)^3 \tag{6.5}$$

with n being the number of moles, γ the Sommerfeld coefficient ($\gamma = 0.729$ mJ/molK^2 for bulk gold) and $R = 8.31$ J/mol K the gas constant. At 100 mK the lattice contribution to the total specific heat for Gold is three orders of magnitude smaller than the electron heat capacity and is therefore negligible.

For the HOLMES detectors the heat capacity of the absorber at the operating temperature of 100 mK is $C_{Au} = 0.57$ pJ/K and the TES itself has a heat capacity $C_{TES} = 0.2$ pJ/K.

6.1.2 Detector design

What we experimentally measure is a temperature $\Delta T = \Delta E/C$ increase due to an energy deposition $\Delta E = 2.8$ keV in an absorber with thermal capacity $C = 0.7$ pJ/K. The TES will respond to the temperature increase with a resistance variation that can be detected using a proper electronic chain. A very sharp transition (i.e. high $\alpha = \frac{d\log R}{d\log T}$) guarantees higher signals which is the basis for achieving a higher energy resolution. One of the limitations

Thickness (× 2) microns	tail [%]	peak [%]	escaping
0.05	2.11E-01	78.89	86
0.1	9.61E-02	90.39	73
0.5	1.25E-02	98.75	32
1	3.85E-03	99.62	13
2	7.30E-04	99.93	3

Table 6.2: Gold absorption probabilities for 2 keV photons for different thickness

is the width of the transition, which is proportional to $\sim 1/\alpha$ is the detector linearity: in order to guarantee a linear response over the region of interest of the EC decay spectrum the detectors need to operate between 30% and 60 % of the resistance variation of the transition, where R(T) is safely linear; this sets the upper limit for the choice of α.

Another important design factor, strictly connected to α and the detector performance is the thermal conductance G between the TES and the thermal bath. G is crucial for the detector performance because it sets the decay time constant $\tau_D \approx \frac{C}{G}\frac{1+\beta}{1+\beta+\frac{\alpha P_J}{GT_C}}$ which is important in order to maximise the live time of the experiment, since for a time $t = 5 \times \tau_D$ after each signal one wants to discard any other pulse in the detector before the base temperature is restored and the gain of the detector, which is a function of temperature, returns to the optimal value. The choice of a high G comes to a price though: as G increases, so does the value of the current necessary to keep the detector at its operating point. A high current value flowing though the TES reduces α and hence the pulse height.

Finiding a proper compromise amongst all the operational parameters is a rather complicate matter; the detector design has been tuned and refined by the Quantum Sensors Group at NIST. NIST is in charge of the design, test and subsequently the fabrication of the TES and the first layer of absorber for HOLMES. Before choosing the final TES for the 1000 detector array an array of 20 single detectors has been produced and intensively tested both at NIST and in Milano-Bicocca.

6.1.2.1 Time response and pile up rejection

A very important feature for the detectors for HOLMES is the speed: in order to keep the pile-up fraction as low as possible it is crucial to have detectors with a fast rising signal since the pile-up fraction is $f_{pp} = \tau_{eff} \cdot A_{EC}$ with A_{EC} being the Holmium activity per pixel and τ_{eff} being the effective time resolution, dependent on the rise time τ_R of the detector and on the pile-up resolving algorithms efficiency. The rise time $\tau_R \approx \frac{L}{R_L+R_0(1+\beta)}$ is dependent on the inductance L in the bias circuit of the TES. A low inductance means faster signals which reduces the pile-up probability. Besides, in order to reach the desired time resolution τ_{eff}, offline rejection algorithms must be applied. Regardless to the chosen algorithm, its rejection efficiency increases with the number of samples on the rising edge of the pulse. Since HOLMES will operate 1000 detectors at very low temperature, multiplexed readout is required as well. The multiplexing factor $n_{mux} \propto \frac{ADC_{bwidth}}{f_{sample}}$ so, in order to keep the multiplexing factor of the order of 30, each detector will be sampled at $f_{sample} = 500$ kHz.

In order to estimate the unresolved pile-up fraction three values of inductance, L = 12, 24, 48 nH, are simulated to enable evaluation of pile-up detection contrasting relatively rapid with relatively slow pulse rises, the latter allowing a higher number of samples on the rising edge. We simulate current pulses in a TES. The dynamics of detector temperature T and current I are modeled by the ordinary differential equations showed in the previous chapter

$$C\frac{dT}{dt} = -P_{bath} + P_j + P \tag{6.6}$$

$$L\frac{dI}{dt} = V - IR_L - IR(T, I) \tag{6.7}$$

with $P_{bath} = k \cdot (T^n - T^n_{bath})$, $P_J = I^2R(T, I)$ and $P = \sum_i \delta(t - t_i) \cdot E_i$ is the power dissipated by an energy deposition E_i arriving at $t = t_i$.
The simulations were performed with a variable delay between the first and the second pulse ranging from 1 µs to 8 µs with a 1 µs step. Furthermore, the arrival time does not match with the sampling. The simulated signals are indeed originally oversampled and the arrival time is generated randomly, in order to recreate a realistic situation. Finally, we have simulated events with a summed energy $E_{sum} = E_1 + E_2 = 2.6$ keV. The rejection efficiency is defined as the fraction of the pile-up events rejected by discrimination algorithms. Therefore, the time resolution τ_{eff} is

$$\tau_{eff} = T \left[1 - \int_0^T \frac{\eta(x)}{T} dx \right] \tag{6.8}$$

with T being the considered time interval for the eventual occurrence of two events and $\eta(x)$ is the rejection efficiency. We have simulated a 12 bit ADC with a dynamic range from 0 to 40 µA, which is the expected current variation in a TES due to a 4 keV energy deposition. We have as well set the sampling frequencie either at 1 or at 2 MHz and we have limited each record length at 1024 and 512 points, respectively. The number of points before the trigger in each acquisition time window is 1/8 of the record length. The analysis is based on the optimal filter [58] and the Wiener filter.

- **optimal filter**:The optimum filter (OF) provides an estimation for the signal amplitude, hence it is used as an energy evaluator; several algorithms are based on the OF and it can as well be used as a discriminator of spurious events. In the frequency domain the OF transfer function $H(\omega)$ is

$$H(\omega) = \eta \frac{S^*(\omega)}{N(\omega)} e^{-1\omega t_M} \tag{6.9}$$

  where $S^*(\omega)$ is the complex conjugate of the Fourier transform of the ideal signal, $N(\omega)$ is the total noise power spectrum, t_M is the delay of the analysed pulse with respect to a pulse which is taken as reference and η is a normalization factor. The OF acts on the frequency components of the signal eliminating the frequencies where the noise contribution is more significant. We evaluate $S(\omega)$ by averaging a large number of raw pulses in order to eliminate the random fluctuations due to the noise; $N(\omega)$ is obtained by acquiring many signal free baselines and averaging the corresponding power spectra. The filtered pulse can be used for calculating the shape parameters that shall be used as tools for discarding spurious events. The most effective parameters for pile up discrimination are the root mean square differences between the filtered average pulse A(t) and the filtered analysed signal O(t). The analysed signal is normalised to the average pulse amplitude. The square differences (TV)of the two functions are given by the below equation and they are evaluated on the right (TVR, test value right) and the left (TVL, test value left) side of the maximum in a defined time interval.

$$TV = \frac{1}{N} \sum_N^i \left(\frac{A_i - O_i}{A_{max}} \right)^2 \tag{6.10}$$

  with A_{max} being the analysed pulse maximum.

- **Wiener filter** The Wiener Filter (WF) technique is a digital filter to gain time resolution and its transfer function is

$$H_i^W = \frac{S_i^*}{N_i + \alpha |S_i|^2} \tag{6.11}$$

where S_i and N_i are the i-th discrete Fourier transform component of the average pulse and the ith component of the noise average power spectrum, respectively; α is a parameter that depends on the energy of the signal to be filtered and it scales the average pulse power in order to be correctly compared to the noise average contribution.

We have performed simulations for different pulse shapes and for different sampling frequencies. The comparison between rejection efficiency achieved with the OF pulse shape analysis and with the WF are reported in Table 6.3 together with the predicted energy resolution E_{FWHM} at 2047 eV evaluated with the OF. The energy resolution has been determined simulating 10000 single mono-energetic pulses. The simulated signals are originally oversampled and then downsampled in order to recreate a realistic situation. The effective sampling rate of the pulse plays a crucial role in pile up identification, regardless of the chosen algorithm, and in order to investigate the samplig rate effect on the Wiener filter application we have performed simulations with 1 MHz and 2 MHz effective pulse sampling. In principle, concerning the pile up identification, it would be desirable to have the highest sampling rate available according to the read out electronics. For HOLMES it is not so straightforward, since the sampling rate is directly included in the calculation of the multiplexing factor: a higher sampling rate reduces the multiplexing ability and would require more copies of the components of the warm electronics. It is not necessary though to fix the sampling rate before the completion of the whole array, since it could easily be adjusted and change subsequently. Ideally HOLMES will be able to use a 2 MHz effective pule sampling, but according to the results obtained with the Wiener filter algorithm, an effective sampling rate of 1 MHz could be also used.

In the right panel of Figure 6.3 a pile-up event well identified by the Wiener Filter is displayed together with the Optimum filter outputs of the raw and average pulses.

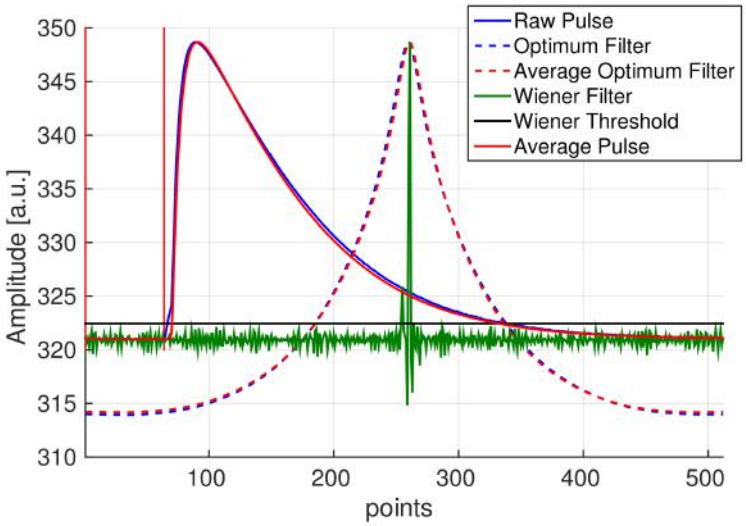

Figure 6.3: An example of a pile-up event well identified by the Wiener (green solid line) filter. In blue dashed line is the Optimum filter output of the raw pulse while in red dashed line is the Optimum filter output of the average pulse. In black the Wiener threshold for the discrimination of pile-up events

L [nH]	τ_R [µs]	f_{sample} [MHz]	Lenght [samples]	τ_{eff}^{OF} [µs]	τ_{eff}^{WF} [µs]	ΔE_{FWHM} [eV]
24	2.3	2	1024	1	0.9	1.7
24 (a)	2.3	1	512	1.8	1	3
48	4.5	1	512	4.2	1.3	2.1

Table 6.3: OF test concerns cuts on both shape parameters (TVL, TVR). The effective time resolution τ_{eff} has been estimated from the rejection efficiency, under the requirement to detect 99 % of single events. The energy resolution ΔE_{FWHM} at 2047 eV is evaluated with the OF, simulating 10000 mono-energetic pulses affected by noise. For the simulation in the second row (a) the sampling time is only two times faster than the rise time. The scatter in energy resolution is due to the number of the samples on the rising edge of the pulse

The Wiener Filter technique shows an excellent pile-up rejection efficiency which turns out to be sufficient for HOLMES goal: for a pulse rise time of around 5 µs an effective time resolution of 1.3 µs was achieved; this is translated in a pile up fraction $F_{pp} = 4 \cdot 10^{\cdot -4}$. These results closely match the baseline specifications of the HOLMES experiment, which aims at a time resolution of ~1 µs and an energy resolution of ~1 eV.

6.1.3 Final TES design

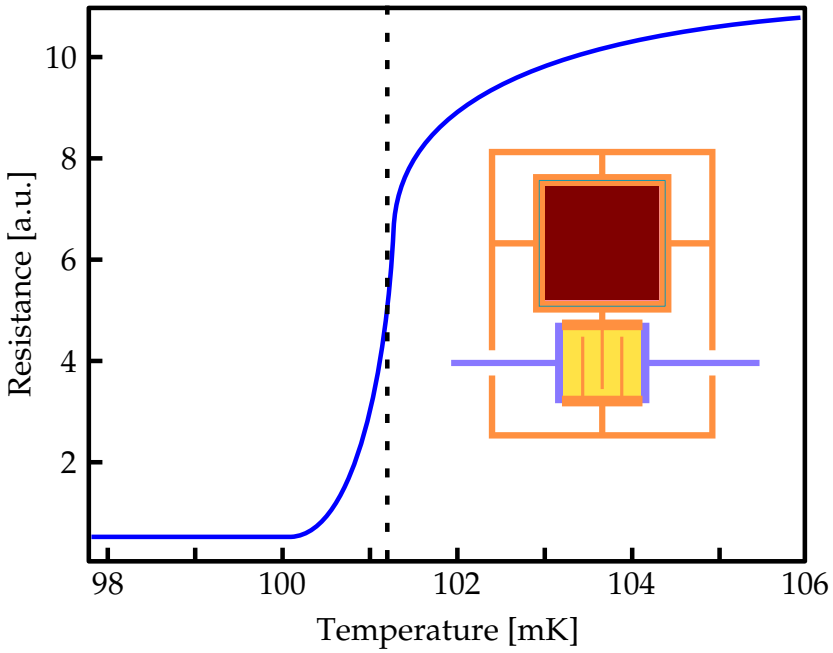

Figure 6.4: Transition shape of the TES prototype (R vs T); the TES scheme is shown as well with the absorber is placed next to the TES on the same Si_2Ni_2 membrane

The intial detector design was intended to have the absorber atop of the TES, but at the first cryogenic test it was seen that the Gold layer deformed the TES transition shape due to proximity effects. In order to obtain a proper superconductive transition a new chip has been designed. In the new version, dubbed *sidecar* design, the TES in placed beside of a gold absorber, as is it shown in the scheme in Figure 6.4; the thermal conductance between the two is provided by a Copper link with a thermal conductance G_1. A different Copper structure stretching from the TES towards the edges of the membrane is used to increase the thermal conductance G towards the bath. Two different geometries, shown in Figure 6.5 were designed in order to choose the most suitable shape of the thermal conductance G_1.

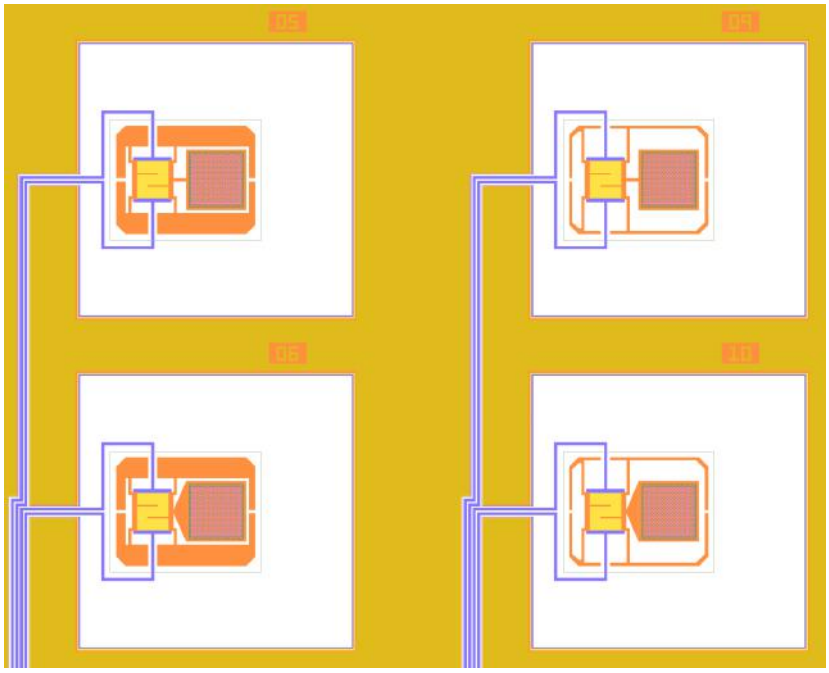

Figure 6.5: Four different geometries were designed in order to tune the thermal conductance G_2 between TES and absorber and the thermal conductance G between TES and thermal bath

In either configurations $G = 570$ pW/K and $G_1 = 70$ nW/K so it's safe to assume $G_1 \gg G$ and $G_1 \sim \infty$. The chip is designed to have thermal capacities C_1=0.2 pJ/K for the TES and C_2 ~0.6 pJ/K for the absorber. During the first cooldown at NIST complex impedance measurements were performed. The results are shown in Figure 6.6. It can be seen that the detector is more accurately described by a two body-like system rather than a single body.

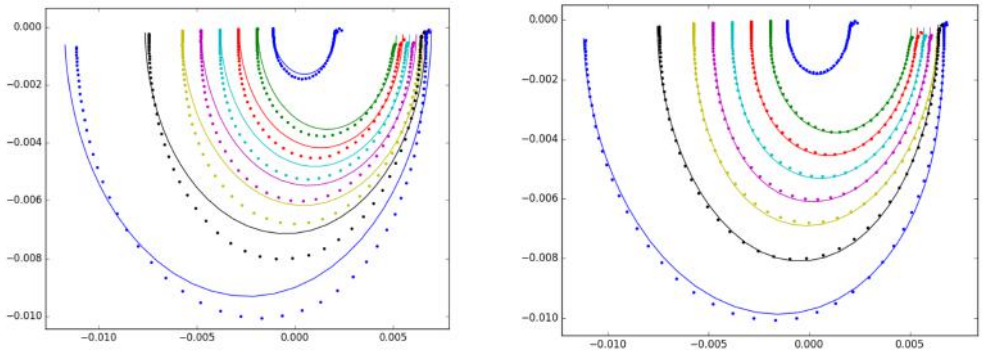

Figure 6.6: Fit of the complex impedance with one body model (left) and two bodies model (right) for different values of R_{TES}.

From the complex impedance measurements we found that the geometry of the thermal link between TES and absorber does not affect the thermal conductance G_1. By analysing the

complex impedance data it can be seen that a second body is indeed necessary to explain the detector response yet, is not straightforward to identify and isolate the physical components which are responsible for this second body heat capacity. The thermal conductance linking the second body to the TES can be evaluated to be $G_2 = 750$ pW/K. A possible interpretation could be the existence of a parallel thermal conductance between the absorber and the copper perimeter, as shown in the scheme in Figure 6.7

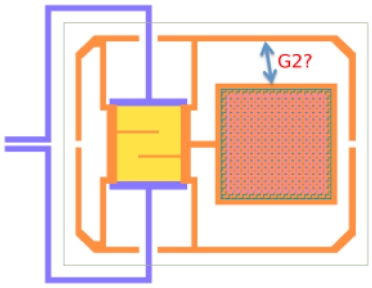

Figure 6.7: A possible cause of the two body behaviour could be the existence of a parasitic thermal conductance $G_2 \sim 750$ pW/K between the absorber and the Copper perimeter

The devices were tested both at NIST and in Milan, showing no pulse shape deformation neither during the rising edge or during the decay time. The detector response to energy deposition is the ultimate test that allowed us to exclude any major implications due to the two body behaviour. The results will be extensively analised in the following chapter.

6.2 ^{163} Ho production

HOLMES aims at a reaching a 1 eV sensitivity on neutrino mass and, according to the simulations a total amount of 6×10^{16} ^{163}Ho nuclei are necessary in order to be able to collect the desired 10^{13} events during its three year long data taking window.

^{163}Ho was discovered in 1960 in a sample of irradiated ^{162}Er that was activated in a nuclear reactor. ^{163}Ho is not indeed available in nature and a special process needs to be studied for its production. An experiment of the scale of HOLMES, which aims at collecting $\sim 3 \cdot 10^{13}$ events during a three year long data taking, needs $\sim 6.5 \cdot 10^{16}$ ^{163}Ho atoms. The necessary atoms will be produced by neutron irradiation of Er_2O_3 enriched in ^{162}Er with the reaction

$$^{162}\mathrm{Er}(n,\gamma)^{163}\mathrm{Er} \longrightarrow^{163} \mathrm{Ho} + \nu_e \tag{6.12}$$

with the decay $^{163}\mathrm{Er} \longrightarrow^{163}$ Ho $+ \nu_e$ being an EC process with a 75 minute half-life. The cross section $\sigma(n,\gamma)$ is about 20 barns for thermal neutrons. During the irradiation process ^{163}Ho is also subject to neutron capture and, in order to give an estimation of the quantity of enriched Er_2O_3 needed for producing the $6.5 \cdot 10^{16}$ ^{163}Ho atoms, it is necessary to know the burn up cross section. Currently, as of the end of 2016 there is no accurate measurement of the ^{163}Ho burn up cross section. The production of ^{163}Ho for HOLMES will take place at the high flux nuclear reactor of the Institute Laue-Languevin (ILL) in Grenoble, France.

The reactor has a thermal neutron flux of about 1.3×10^{15} $n/s/cm^2$. Exposing a 30% enriched $^{162}Er_2O_3$ sample to such a flux would produce ^{163}Ho with a rate of approximately 50 kBq/week/mg(Er_2O_3) neglecting the $^{163}Ho(n,\gamma)^{164}$Ho burn-up cross section.

6.2.0.1 Purification and Irradiation

In order to minimise the production of dangerous isotopes such as ^{166m}Ho, the enriched Er_2O_3 must be purified before irradiation. The chemical separation process takes place at the Laboratory of Radiochemistry (LRC) at the Paul Scherrer Institute (PSI, Villigen, Switzerland). Two separate processes are performed: *pre* and *post* irradiation. The former is necessary to remove eventual contaminants of the original enriched Er_2O_3 powder, while the latter, performed immediately after the removal from the reactor is needed to remove the highly radioactive isotopes produced during the irradiation process. Three batches of Er_2O_3 have been purchased, two of which have been pre-purified and irradiated during 55 and 56 days respectively long cycle at ILL in two different sessions. Part of the ^{163}Ho produced in the first batch, 20.6 mg, enriched in ^{162}Er at 28.2 % in is currently being used for a calorimetric measurement with Sn aborbers coupled to Si thermistors in Milano-Bicocca.

The second batch of 141 mg enriched in ^{162}Er at 26.8 % has been pre-purified and irradiated together with some leftovers from the first batch and is currently stored awaiting for a precise ICP-MS measurement in order to assess the exact ^{163}Ho produced. This is a rather important quantity which not only will provide information on the overall efficiency of the purification and irradiation process, but will also provide information on the yet unknown burn up cross section. From a ICP-MS measurement performed at PSI which gave information on the ^{165}Ho/^{163}Ho ratio and on the ^{165}Ho/^{166m}Ho ratio, it should contain a total activity of 30 MBq of ^{163}Ho.

The third batch of 538 mg enriched in ^{162}Er at 25.1 % will be irradiated in 2017 together with some extra material from the previous purifications.

6.3 Embedding process

6.3.1 Target production

In order to fix the ^{163}Ho in the absorber of the detectors a custom ion implanter will be used. The implantation process will be carried out by accelerating ^{163}Ho ions emitted from a source towards the end station where the detectors will be located. The metallic cathode for the ion source will be made out of a metallic holmium containing ^{163}Ho. The cathode will be actually produced by compressing the ^{163}Ho metal powder with a mixture of Nickel-Titanium powder into a ring shape which will be installed in the implanter. Ni and Ti are used for Oxygen absorption in order to avoid the dangerous oxidation of the metallic Ho. Additionally, in order to produce a ring shaped target with sufficient mechanical stability, extra Sn is added at the metallic powder before compression. In Figure 6.8 the result of the very first test using a cylindrical shape target can be seen.

Figure 6.8: First test of the target production. *Left*: the press used for the target production 350 bar/cm^2; *right*: the first test of target production with cylindrical shape.

The $^{163}Ho_2O_3$ powder purified after irradiation needs to be reduced to metallic form and distilled. The reduction and distillation process is achieved by heating the mixture of yttrium and holmium oxide above the melting point. A Tantalum heated Knudsen cell is used for the reduction and distillation of holmium from the Er_2O_3. Holmium is reduced at 2000 K through the reaction Ho_2O_3+2Y(met)$\longrightarrow$ 2Ho(met)+Y_2O_3. A new thermally optimized cell has been designed and installed in a new evaporation system set-up. The system has been successfully running since February 2016 and it is currently being tested and optimised. Tests are in progress with natural Ho_2O_3 to tune the reduction process and assess the overall efficiency.

The ^{163}Ho custom ion implanter is shown in Figure 6.9. The implanter is composed of an ion source which extracts ^{163}Ho ions from a metal target by Ar plasma sputtering. The ^{163}Ho are then accelerated and directed towards the magnetic selector and focusing sectors.

The Ar plasma will extract Ho atoms from the source by sputtering and the free atoms will than be ionised by and ECR source in order to accelerate them towards the selection sector. Since the rate of extraction will be set by the density of the Ar plasma, in order to obtain the desired ^{163}Ho deposition rate of 1 μA, the chemical composition of the target must be carefully studied. It is in principle possible to dilute the ^{163}Ho with ^{165}Ho and other metal compounds such as Sn in order to reduce the current on the target. It is then clear that the selection magnet will play a crucial role in separating the the ^{163}Ho from any other atomic species in the target. The major threat for the neutrino mass measurement would be the presence of ^{166m}Ho, which decays with a low energy beta spectrum that represents a background to the EC capture spectrum of ^{163}Ho, yet one does not want to implant ^{165}Ho either, even though it is harmless from the radioactivity point of view, since it will add extra heat capacity which could eventually spoil the performance of the detector.

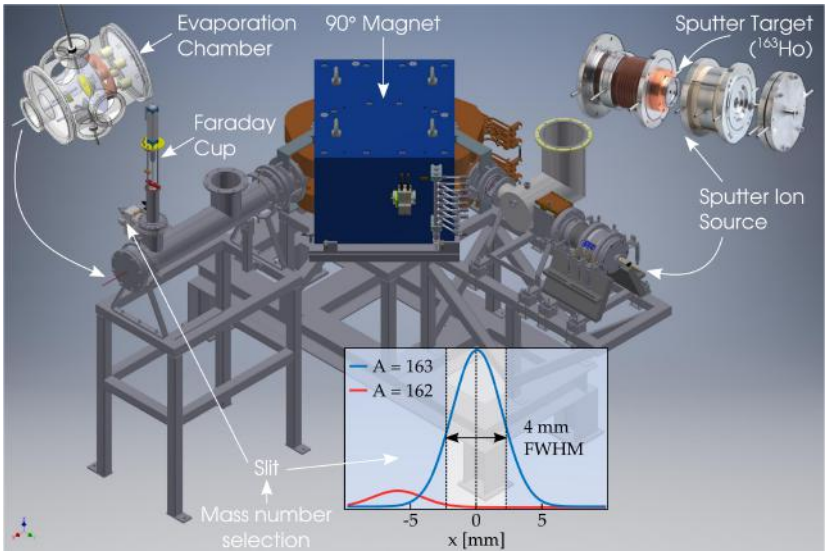

Figure 6.9: The HOLMES custom ion implanter: from right to left, the Penning sputter ion source, the steering magnet, the mass analyzing magnet, and the evaporation chamber.

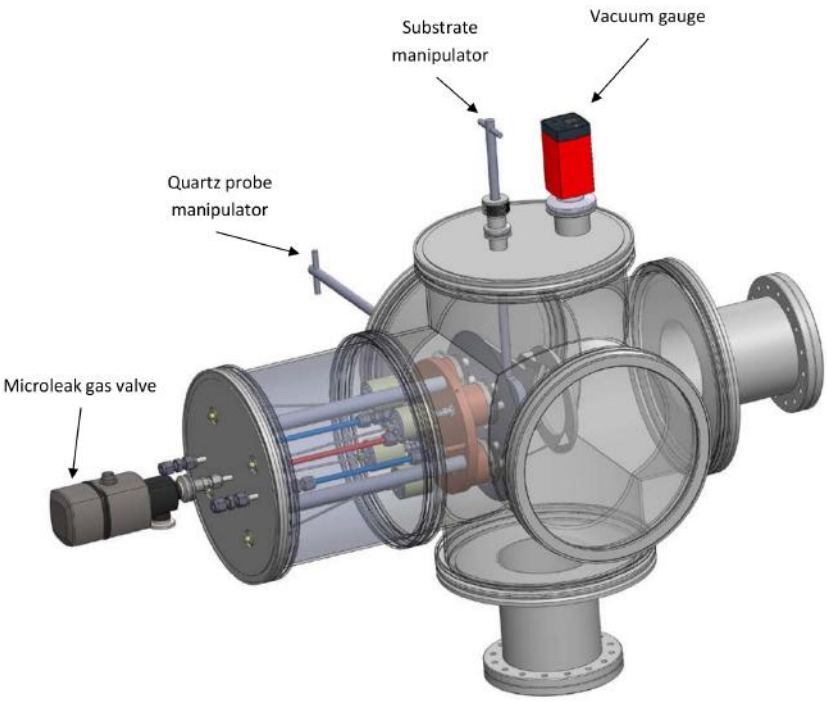

Figure 6.10: Preliminary design of the end point station with the detector holder. The general structure based on a NW200 6 ways cross. The beam will enter the chamber from the right side, while on the opposite side the deposition system will be mounted.

The magnetic selector is a dipole magnet that bends the ion beam in order to separate and select ^{163}Ho mainly from ^{166m}Ho and any other contaminating isotope which has not been removed by the purification process at PSI. After the selection sector the beam is focused in order to maximise the geometric efficiency on the target. After the bending sector a selection slit will separate the ^{163}Ho component of the beam from the neighbouring mass isotopes. The selected ^{163}Ho ions will be focused and will hit the detector array. The kinetic energy of the ions will be tuned so that the beam will penetrate the first atomic layers of the gold absorber. The beam will sweep over the whole array several times in order to obtain the most uniform density of ^{163}Ho atoms. In order to keep the ^{163}Ho density uniform and to preserve the lattice structure of the absorber, Gold must be sputtered on the absorber while ^{163}Ho is implanted. In the target chamber, behind the array holder, a special Gold sputtering system will be installed in the end point station where the detectors will be in place, as shown in Figure 6.10.

The sputtering system consists of an ECR generated plasma hitting a gold target which will then sputter on the detectors while the beam is sweeping. The design of the target chamber is being finalised now, as can be seen in Figure 6.11, by the Milano working group before being integrated in the implanting system which will be set up in Genova in 2017. The geometry of the final HOLMES detectors array will be defined according to the beam diameter at the end station of the implanter in order to maximise the geometric efficiency.

It is of crucial importance to tune the current of the ion beam with the sputtering rate in order to keep a uniform density of ^{163}Ho inside the absorbers and, once the implantation is over, to deposit the 1 μm thick Gold layer.

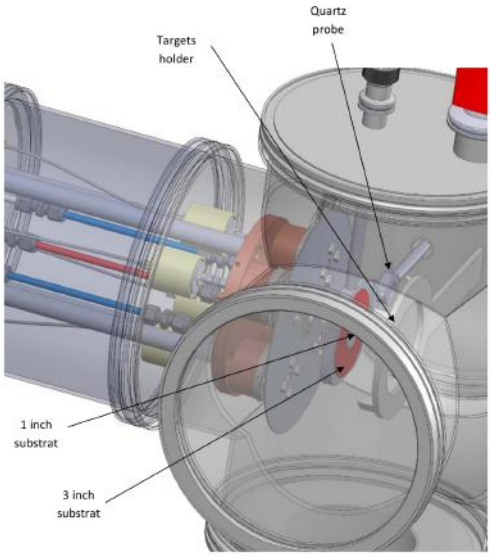

Figure 6.11: Close up of the deposition system. The detector chip will be held in place on the 1 inch substrate and the Gold sputtering targets will be mounted on the target holder. The ^{163}Ho beam will pass through the target holder and will stop on the detectors together with the sputtered Gold.

6.3.2 Final processing

After the detectors have been implanted one last step is necessary before the actual low temperature operation: the silicon underneath the detectors has to be etched in order to release the Si_2N_3 membrane with the detectors on top. This process will be performed using a deep reactive ion etching. The details of the process are being defined in collaboration with CNR Roma.

Chapter 7

Detectors characterisation

In the following paragraphs I will outline the work to measure the prototype detectors produced at NIST that have undergone intensive testing both at NIST and in Milan-Bicocca. I have set up a new readout system in a new dry dilution refrigerator in order to be able to measure TES coupled to rf-SQUIDs.

7.1 Experimental setup

I had to build up an entirely new set up for the TES detectors and adapt an existing microwave read out system for measuring the multiplexed rf-SQUIDs. I started by assembling a special detector holder to be coupled to the mixing chamber of a ^{3}He-^{4}He dilution refrigerator facing a radioactive source. I first performed a characterisation of the microwave readout system studying the resonances of the multiplexing chip; I could then acquire and demodulate the rf-SQUID response, which allowed me to perform specific studies on the SQUIDs; finally I focused on the characterisation of TES response and on the study of the TESs performances. I was finally able to set up each detector at a proper working point so that I could perform calibration runs with ^{55}Mn K-alpha and a multi-line X ray emitting source in order to assess important issues such time and energy resolution and detector linearity.

7.2 Multiplexed Readout

In order to measure the SQUID voltage output, the SQUID itself is coupled to a quarter wavelength resonator transforming the signal into a phase shift of a traveling wave trough the microresonator. This is achieved by coupling the SQUID to the inductive load of the LC resonator as can be seen in the scheme of the readout circuit shown in Figure 7.1.

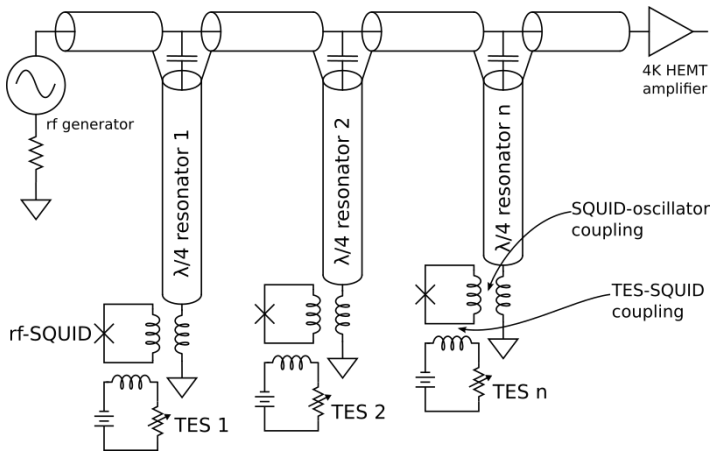

Figure 7.1: The circuit diagram of the multiplexed readout: each TES is coupled to a SQUID; a change in the SQUID flux changes the load of the resonating circuit shifting its frequency. The frequency shift can be precisely measured using the homodyne technique

The information coming from the superconducting microwave microresonators is accessed with the homodyne mixing technique. The signal that has to be demodulated is mixed with a reference signal. The characteristic of the homodyne readout method is that one signal is mixed with the exact copy of itself. In order to perform the mixing and the downconversion, a special circuit, shown in fig. 7.2 [59], is necessary. At the cold stage, the signal passes through several resonators tuned to oscillate with different frequencies, than it is remixed with its own copy.

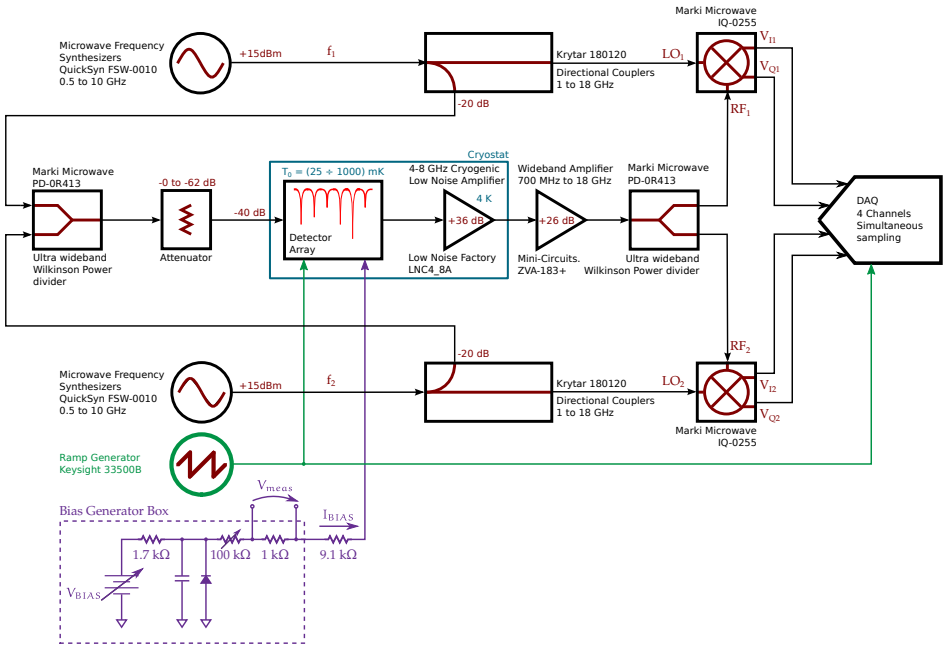

Figure 7.2: The circuit diagram of the homodyne setup used to read out the superconducting microwave microresonators coupled to the TES. The ramp circuit and the TES bias circuit are independent.

This is practically achieved generating a probe signal with a microwave synthesizer which is then split in two components by a directional coupler. One of the two signals is sent to the LO port of the IQ mixer, while the attenuated signal is sent via a coax cable to the multiplexing chip inside the refrigerator. The wave then travels through the feedline coupled to the resonators and after being amplified by two microwave amplifier (one HEMT) it goes into the RF port of the IQ mixer. The ideal IQ mixer has two output values: the real component of the transmission signal on the first channel, namely the I channel, and the imaginary component on the second channel, namely the Q channel. Combining I and Q is it possible to retrieve the amplitude A and the phase ϕ of the original signal through the equations

$$A = \sqrt{I^2 + Q^2} \tag{7.1}$$

$$\phi = \tan^{-1}\left(\frac{Q}{I}\right) \tag{7.2}$$

7.2.1 Cryogenic set up

The signal of an rf-SQUID is read out using a homodyne system described in the following paragraph. Before the very first SQUID test we had to instrument the dilution refrigerator with the necessary wiring and electronic components needed to effectively read out the rf-SQUID. The scheme can be seen in Figure 7.3. The probe signal runs from room temperature to the 4 K stage through Cu-Be cables, in order to limit the heat load due to the big temperature difference between the stages. After a 20 dB attenuation at 4 K in order to match the

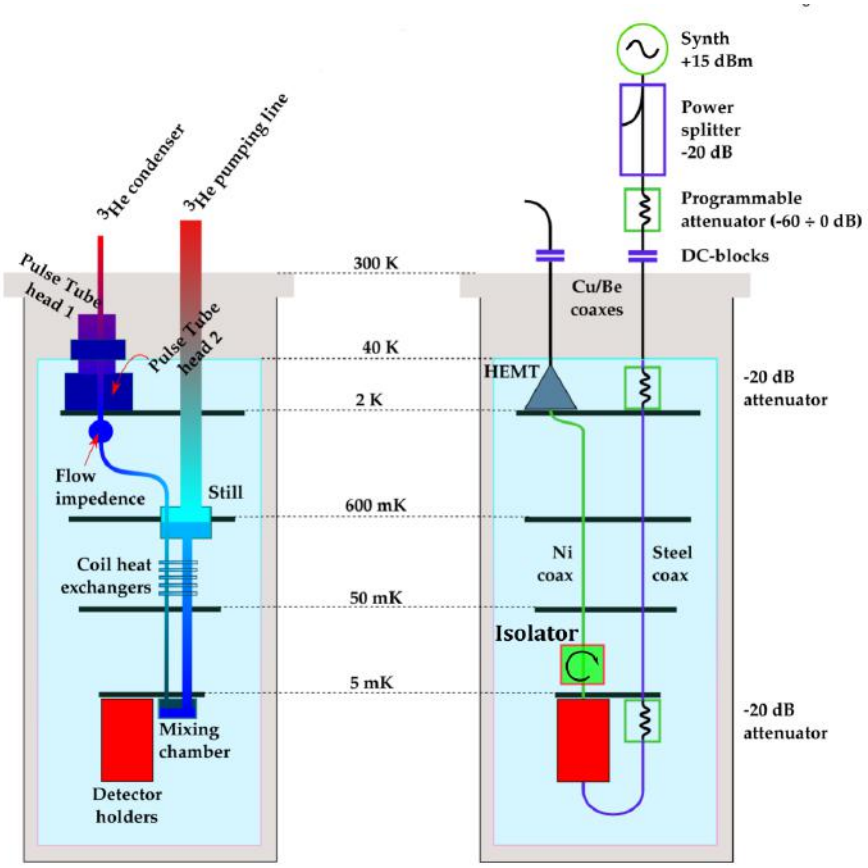

Figure 7.3: Scheme of the electronic setup inside the cryostat

thermal noise to the temperature difference, the signal is carried to the detectors through stainless steel cables which have a reduced thermal load on the coldest stage, where the detectors are. Before actually entering the detector box, the probe signal is further attenuated by 20 dB. After passing through the detector the signal has to be recovered to room temperature, where all the readout electronics are. From the cold stage until the 4 K stage, the signal first passes through a circulator configured as an isolator to eliminate any eventual reflection acting as an isolator, then the signal is carried with Nb coax cables, which is superconductive and avoids signal attenuation and has a very low thermal conductance. At 4 K a special cold HEMT (High Electron Mobility Transistor) amplifier is mounted. The critical parameter of the amplifier is its noise temperature, as can be seen in Figure 7.4, which has been especially chosen for high resolution spectroscopy. From the amplifier output to room temperature, the signal is again carried with Cu-Be cables, before reaching a further room temperature amplifier, which has a gain of 26 dB over a band ranging from 700 MHz to 18 GHz.

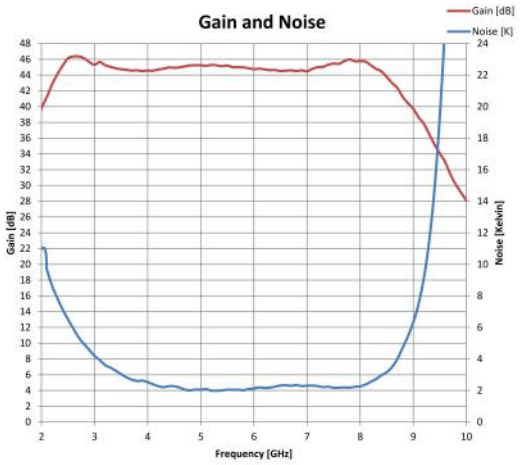

Figure 7.4: Noise and gain of the HEMT amplifier mounted on the rf circuit at the 4 K stage of the cryostat

7.2.2 IQ mixer

The in-phase signal results from directly mixing the RF (Radio-Frequency) with the LO (Local Oscillator), while the quadrature signal Q is obtained from mixing the RF with the LO phase-shifted of $\pi/2$, as pictured in Figure 7.5.

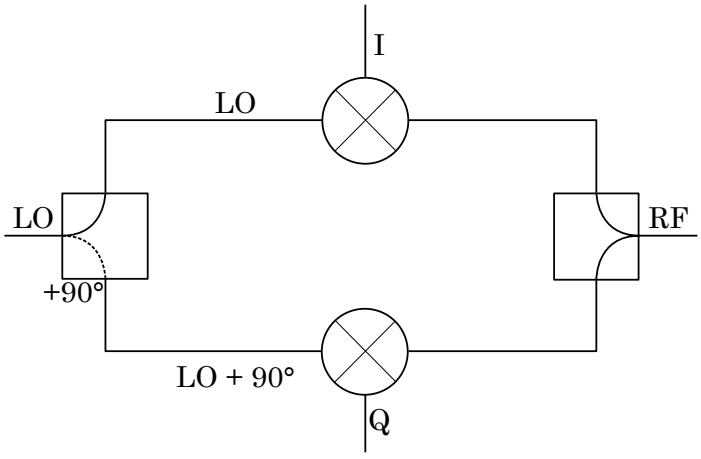

Figure 7.5: An IQ mixer: the quadrature signal Q is obtained by shifting of $\pi/2$ the phase of the LO, while the in phase signal I is obtained by mixing the LO signal with the RF signal.

In a homodyne configuration the LO and the RF have the same frequency. The only quantity which is different between the two signals is the phase

$$V^{LO} = V_0^{LO}\cos(\omega t) \tag{7.3}$$

$$V^{RF} = V_0^{RF}\cos(\omega t + \phi_0) \tag{7.4}$$

Analytically, the I signal is computed by the mixer as the product between the two input signals:

$$\begin{aligned} V_I \propto V^{LO}V^{RF} &= V_0^{LO}V_0^{RF}\cos(\omega t)\cos(\omega t + \phi_0) \\ &= \frac{1}{2}V_0^{LO}V_0^{RF}\left[\cos(2\omega t + \phi_0) + \cos(\phi_0)\right] \end{aligned} \tag{7.5}$$

A low pass filter will cancel the radio-frequency term, making the I response to be the real component of the complex RF signal.

$$V_I \propto \frac{1}{2}V_0^{LO}V_0^{RF}\cos(\phi_0) \tag{7.6}$$

On the other hand, the Q signal is computed in the same way, accounting in this case for a 90° shift on the LO signal:

$$V^{LO} = V_0^{LO}\cos\left(\omega t + \frac{\pi}{2}\right) \tag{7.7}$$

So the product between the RF and the LO signals in this case yields

$$\begin{aligned} V_Q \propto V^{LO}V^{RF} &= V_0^{LO}V_0^{RF}\cos\left(\omega t + \frac{\pi}{2}\right)\cos(\omega t + \phi_0) \\ &= \frac{1}{2}V_0^{LO}V_0^{RF}\left[\cos\left(2\omega t + \phi_0 + \frac{\pi}{2}\right) + \cos\left(\phi_0 - \frac{\pi}{2}\right)\right] \\ &= \frac{1}{2}V_0^{LO}V_0^{RF}\left[-\sin(2\omega t + \phi_0) + \sin(\phi_0)\right] \end{aligned} \tag{7.8}$$

The low frequency Q signal will be then proportional to the imaginary component of the RF signal:

$$V_Q \propto \frac{1}{2}V_0^{LO}V_0^{RF}\sin(\phi_0) \tag{7.9}$$

The output of the two mixers is then amplified again before being digitised using a National Instruments 16 bit ADC. We have developed a special two stage, four channels wide band amplifier for the I and Q signal before digitalisation. These amplifiers have been tested in order to operate them with ramp frequencies up to 100 MHz, as can be seen in 7.6.

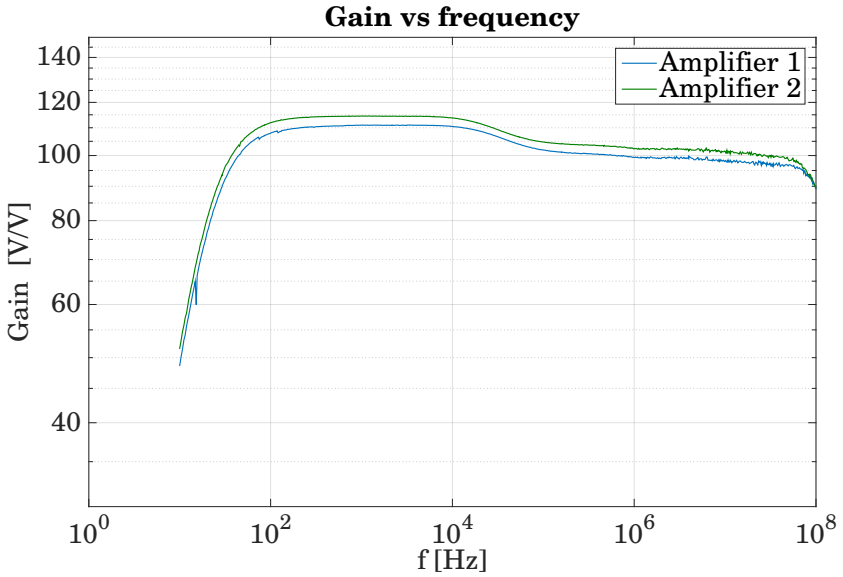

Figure 7.6: Gain of the IQ amplifiers placed before the acquisition board.

The readout is practically achieved by acquiring the voltage output I and Q, from which the SQUID response is reconstructed offline.

7.2.3 Signal reconstruction and processing

The I and Q outputs are digitised and acquired over time in order to enable the offline signal reconstruction. As described in Chapter 5.3.1, the rf-SQUID is operated in flux ramp modulation mode and offline processing algorithms are necessary in order to reconstruct the signal in time. We apply a periodic ramp that sweeps through multiple flux quanta in the SQUIDs, and require the slew rate of this ramp to greatly exceed that of any expected input signal. An input signal therefore looks like a flux offset during the duration of the ramp and produces a phase-shift ϕ in the oscillating SQUID response Φ, which is calculated with respect to a reference oscillation

$$\phi = 2\pi \frac{\Phi}{\Phi_0} \tag{7.10}$$

From I and Q we reconstruct the phase shift Φ of the SQUID corresponding to each ramp cycle, subsequently we extract a value ϕ which is used to reconstruct the signal $\phi(t)$. The ramp is generated with a programmable function generator and sent to the SQUID. During the first tests we saw a noise contribution at 50 Hz due to the ramp generator, we studied a decoupling method in order to isolate the ramp generator from the cryostat. We constructed a circuit with a series of three isolation amplifiers with inductance L=350 µH (type: WE-MIDCOM 749012011 HT1526, shown in Figure 7.7); each isolation amplifier contains two transformers, six in total, which have to be activated in order to adjust the transfer function of the filter to the ramp frequency set by the user. It is important to select the proper bandwidth in order not to generate distortions of the ramp.

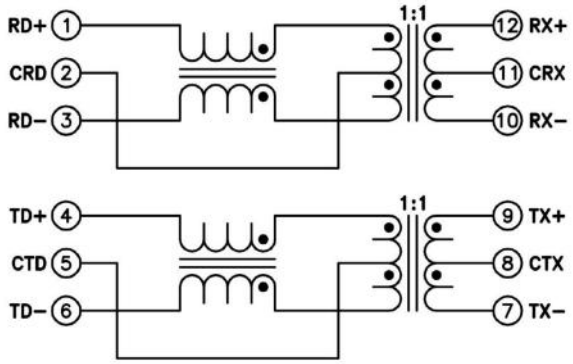

Figure 7.7: Isolation amplifier WE-MIDCOM 749012011 HT1526 circuit scheme

We have performed tests on the amplifiers in order to set the number of transformers needed for different ramp frequencies. The adjustable transformers are 2, 4 or 6, since every amplifier is composed by two. In order to set the relationship between number of active transformers and the bandwidth of the filter we have performed a frequency characterisation of the devices. An example of the transfer function for 4 active transformers is shown in Figure 7.8.

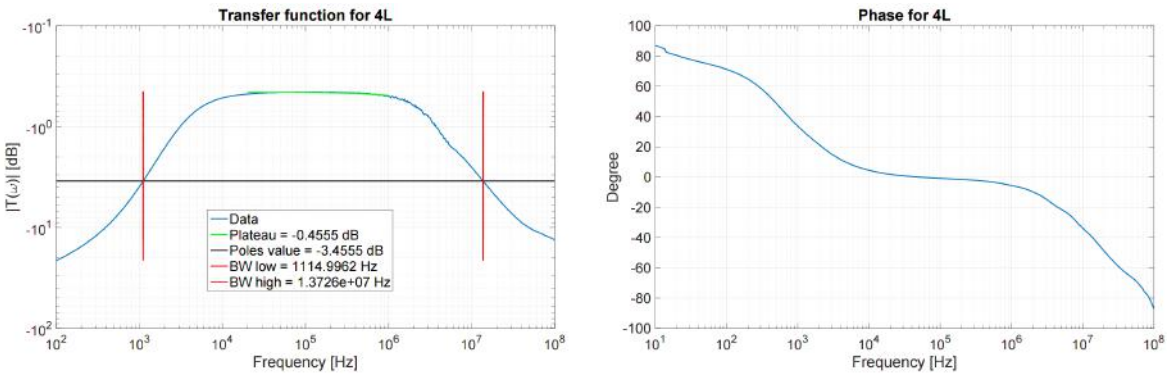

Figure 7.8: Example of the transfer function for 4 active transformers. *Left*: isolation amplifier transfer function; the poles coordinates have been calculated at the transfer function value 3 dB below the central flat region. *Right*: phase of the transfer function.

The results of the bandwidth test are shown in Table 7.1. After measuring the effective bandwidth we performed a simulation of the response to an input ramp function. Finally we tested the decoupling amplifier response to an effective 1 MHz ramp. The results are shown in Figure 7.9. We can see that a 1 MHz ramp, which is double the frequency needed for HOLMES has no distortion after passing through the amplifier; besides any DC current is screened, as can be seen both in the simulation and in the measurements, since the ramp is centered at V=0. With the new decoupling system we were able to eliminate the noise contribution due to the ramp generator.

Active transformers	Low pole [kHz]	High pole [MHz]
2	2.262	25.34
4	1.115	13.73
6	0.727	0.96

Table 7.1: Bandwidth limits for each number of active transformers.

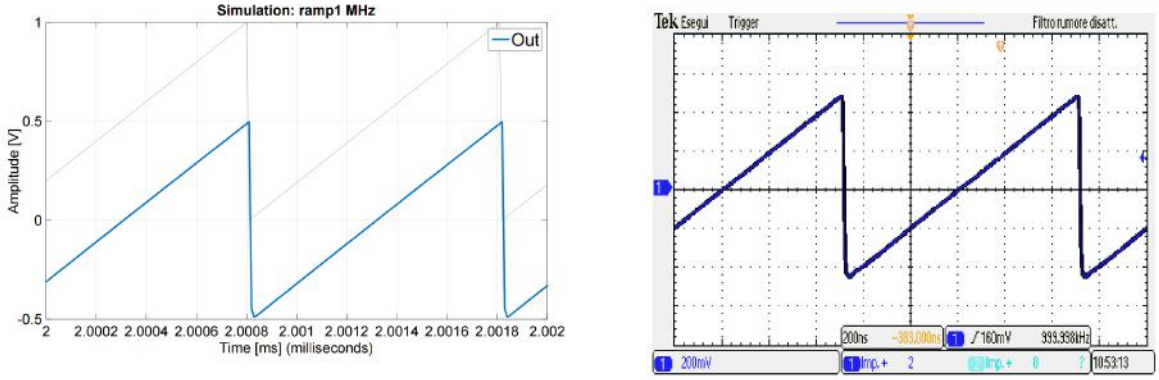

Figure 7.9: Amplifier ramp test. *Left*: simulation using the measured transfer function for two active transformers. *Right*: Measurement of the amplifier output with an input 1 MHz ramp.

7.3 First tests

We started testing the TES and the multiplexing system with an array of standard Bismuth TES provided by NIST together with a multiplexing chip that allowed us to optimise the measuring system, the data acquisition, and the analysis process. The first version of the holder and the detectors are shown in Figure 7.10. In the blue box there is the first array of 20 standard TESs with Bismuth absorber, while in the red box, there is the interface chip on which, there are the shunt resistors and a selectable range of four Nyquist inductance values.

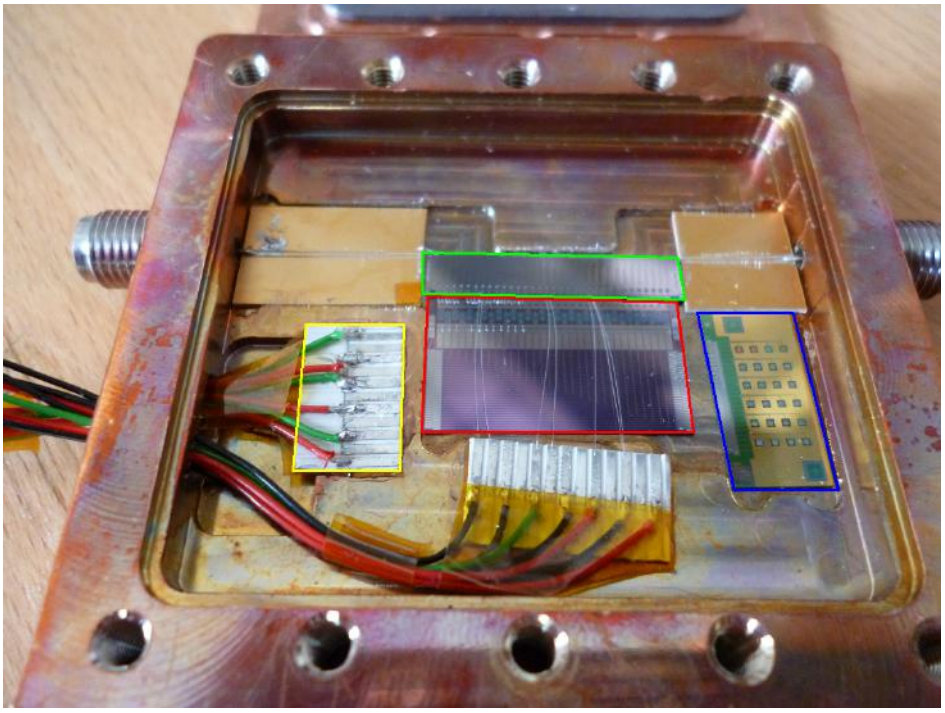

Figure 7.10: First version of the chip holder with the detectors and multiplexing chip mounted. In *blue* the TES chip; in *yellow* the multiplexing chip and the contact pad for connecting the ramp and the bias line; in *red* the interface board, where the shunt resistors and the stray inductance are.

During this first phase the DAQ we were using had a maximum sampling rate of 2.5 MHz, which did not allow us to use a ramp frequency higher than 62.5 kHz. Due to the slow effective sampling rate during these first test we were only able to measure slower detectors. This was possible using a higher value of inductance, 610 nH and 250 nH.

These measurements were the first ones we did using a microwave multiplexed TES detector. We had to develop a whole new acquisition and analysis software which allowed us to characterise the detectors and to tune the acquisition parameters before data taking. We adapted the demodulation software for acquiring, processing and displaying the SQUID response so that we could control and tune the parameters of the ramp modulation system, namely the RF frequency, the ramp frequency and the ramp amplitude. We then developed a special acquisition tool for an online noise power spectrum analysis and an oscilloscope to monitor the detector response live. Finally we developed a special software tool for the automatic acquisition and processing of the IV characteristics curves of the TES.

7.3.1 I-V characterisation

In order to operate and properly bias a TES, some preliminary operations are necessary. The goal is to choose the proper bias current in order to optimise the signal to noise ratio. Each current value sets a different steady state of the TES through the transition. In order to choose the optimal point we need to study the TES resistance at varying bias currents. Operationally we achieve this by performing a current sweep from higher bias current val-

ues towards lower currents and recording the TES response through the transition. The TES resistance cannot be assessed directly but has to be calculated: the typical I-V curve can be separated into three distinct regions: the high bias region, where the TES is resistive and acts as an ohmic material, the low bias region, where the TES is purely superconductive and the transition region. From the superconductive region it is possible to extrapolate the current to flux conversion factor, assuming the superconducting TES resistance to be 0, while from the resistive region it is possible to extrapolate the normal resistance value of the TES by assuming the TES to behave like an Ohmic resistor and knowing R_{sh}.

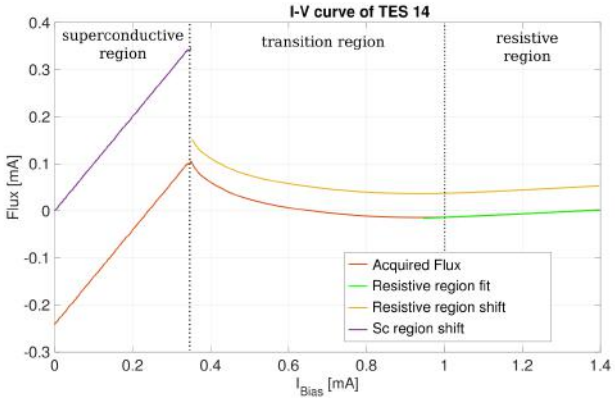

Figure 7.11: A processed I-V curve for a TES, with different regions highlighted, from the slope of the superconductive region the current to flux conversion factor can be measured $\mu A/\Phi_0$, from the resistive region, the TES resistance is measured.

The first SQUIDs we were using had a conversion factor of 9 $\mu A/\Phi_0$

Finally, one can plot the TES resistance vs the bias current and choose the optimal bias point. A common choice is to keep the TES around 30 % of the normal resistance value, because of the good linearity and dynamic range of the detector.

7.3.2 First tests results

After the initial runs when we developed, debugged and optmised the experimental setup and the read out, I could cool down and characterise the Bi-TES detector.

During this first measurement phase we saw that the detectors were thermally drifting on the long time scale, so we have improved the thermal stability of the detector box by decoupling it from the Mixing Chamber stage of the cryostat where it had been previously mounted, as can be seen in Figure 7.12 and by setting up a weak thermal connection to the cryostat cold stage. In this configuration we were able to thermally stabilise the holder temperature by mounting a thermometer and a heater directly on the copper box so that we could set up an externally controlled thermal feedback. With the decoupling and independent stabilisation we were able to reach impressive results even with these first detectors. These were indeed the first TES read out using the microwave multiplexing technique to be used for high resolution X ray detection.

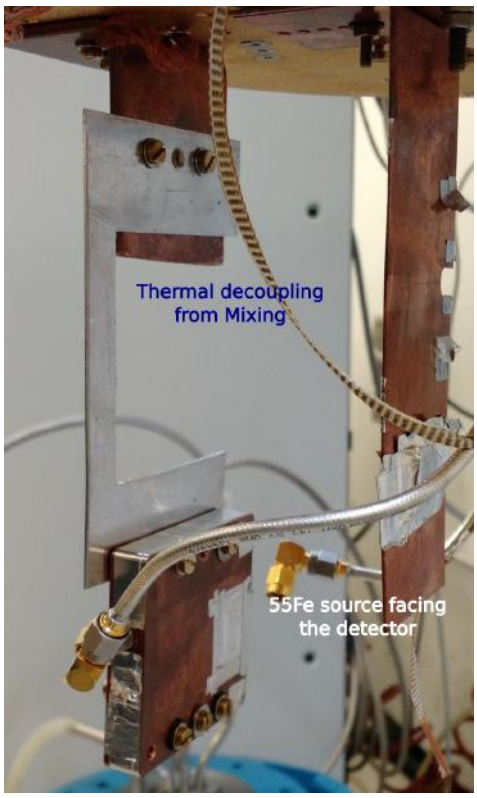

Figure 7.12: First thermal decoupling of the detector: the picture was taken before mounting the copper wire which provided the weak thermal connection to the cold stage.

We then studied the signal to noise ratio (SNR) and the effective energy resolution illuminating the detectors with X rays from a ^{55}Fe source, as function of the working point, at a chosen temperature 50 mK. Some results of the resolution as a function of the working resistance are shown in Table 7.2. The fit of the spectra at the optimal working point is shown in Figure 7.13.

Working point R %	SNR	Optimal Filter res at 5.9 keV [eV]	Measure res at 5.9 keV [eV]
10	1093	5.4	10.6
20	1376	4.3	10.3
30	1407	4.2	9.1
40	1324	4.5	21.5

Table 7.2: Bi-TES characterisation: signal to noise ratio, expected (corrected for detector nonlinearity) and measured resolution at the 5.9 keV peak of ^{55}Fe. The difference between expected and measured is due to unidentified noise $\sim 1/f$ at low frequencies.

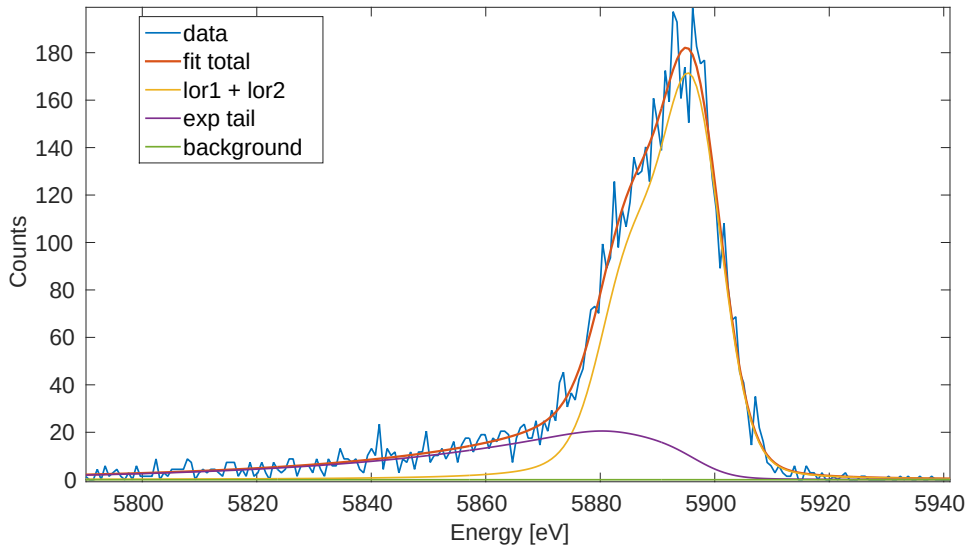

Figure 7.13: Fit of the 5.9 keV peak obtained illuminating the first TES array with X rays from ^{55}Fe. The Bismuth detectors present a tail towards lower energies due to the thermalisation process in the absorber. A special fitting function was developed in order to take into account the lower energy tail. The achieved resolution after offline stabilisation was 9.1 eV FWHM.

In order to fit the 5.9 keV peak a special tool was developed. ^{55}Fe decays via electron capture to ^{55}Mn. The K-α line has a fine structure which needs to be taken into account in the peak fitting algorithm. The 5.9 keV double peak is lorentzian but due to the finite detector resolution, in order to fit it, it is necessary to use a lorentzian function convolved with a gaussian function. In the fitting algorithm the peak positions, ratio and intrinsic width are fixed, while the resolution is left as a free parameter.

While the test runs with the Bismuth-TES were ongoing we bought and set up a fast DAQ with sampling rate of 250 MHz, which allowed us to increase the ramp, and hence

the sampling frequency up to 250 kHz. The new DAQ was ready when NIST shipped to Milan the multiplexing chip specifically optimised for HOLMES and the prototypes of the HOLMES TES.

7.4 Multiplexing chip 16A

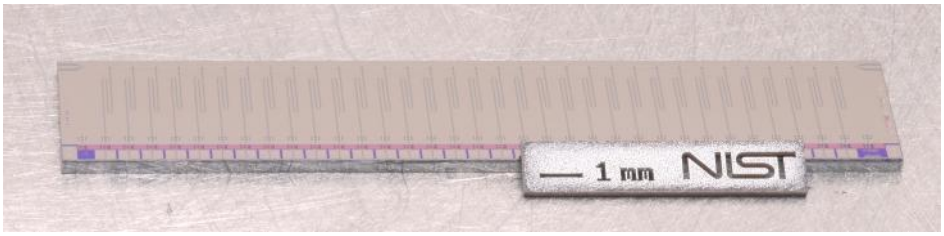

Figure 7.14: Chip μMux 16A with the array of rf-SQUIDs coupled to the quarter wavelenght resonators

μMux 16A (Figure 7.14) is the version of the multiplexing chip used for the initial tests with the HOLMES TES. The chip is design to have 33 different resonators coupled to the same feedline. I have measured 32 separate resonances, with one resonance overlap; the transmission function S_{21} can be seen in Figure 7.15. For simplicity each resonance can be as well represented in a (I, Q) plane; for this representation, the resonance shape is a circle and the SQUID oscillation is an arc on the resonance circle.

In order to evaluate the bandwidth I have acquired S_{21} over a wide frequency range, set boundaries for each resonance and fit it. An example of a fitted resonance is shown in Figure 7.16

Two resonances were too wide and the fit did not converge. In the Figure 7.17 the distribution of the calculated bandwidths can be seen. The bandwidth of 6 out of the 32 measured resonances was below 1 MHz; this can be ascribed at fluctuations in the coupling factor Q due to reflections of the microwave probes. This is probably due to impedance mismatches on the transmission line which generate standing waves along the feedline. We will try improving the coupling of the chip to the feedline by reducing the length of the bonding wires. Besides, in order to obtain a regular and reproducible resonance spacing, the next chip will be fabricated using a single mask section repeatedly for all the couplings to the feedline of the 33 resonators in order to guarantee a good tuning of each resonance frequency.

Concerning the frequency separation, which can be easily evaluated from S_{21}, the resonances are averagely spaced by roughly 15 MHz; even though some resonances have clearly shifted from their design frequency, as can be seen in the distribution plotted in Figure 7.18. This is a minor concern at the moment, but needs be improved in the next chip version, which is designed to have 14 MHz spacing with placement better than 1 MHz.

The results are very promising. I successfully tested the chip and subsequently used it for reading out TES detectors sampled at 500 kHz, as required by HOLMES.

Channel	frequency ω_0 [GHz]	BW [MHz]
1	5.6425	0.0000
2	5.6647	1.3631
3	5.6739	1.4589
4	5.6866	1.2123
5	5.7082	0.8827
6	5.7175	0.7496
7	5.7342	0.9159
8	5.7504	1.2350
9	5.7608	1.5846
10	5.7789	1.5715
11	5.7919	1.9472
12	5.8075	1.4714
13	5.8235	0.8827
14	5.8330	0.7182
15	5.8519	0.9201
16	5.8646	2.0420
17	5.8774	3.0550
18	5.8838	1.2453
19	5.8982	1.4724
20	5.9037	1.6462
21	5.9258	1.9000
22	5.9388	1.2891
23	5.9499	1.1529
24	0.0000	0.0000
25	5.9814	3.0973
26	5.9993	2.9066
27	6.0158	2.9722
28	6.0211	2.0372
29	6.0432	1.8541
30	6.0555	1.3124
31	6.0706	1.0574
32	6.0870	1.3360
33	6.0942	3.2573

Table 7.3: List of the resonances on chip μMux 16A with central frequency and corresponding bandwidth

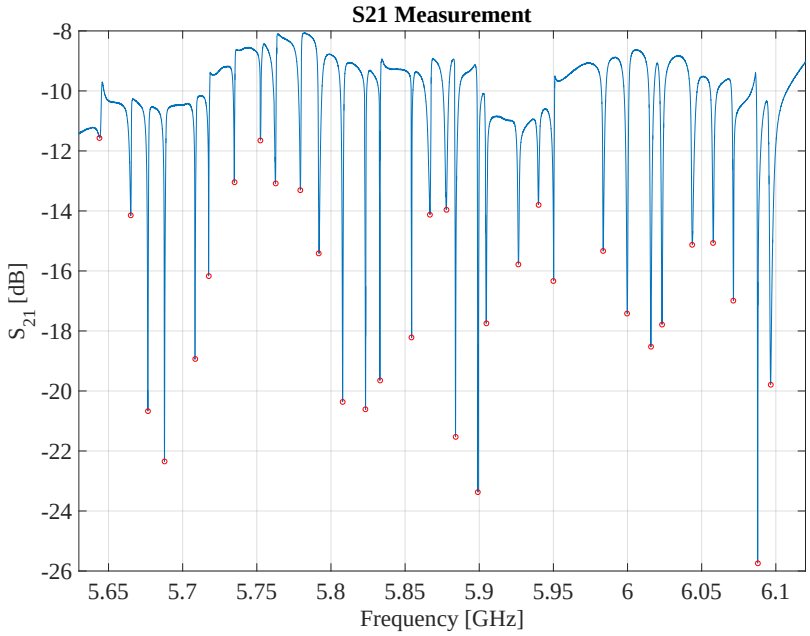

Figure 7.15: Transmission function S_{21} for the chip μMux 16A; each resonance dip is marked with a dot

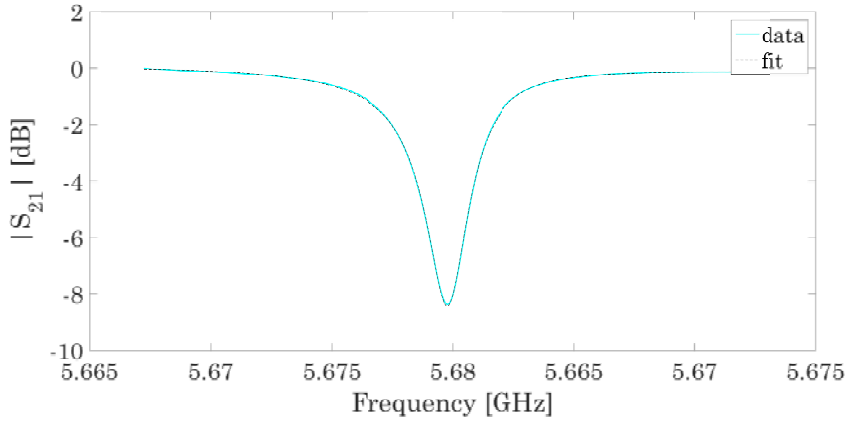

Figure 7.16: Example of one fitted resonance on the chip μMux 16A

7.5 rf-SQUID design

Coupled to every resonator there is a dissipationless rf-SQUID that transduces every change in current in the TES into a variation of inductive load of the coupled resonator. The rf-SQUID consists of a superconducting loop interrupted by layer of insulating material, the Josephson junction. The rf-SQUIDs are geometrically arranged to operate as second order gradiometers and consist of four lobes, as in a cloverleaf. Through each lobe runs the input coil and the flux ramp modulation coil as can be seen in Figure 7.19. The orientation of

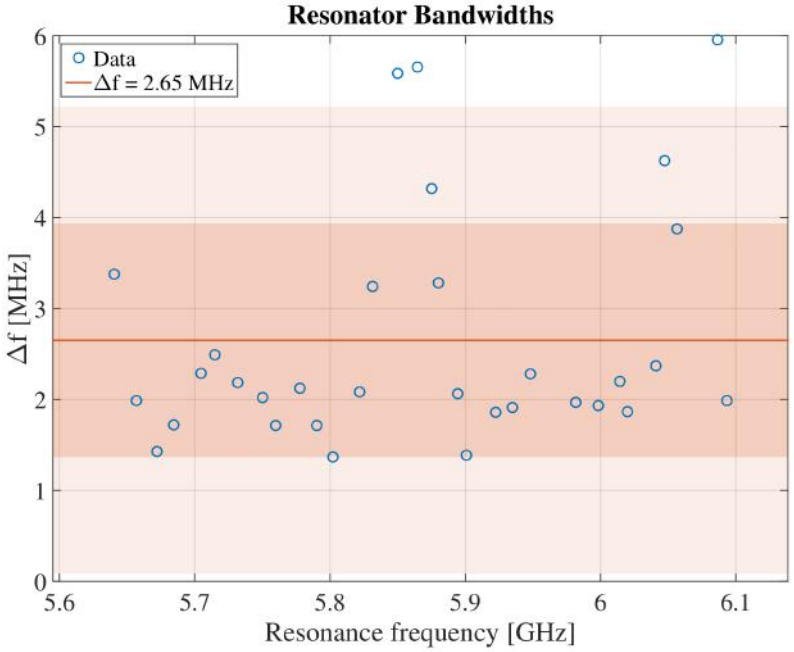

Figure 7.17: Bandwidth distribution of multiplexing chip μMux 16A, the red line indicates the 1 MHz bandwidth needed for HOLMES

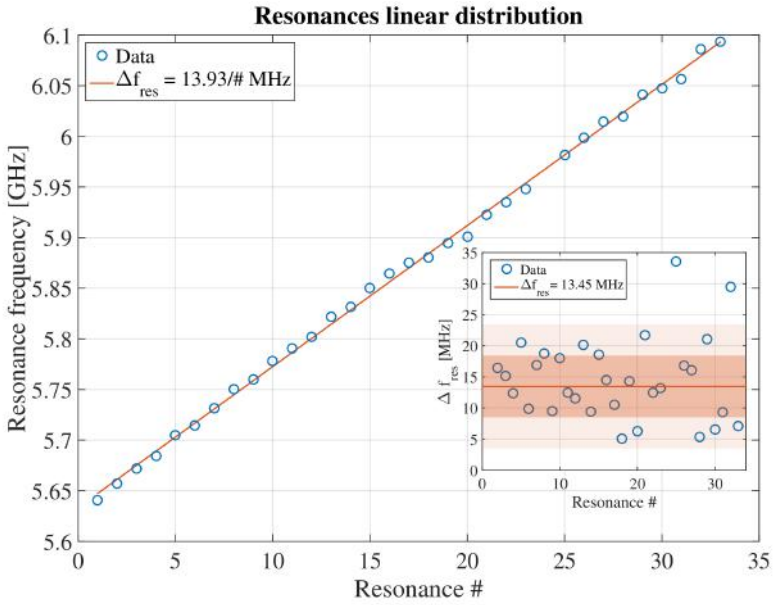

Figure 7.18: Frequency separation of resonances on multiplexing chip μMux 16A, the blue line indicates the 10 MHz separation needed for avoiding crosstalk in HOLMES

the lobes alternates around the SQUID making it insensitive to first order gradients and to uniform fields. The input coils alternate change orientation from one lobe to the adjacent

one in order to generate strong coupling to the SQUID.

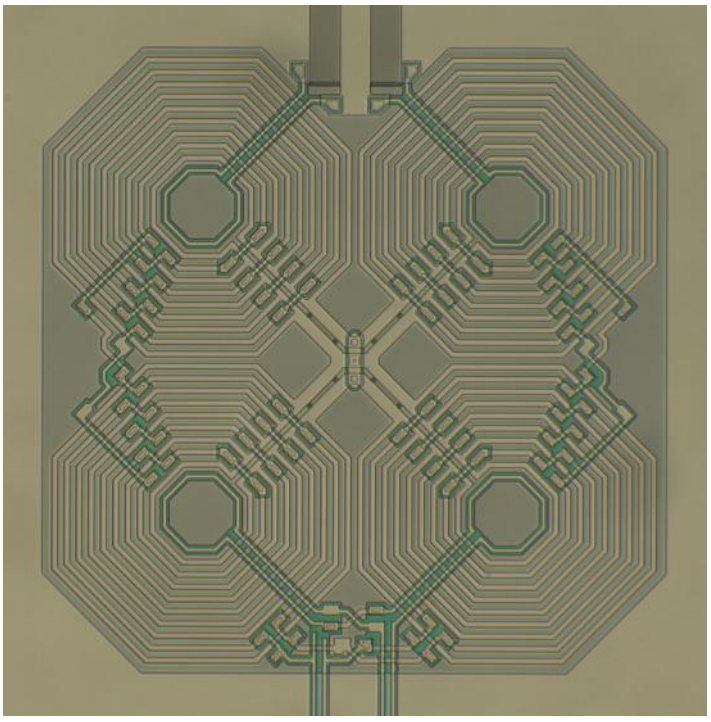

Figure 7.19: Image of a rf-SQUID from the chip 16A. The four lobes are clearly visible; the input lines at the bottom are the coupling to the TES circuit while the lines atop of the SQUID are the coupling to the RF oscillating circuit (Courtesy of NIST).

I have tested and operated the SQUID modulating with ramp frequencies up to 500 kHz; an example of the SQUID oscillation can be seen in Figure 7.20.

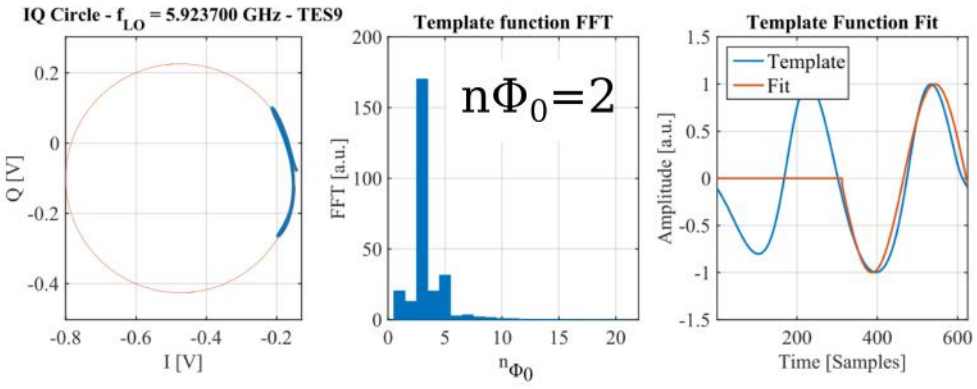

Figure 7.20: *Left* SQUID oscillation to the flux ramp modulation at 500 kHz represented in the IQ plane. *Center* Fourier transform of the SQUID response. *Right* SQUID response (and fit) used as a reference oscillation for demodulation.

For the SQUIDs of chip 16A the current to flux conversion factor is 11.6 $\mu A/\Phi_0$

7.5.1 Linearity

I have checked the linearity of the SQUID response to an externally applied flux on the input coil operating in flux ramp modulation at 500 kHz. The SQUID response can be seen in the graph shown in Figure 7.21. The error on the demodulation is of the order of 10^{-4}, as can be seen in Figure 7.22 which is perfectly within expectations.

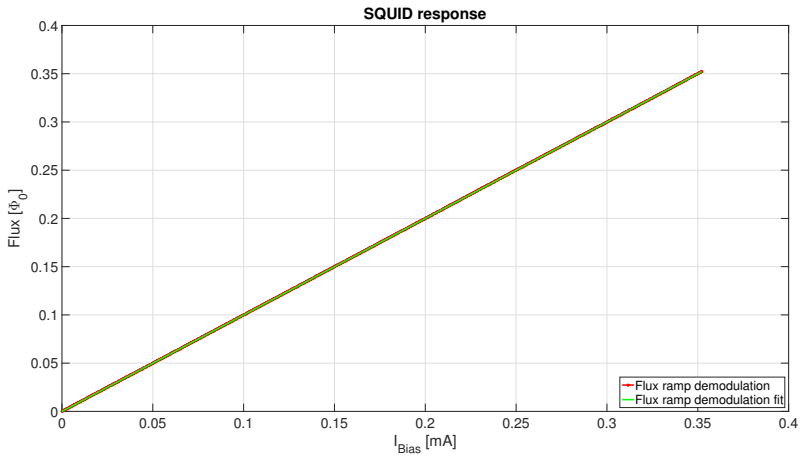

Figure 7.21: SQUID response to a variable current input signal; flux ramp modulation at 500 kHz.

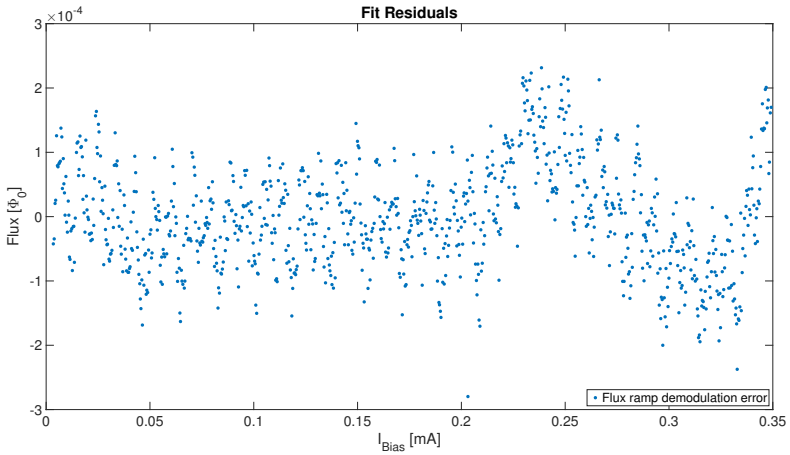

Figure 7.22: SQUID demodulation fit residuals.

7.5.2 Noise

The noise of the SQUID is measured demodulating the SQUID response with no detector connected; as an example, a power spectrum can be seen in Figure 7.23. The results for the 33 SQUIDs is reported in Table 7.4; the SQUIDs for which no number is reported were not measurable due to difficulties in demodulating the signals from the correspondent resonators. The noise level of the SQUIDs vary between 2 and 8 $\mu\Phi_0/\sqrt{\text{Hz}}$; in order not to spoil the resolution, the ideal SQUID noise should not be above 3 $\mu\Phi_0$. These results shows that there is still room for improvement in the reproducibility of the SQUIDs and multiplexing chip. The reason for the spread is the variation of the coupling to the feedline described in the previous paragraph. However these results demonstrated that the chip 16A could achieve performances which are compliant with the HOLMES specifications, since with a SQUID noise of 2 to 4 $\mu\Phi_0/\sqrt{\text{Hz}}$ it is possible to achieve the necessary SNR for ~eV energy resolution. A new improved version will be produced for the final HOLMES measurement.

Channel	frequency ω_0 [GHz]	Noise [$\mu\Phi_0$]
1	5.6425	-
2	5.6647	6.4
3	5.6739	3.4
4	5.6866	3.0
5	5.7082	2.8
6	5.7175	3.7
7	5.7342	4.7
8	5.7504	5.4
9	5.7608	-
10	5.7789	5.0
11	5.7919	3.5
12	5.8075	2.6
13	5.8235	2.4
14	5.8330	2.8
15	5.8519	3.1
16	5.8646	5.4
17	5.8774	8.3
18	5.8838	2.9
19	5.8982	2.8
20	5.9037	4.3
21	5.9258	5.3
22	5.9388	-
23	5.9499	4.5
24	0.0000	0.0
25	5.9814	8.5
26	5.9993	-
27	6.0158	3.6
28	6.0211	2.8
29	6.0432	2.8
30	6.0555	3.0
31	6.0706	4.3
32	6.0870	3.7
33	6.0942	8.0

Table 7.4: Flux noise of μMux 16A measured at 500 kHz sampling rate

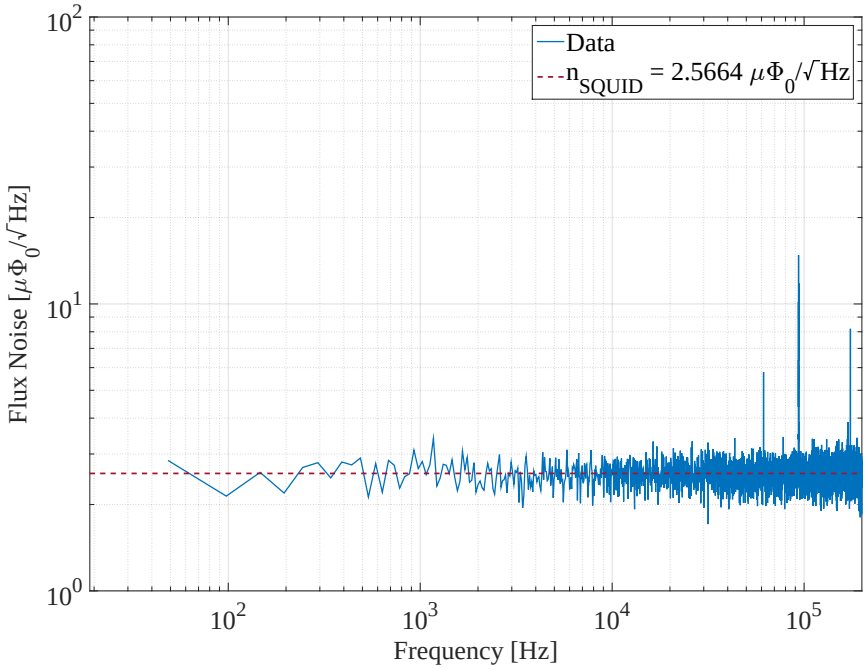

Figure 7.23: SQUID noise demodulated at 500 kHz

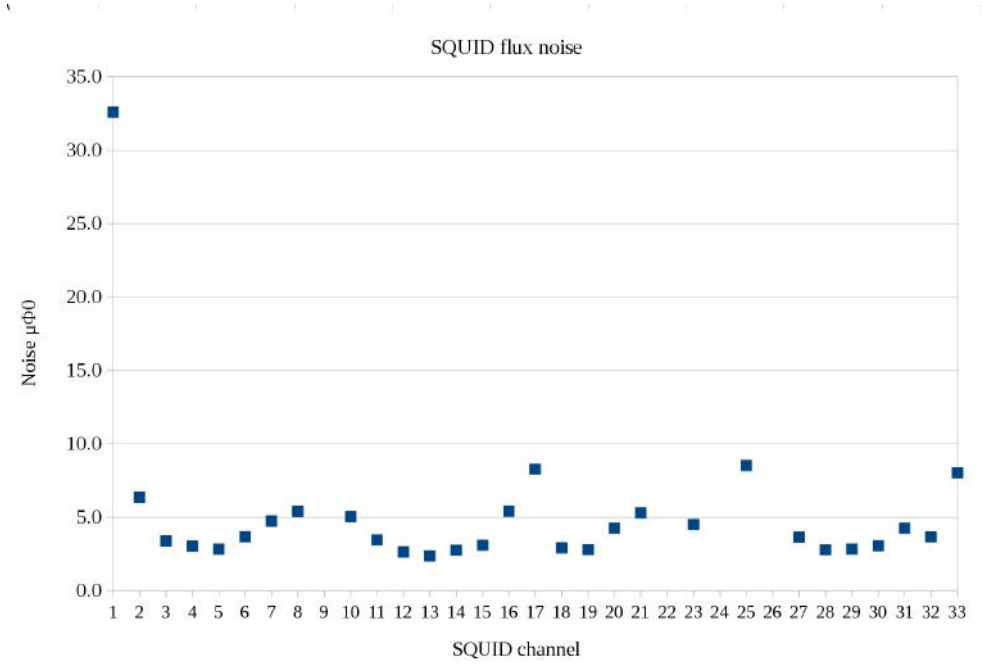

Figure 7.24: SQUID noise distribution

7.6 HOLMES TES results

The aim of putting such an effort in designing and fabricating a multiplexing chip with high performance SQUIDs and RF resonators is to ultimately read out and properly sample the signals from the 10 µs fast TES detectors of HOLMES. As of September 2016 I had measured an array of twenty TES prototypes with different configurations of thermal conductance, thermal capacity and absorber-thermometer coupling geometry. In order to connect the TES to the SQUID readout an interface (IF) chip is used. A new arrangement was studied and it can be seen in Figure 7.25. On the IF chip the shunt resistors and a selectable combination of extra indcutance are placed. For the test measurements we had an interface chip with 0.3 mΩ shunt resistors and a choice of three Nyquist inductance values in order to tune the electrical response time of the chip. In order to thermalise the TES chip and the collimator mounted on it, some Gold wires were bonded from the collimator towards the copper of the holder. In a second measurement the collimator was removed.

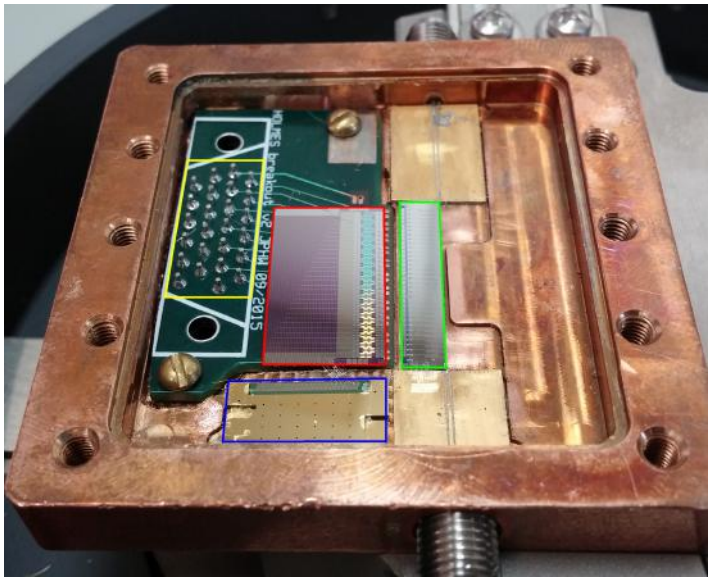

Figure 7.25: The new holder for the TES and multiplexing chip. In blue the the TES chip covered with a silicon collimator centered on the sidecar absorbers; on the right side some some Gold connections were added to thermalise the collimator and the chip underneath. In the red box the new interface chip. In green the 16A multiplexing chip. In yellow, a custom build pin board for the ramp line, the bias line and other free input lines.

Additionally, a new mounting system was built in order to keep the detector decoupled from the cold stage of the cryostat and to allow the mounting of a fluorescence source used for linearity studies. The improved system can be seen in Figure 7.26.

The multi line fluorescence source was set up using two ^{55}Fe emitters faced toward a target of Al, NaCl and $CaCO_3$ which emitted fluorescence photons from the K-α lines. A simulation was performed in order to optimise the geometrical configuration with the goal of maximising the activity on the detectors, the parameters are reported in Table 7.5. Besides, the collimator has been removed in order to increase the activity.

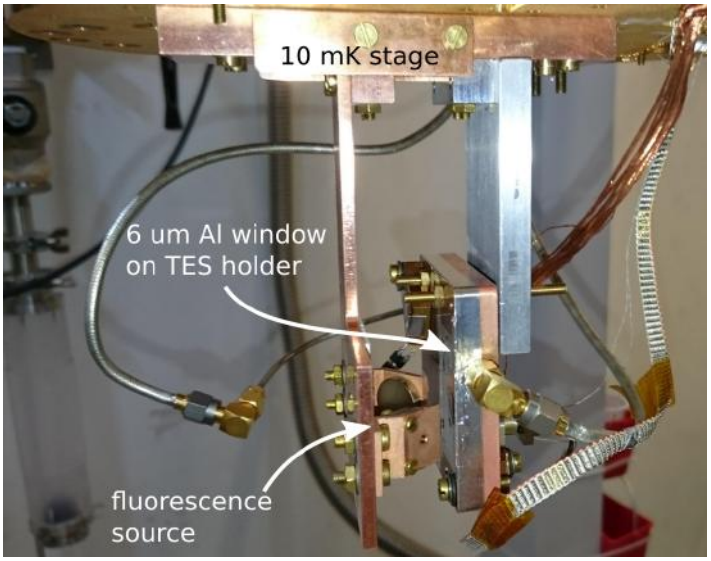

Figure 7.26: Copper holder facing fhe fluorescence source

Material	Surface [mm^2]	Expected rate [counts/s]	Energy [keV]
Al	10×10	2.7E-3	1.486
NaCl	13×13	3.2E-3	2.622
$CaCO_3$	6.7×6.7	18E-3	3.692

Table 7.5: Simulation results for the optimisation of the geometrical characteristics of the X ray fluorescence source

7.6.1 Thermal conductance

The thermal conductance G that links the TES to the thermal bath sets not only the decay time of the thermal pulse but also the shape of the I-V curve since G regulates the power flow, hence the steady state of the biased TES. For HOLMES it is important to have an exponential thermal constant of the order of $\tau_- \sim 150\mu s$ in order to reduce the dead time of each detector after an energy deposition. By studying the behaviour of the TES at different temperatures we can evaluate the thermal conductance towards the heat sink. Keeping in mind that

$$P_{bath} = k(T^n - T_{bath}^n) \tag{7.11}$$

with k and n depending on the properties of the materials that provide the thermal link to the bath. We can express the constant k in terms of the thermal conductance G and the critical temperature T_c

$$k = \frac{G}{nT_c^{n-1}} \tag{7.12}$$

The power flowing to the bath can be calculated for each temperature biased at the same TES resistance (in this case 25% of R_n)

$$P_{bath} = R_{TES_{25}} \times I_{TES_{25}} \tag{7.13}$$

with R_{25} and I_{25} being the value of the TES resistance and the corresponding bias current at 25% of the normal resistance value. Substituting 7.13 in 7.11

$$I_{TES_{25}} = \sqrt{\frac{k}{R_{TES_{25}}}(T_c^n - T_{bath}^n)} \tag{7.14}$$

we can therefore fit the acquired data and extrapolate the parameters K, n and T in order to calculate

$$G = nKT^{n-1} \tag{7.15}$$

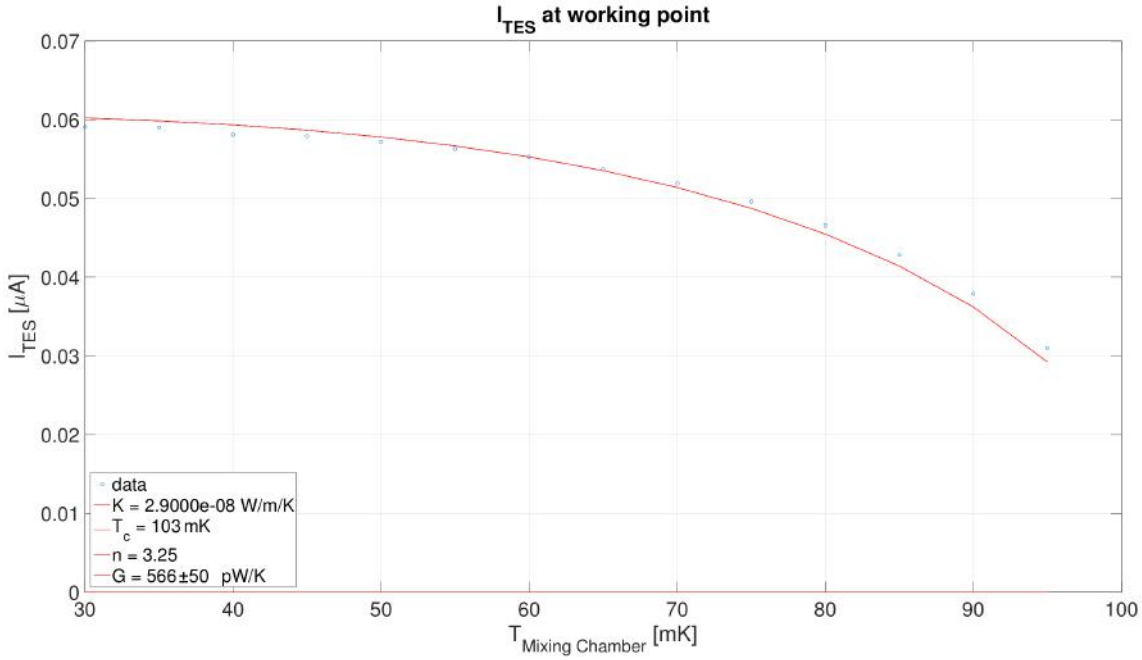

Figure 7.27: Example of a measurement of the thermal conductance of a detector with high conductance value towards the sink. The measured value 566±50 is in agreement with the NIST design value of 570 pW/K

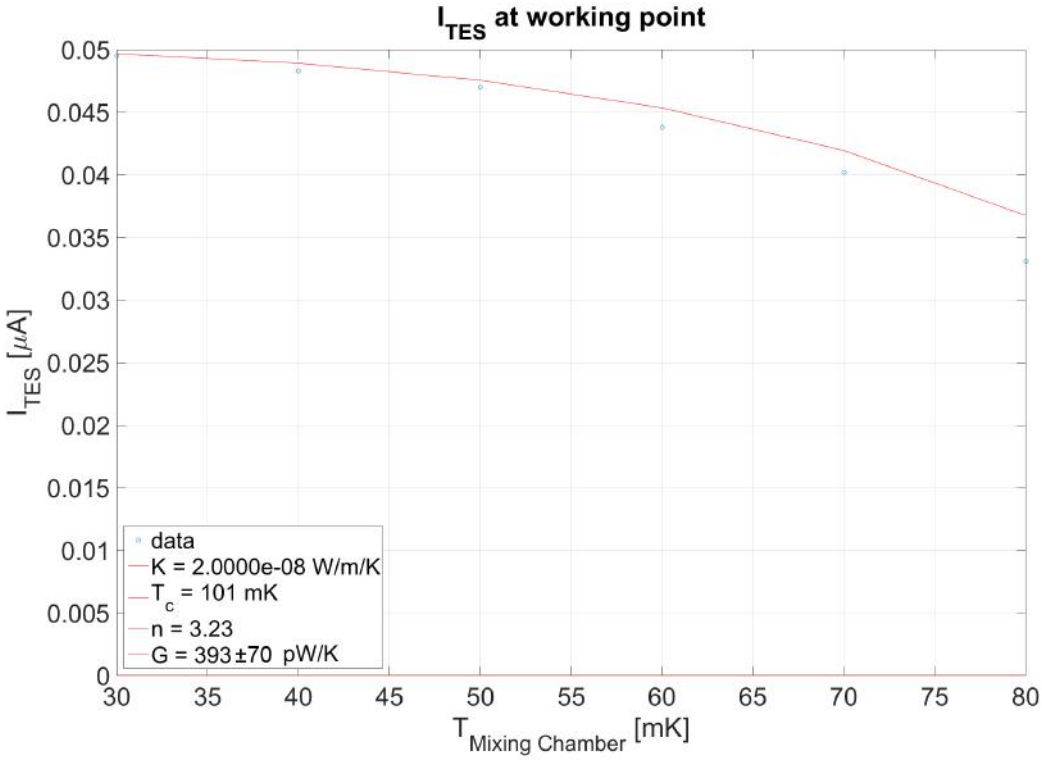

Figure 7.28: Example of a measurement of the thermal conductance of a detector with low conductance value towards the sink. The measured value 393±70 is in agreement with the NIST design value of 430 pW/K

The detectors from NIST have been designed to have two different values of thermal conductance, namely 430 pW/K and 570 pW/K. The most suitable for HOLMES are clearly those with the higher conductance since not only fast rising pulses are needed but also a fast decay time in order to reduce the dead time of the detector after an energy deposition in the absorber. Yet, for the sake of comparison of the resolution and response, amongst the six types of detectors I have also tested two which had G=430 pW/K.

7.7 Detector response

In order to choose the most suitable design for the detectors for HOLMES I have tested detectors with similar characteristics but slightly different design, such as with different geometry of the thermal link between absorber and TES or varied thickness of the copper thermal conductance towards the thermal bath. The aim was to choose the design with the best time response and resolution. The transition shape, and hence the detector response are slightly influenced by the different G and by the thermal connection to the bath itself, and since it is not trivial to predict the R(T,I) response of each detector, it is important to test different designs in order to chose the best one. All the detectors have been measured with a collimator atop the detector chip which was aligned so that only the absorbers could be hit

TES	G [pW/K]	Inductance [nH]
8	570	70
9	570	86
11	570	70
12	430	84
14	430	70
19	570	70

Table 7.6: Set up summary of the measured detectors. Detector number 8 and 11 were measured during a separate cooldown.

by the X-rays from the calibration source. TES 8 and 11 have been measured from a second copy of the TES chip and without a collimator. In Figure 7.29 there is a scheme of the tested detector geometry are shown, while in the Table 7.6 a list of the significant parameters for each TES are reported.

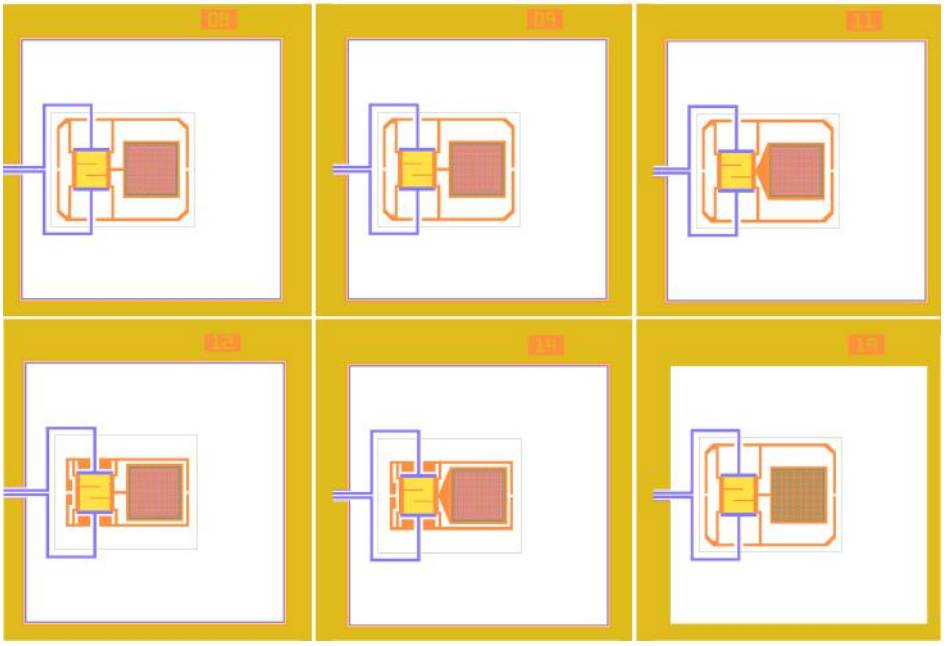

Figure 7.29: Design of the six detectors chosen to be tested. Different geometries of the absorber-TES thermal link have been tested in order to exclude pulse shape alteration or any rise time dependence.

7.7.1 Rise time

The detector response to an energy deposition is described by the coupled differential equation described in Chapter 4. Solving the differential equation for a delta like energy deposition we obtain a model for the detector response. It is crucial for HOLMES to have a ~ μs time resolution, which can only be achieved with a 10 μs τ_R detectors. In Figure 7.30 an acquired pulse is compared with the prediction from the electrothermal model of the TES. The slight disagreement on the decay time of the pulse could be due to the two body nature of the TES and absorber heat capacities. Yet, this is of no concern since it affects just the decay time of the detector and leaves the rising edge unchanged.

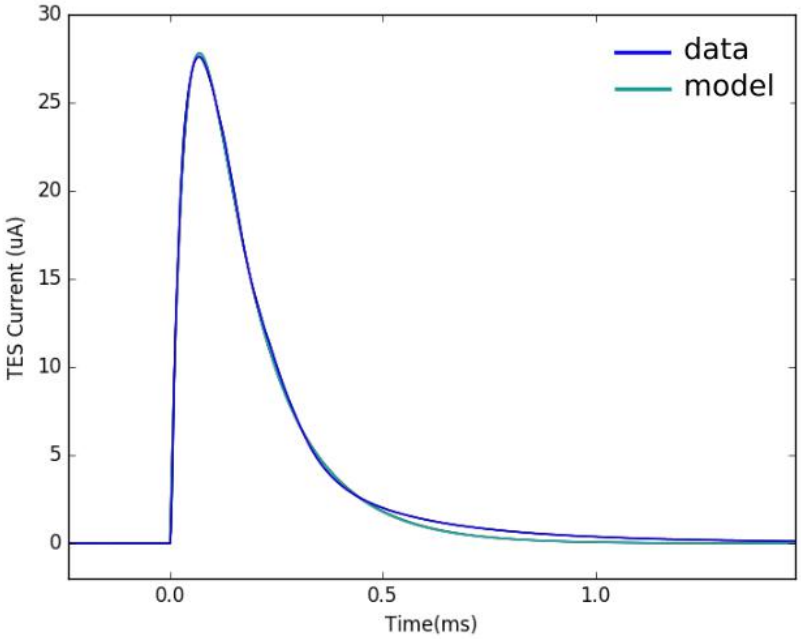

Figure 7.30: Data and model of the detector response to a 5.9 keV energy deposition. It can be seen that the two body model is in good agreement with the data. α=40, β=1, L=86 nH

I have measured detectors with 70 nH and 86 nH inductance. The inductance value determines the electronic rise time τ_{el} which sets the limit on the effective τ_R of the pulse. In our current setup the choice of inductance allowed us to measure detectors with no less that 70 nH, which corresponds to an effective τ_R= 16 μs. The same detector was measured with 70 nH and 86 nH showed a $\tau_{R,70}$=15.6±0.5 μs and $\tau_{R,86}$=19.2±0.7 μs, fitted with a single exponential, as showed in Figure 7.31.

The TES for HOLMES will have 50 nH inductance, which will allow the rise time of the pulses to go as low as 10 μs, as predicted by the electro thermal model by Irwin described in Chapter 5.

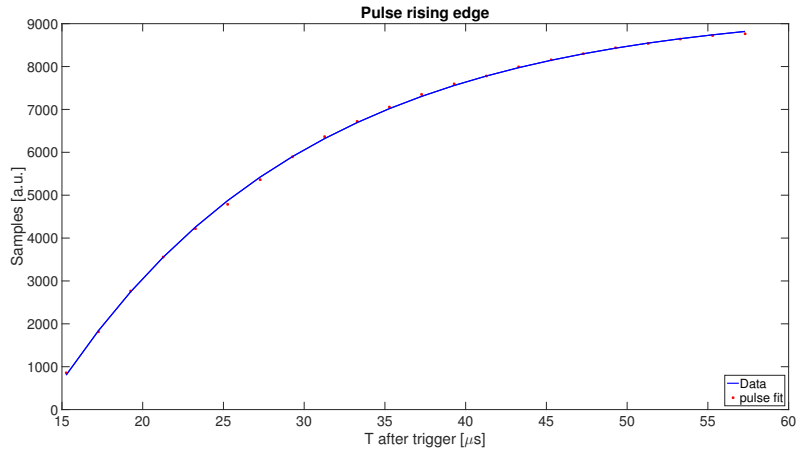

Figure 7.31: Close up of the rising edge of a detector with 70 nH inductance fitted with a single exponential; exponential coefficient $\tau_{R,70}$=15.6±0.5

7.7.2 Position dependency

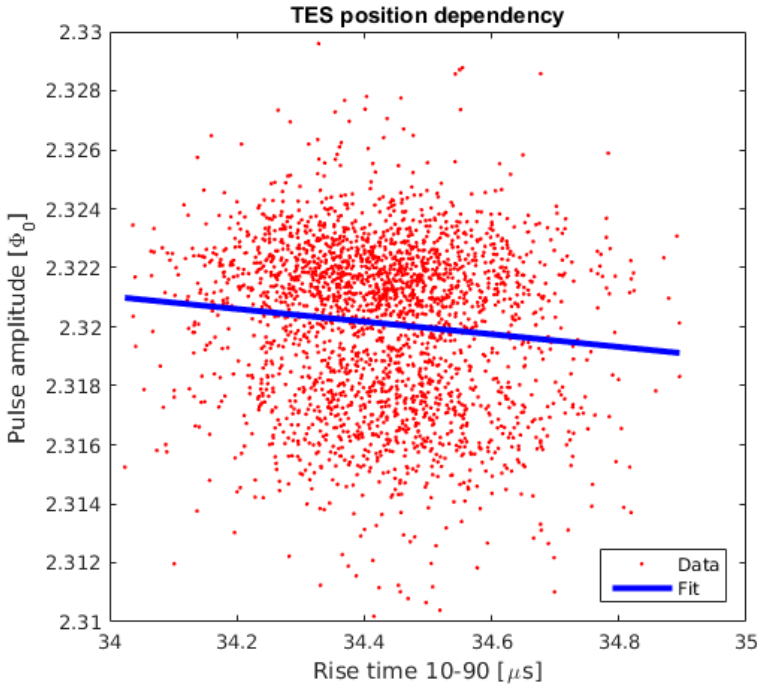

Figure 7.32: Scatter plot of rise time (10 % to 90 %) vs amplitude for TES 9.

In order to investigate position dependency I have studied the correlation between the rise time and the amplitude of the pulses during a calibration run with a ^{55}Fe source. If the

response of the detector is dependent by the position of the energy deposition, the amplitude and the rising edge of the pulses change for different interaction points in the absorber. In Figure 7.32 the plot of pulse amplitude vs rise time is shown for the events in the 5.9 keV of the spectrum. A slight correlation is visible. To evaluate the significance of this correlation I have performed a linearisation of the amplitude according to the linear fit, as shown in the Figure, I was then able to quantify the degradation from position dependency comparing the resolution before and after the linearisation. The resolution on the 5.9 keV peak improved by 1%, i.e. 50 meV.

7.7.3 Detector response

All detectors were illuminated with a Mn K-α X-ray emitting source which emits photons at 5.9 keV and 6.5 keV. For the estimation of the signal to noise ratio, pulses from the 5.9 keV line have been compared for all the detectors. The results are shown in Figure 7.33. The difference in the pulse height is probably due to fluctuations of the parameters α and β or of the value of the shunt resistance. This issue needs a deeper understanding in order to assure the reproducibility of the performance across a whole detector array. It will be directly assessed during the first measurements of the 32 detector array which is due in mid 2017. It is worth stressing that this first detector array was meant to be used for testing various designs and the reliability of our experimental setup. Once the best detectors are selected, a new test array will be produced with smaller variations of the selected detectors design and with several copies of the same detector in order to check the reproducibility of detectors in large arrays.

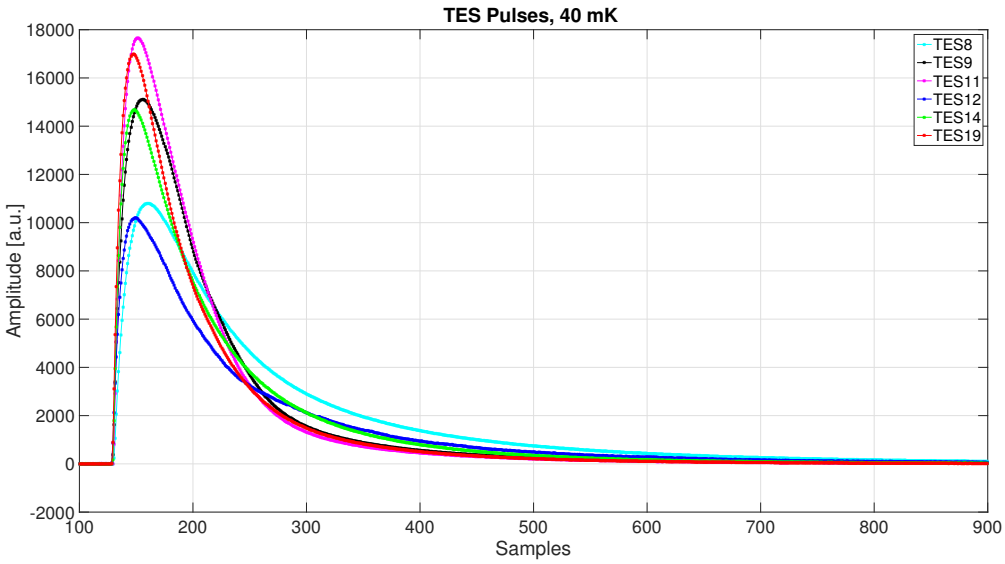

Figure 7.33: Detector response to a 5.9 keV energy deposition.

7.7.4 TES noise

The noise power spectrum of the TES is the sum of the noise of the SQUID, of the Johnson noise due to load resistor and due to the TES, and the noise of the thermal fluctuation through the thermal conductance G. The noise power spectrum has been simulated solving the coupled thermal and electrical differential equations in Chapter 5 and summing up all the contribution. The parameters used for the simulation, i.e., bath temperature, R_{TES} coincide with the parameters used for the spectrum measurement described in the next paragraph. The measured noise spectrum agrees with the expected noise power spectrum predicted for a 1 mΩ TES operated at 40 mK bath temperature with a total inductance of 84 nH; the comparison between expected and acquired data can be seen in Figure 7.34

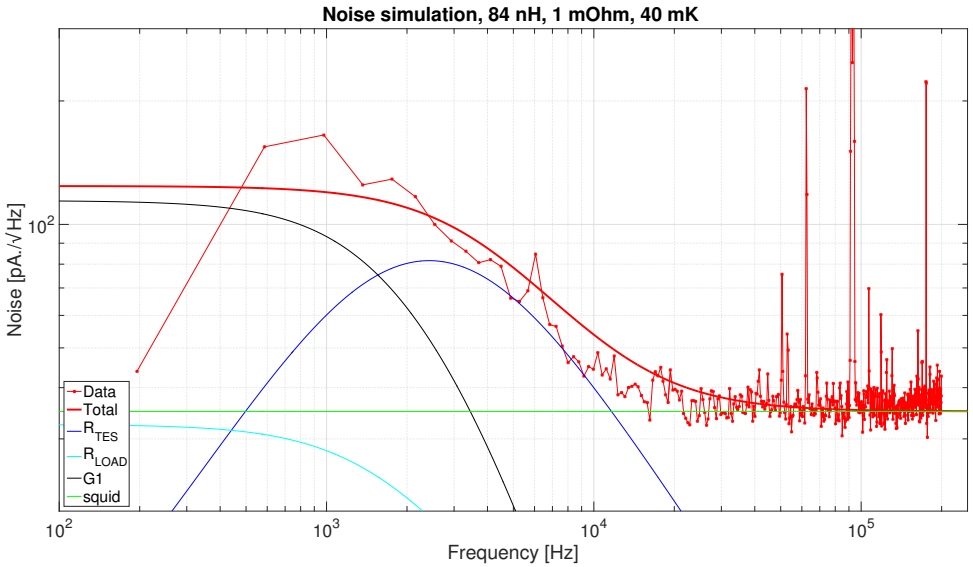

Figure 7.34: Simulated noise power spectrum for TES 9 at 1 mΩ, operated at 40 mK compared with the acquired data.

I have measured the noise power spectrum of the each of the six TES detectors and, in order to predict the best case resolution. To do this I have calculated the signal to noise ratio based on the pulse shape and on the noise power spectrum using the optimal filter. The acquired power spectra are shown in Figure 7.35. The optimal filter estimation of the resolution is based on the ratio of the integrals of the Fourier transform of the pulse with respect to the noise power spectrum and it gives a prediction of the best achievable resolution, without taking into account thermal instability or any other time dependent effect or non-linearity in the detector response. In order to predict the expected resolution of the 5.9 keV peak of the spectrum, a correction for the detector non-linearity is necessary. In our estimation of the resolution at the peak the correction that was used is a *local* calibration of the detector using the 5.9 keV and 6.5 keV peaks. The results are shown in the table below.

TES	OF resolution [eV]
8	5.5
9	4.5
11	7.6
12	8.6
14	7.4
19	5.2

Table 7.7: Expected optimal filter resolution for the 5.9 keV peak.

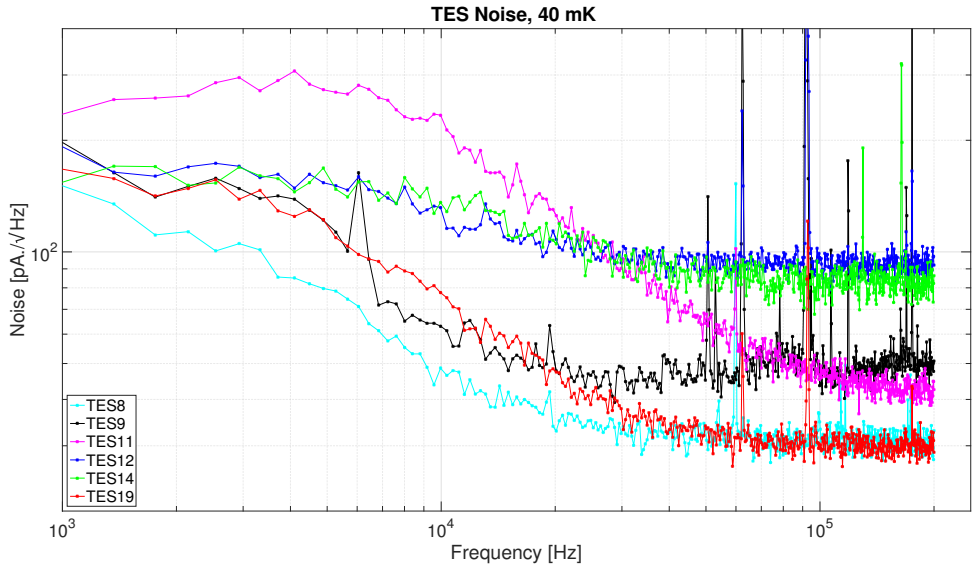

Figure 7.35: Acquired noise for each TES. Each detector has been measured separately in order to bias it with the proper current and set the working resistance of the TES at 1 mΩ. The different shapes are due to variation in the TES parameters in the 10-100 kHz region, and to variation in the SQUID noise at the 100 kHz-200 kHz region.

7.7.5 Energy resolution

In order to study the energy resolution of the TESs, I have illuminated the detectors with a Mn X-ray source emitting photons at 5.9 keV and 6.5 keV. I have further optimised the stabilisation and the working point of the best performing detector, i.e. TES number 9, in order to reach the best energy resolution at 5.9 keV. The continuously acquired data has been triggered offline with a dedicated second order derivative based trigger algorithm and then processed with the optimal filter in order to maximise the signal to noise ratio and produce the n-tuples for the analysis. Before the analysis and the fit of the peak, two corrections

TES	Fit resolution [eV]
8	8.4
9	5.9
11	10
12	19
14	25
19	7.9

Table 7.8: Resolution (FWHM) of the 5.9 keV peak fitted with two gaussians

have been performed: the amplitude was linearised with respect to the the oscillations in time, and with respect to the offset. For the time correction I have fitted the amplitude vs time scatter plot with a high degree polynomial and used the resulting function to linearise the amplitude. Subsequently I performed a linearisation procedure to take into account the gain variation due to change in the working point. Since any shift or drift of the working point causes a variation in the offset of the detector I have linearised the amplitude with respect to the offset of each pulse. After the offline processing I have finally calculated the energy resolution fitting the 5.9 keV peak with the fitting function described in the previous paragraph; the results for the best detector are shown in Figure 7.36.

As can be seen from the SNR prediction and from the noise plots in Figure 7.35, the factor that contributed to the resolution degradation of TES 12 and 14 was the SQUID noise, clearly visible in the high frequency region of the noise power spectrum. Besides, for TES 14 a thermal instability was observed which could not be corrected with the standard amplitude versus offset linearisation. These two detectors are not suitable for HOLMES but we are working in order to understand what is the cause of the instability and response variation over time.

The new detector array will be produced with detectors simliar to TES 9 with some variations that will allow the rise time τ_+ to vary in the range 11–40 μs.

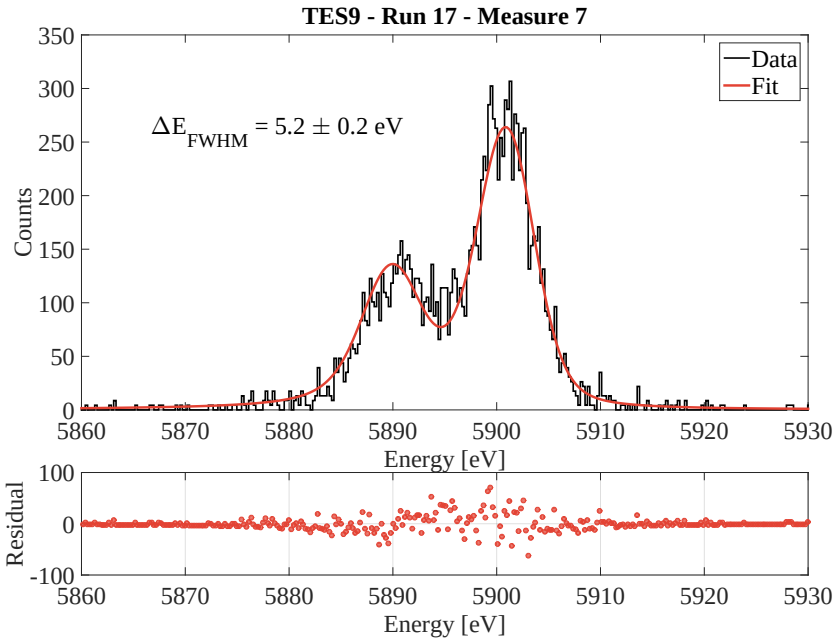

Figure 7.36: TES resolution on the 5.9 keV Mn K-α peak

This was the first time an X ray TES was read out with a multiplexed RF-SQUID system.

7.7.6 TES linearity

For measuring the linearity of the TES response in the region of interest for the neutrino mass measurement with ^{163}Ho a dedicated measurement with a multi line X ray emitting source has been performed. The source has been designed and set up in order to emit X rays from the fluorescence of Al and Cl, besides the ^{55}Fe source has been added. From the peak position it is possible to estimate the linearity of the detector: data has been fitted with a first degree polynomial curve. As ca be seen from the results in Figure 7.38 the response is linear.

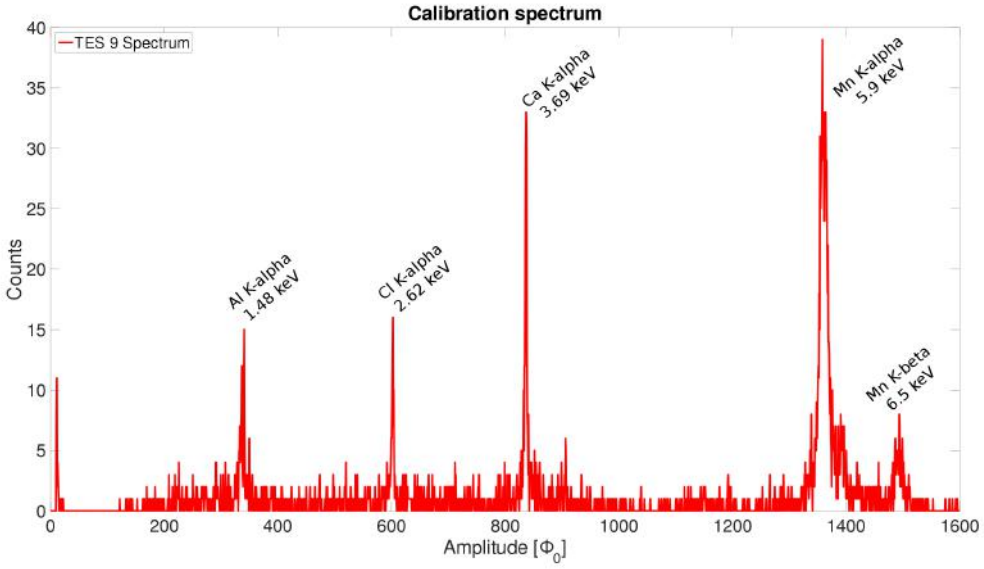

Figure 7.37: Spectrum of a 24 h long calibration spectrum with the fluoresced X ray lines. The spectrum is obtained after pulse shape cuts and detector amplitude vs baseline correction.

During the HOLMES measurement a similar X ray source will be installed in order to perform periodical calibration sources. Even though the ^{163}Ho spectrum can be calibrated using the M and N capture peaks it is important to have a calibration peak above the end point in order to monitor the detector response over time.

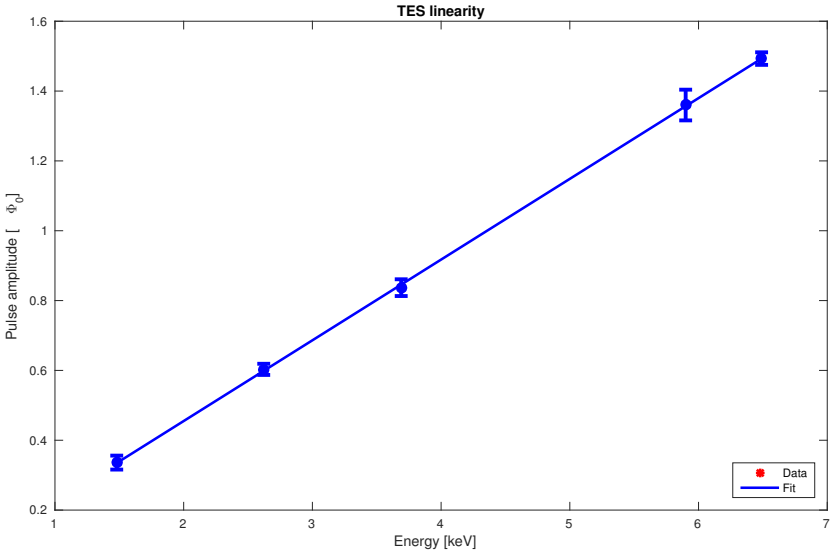

Figure 7.38: X ray energy as a function of the pulse amplitude in the TES; the data is fitted with a first order degree polynomial; χ^2/dof=0.999.

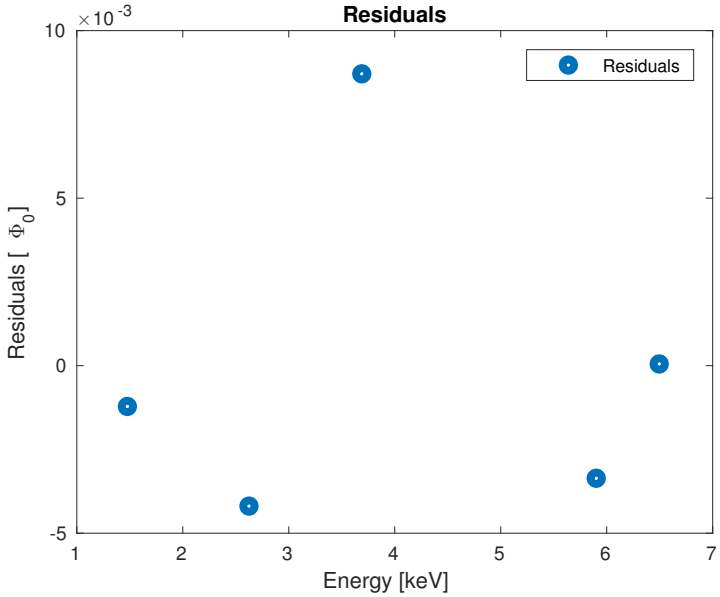

Figure 7.39: Residuals of the 1st degree polynomial fit of the TES response Amplitude vs Energy

Chapter 8

Conclusions

The work described in this thesis followed the first phases of the HOLMES experiment, which started in February 2014. During my PhD a new experimental set up for the operation of Transition Edge Sensors has been installed in the Cryogenic Laboratory in Milano-Bicocca. Even though TES are well known detectors, HOLMES will push the performance of X ray energy range TES to its very limit. Since the goal of HOLMES is to measure the neutrino mass from the Electron Capture spectrum of ^{163}Ho with ~eV sensitivity it is of crucial importance to gather as many statistics as possible around the upper end of the spectrum, where the effect of the non vanishing neutrino mass is visible. In order to reach the designed sensitivity we performed simulations and found the optimal ^{163}Ho activity to be implanted in each of the detectors' Gold absorber is 300 Bq.

To cope with such a high activity while limiting the pile up fraction to 10^{-3} is no trivial matter: the time resolution of the detectors needs to be of the order of $\sim$ µs. Such a performance is indeed achieved with fast rising edge detectors ($\sim$ 10 µs) and with even faster sampling (500 kHz). Additionally, operating a full array of 1000 detectors at ~10 mK requires a multiplexed read out and we decided that the best solution for HOLMES is the use of SQUID amplifiers coupled to microwave resonators.

My thesis followed the initial preparation of the experimental set up of HOLMES. In Milano Bicocca we installed a new cryo-free dilution refrigerator and instrumented it with all the necessary components to perform initially the characterisation runs of the HOLMES prototype detectors and subsequently the HOLMES measurement. Thanks to the knowledge acquired by the group I worked in from the development of microwave kinetic inductance detectors, I was able to easily adapt a two channel analogue homodyne set up for reading out the microwave multiplexed TESs. The signal reconstruction from the rf-SQUID used for the TES readout is not straightforward though and we had to devolp dedicated software in order to acquire, demodulate and save data.

I started by testing our system with an array of more conventional TES detectors provided by NIST, before the first array of prototypes for HOLMES was prepared. The detectors for HOLMES are produced using a so called "sidecar" design, with the Gold absorber placed aside of the TES and connected with a strong thermal link, in order to eliminate the proximity effect of Gold to the superconducting thermometer which was seen to distort the shape of the superconducting transition. Even though the detector type was already roughly estab-

lished, a few variations to the standard design were produced in order to determine and fine tune some detector parameters before producing the final array for HOLMES. The variations included two different thermal conductance values and two differently shaped thermal connections between TES and absorber; additionally, some detectors were produced to study the effect of extra heat capacity. We tested this and determined that the TES response is not influenced by the geometry of the thermal link between the absorber and the TES itself, moreover we have not observed significant position dependency, yet the detector response is influenced by the presence of a second body which is weakly coupled to the TES+aborber complex. The presence of this weakly coupled second body does not affect in any way the performance or the quality of the detectors, but it is an interesting matter which is worth investigating in the near future.

During my PhD period I have characterised the performance of different detectors that have been studied at NIST with Time Domain Multiplexing, a well established and conventional read out technique compared to the Microwave Multiplexing I am using in Milano-Bicocca. I tested the TES detectors using the rf-SQUID readout and we were able to reproduce the performances in term of energy and time resolution reached at NIST, validating the detector design which will be adopted for HOLMES.

Soon HOLMES will switch from our current two channel multiplexed readout to the digital ROACH-2 system allowing us to read out as many as 32 channels with one single board. Indeed, in the near future the implantation system will be ready in Genova and we will be able to measure the first array of 32 detectors with implanted ^{163}Ho.

The measurements performed on the first array of implanted detectors will give important information on the contribution to the detector heat capacity of the implanted atoms and, most important, it will allow us to perform a high statistics calorimetric measurement of the EC spectrum of ^{163}Ho. The experimental data on the spectral shape is of crucial importance in order to test the theorists' prediction of second order processes such as shake up and shake off, which may ultimately enhance the rate at the end point. Once all the tests and preliminary measurements will be performed it will be possible to give a more precise prediction of the sensitivity of the final 1000 detectors HOLMES measurement on the neutrino mass.

List of Figures

Bibliography

[1] F. Reines, "The neutrino: from poltergeist to particle," *Reviews of Modern Physics*, vol. 68, pp. 317–327, 1996. 3

[2] C. L. Cowan, F. Reines, F. B. Harrison, H. W. Kruse, and A. D. McGuire, "Detection of the free neutrino: A Confirmation," *Science*, vol. 124, pp. 103–104, 1956. 3

[3] G. Danby, J.-M. Gaillard, K. Goulianos, L. M. Lederman, N. Mistry, M. Schwartz, and J. Steinberger, "Observation of High-Energy Neutrino Reactions and the Existence of Two Kinds of Neutrinos," *Physical Review Letters*, vol. 9, pp. 36–44, 1962. 4

[4] K. Kodama *et al.*, "Observation of tau-neutrino interactions," *Physics Letters B*, vol. 504, pp. 218–224, 2001. `hep-ex/0012035v1`. 4

[5] B. Pontecorvo, "Mesonium and antimesonium," *Sovietic Physics - Journal of Experimental and Theoretical Physics*, vol. 6, p. 429, 1957. 4

[6] G. Bellini, L. Ludhova, G. Ranucci, and F. L. Villante, "Neutrino oscillations," *Adv. High Energy Phys.*, vol. 2014, p. 191960, 2014. 4

[7] N. Cabibbo, "Unitary symmetry and leptonic decays," *Physical Review Letters*, vol. 10, pp. 531–533, 1963. 4

[8] M. Kobayashi and T. Maskawa, "CP Violation in the Renormalizable Theory of Weak Interaction," *Progress of Theoretical Physics*, vol. 49, pp. 652–657, 1973. 4

[9] F. Capozzi, G. Fogli, E. Lisi, A. Marrone, D. Montanino, *et al.*, "Status of three-neutrino oscillation parameters, circa 2013," *Phys.Rev.*, vol. D89, no. 9, p. 093018, 2014. 7

[10] Y.-F. Li, J. Cao, Y. Wang, and L. Zhan, "Unambiguous determination of the neutrino mass hierarchy using reactor neutrinos," *Phys. Rev. D*, vol. 88, p. 013008, Jul 2013. 9

[11] G. Hinshaw *et al.*, "Nine-Year Wilkinson Microwave Anisotropy Probe (WMAP) Observations: Cosmological Parameter Results," *Astrophys.J.Suppl.*, vol. 208, p. 19, 2013. 10

[12] P. Ade *et al.*, "Planck 2015 results. xiii. cosmological parameters," *ArXiv*, 2015. 10

[13] M. Geoppert-Mayer, "Double Beta-Disintegration," *Physical Review*, vol. 48, pp. 512–516, 1935. 11

[14] E. L. Fireman, "A Measurement of the Half-Life of Double Beta-Decay from $_{50}Sn^{124}$," *Physical Review*, vol. 75, pp. 323–324, 1949. 11

[15] S. R. Elliott and P. Vogel, "Double Beta Decay," *Annual Review of Nuclear & Particle Science*, vol. 52, pp. 15–151, 2002. `hep-ph/0202264v1`. 11

[16] S. Dell'Oro, S. Marcocci, and F. Vissani, "New expectations and uncertainties on neutrinoless double beta decay," *Phys.Rev.*, vol. D90, no. 3, p. 033005, 2014. 12

[17] H. Klapdor-Kleingrothaus, A. Dietz, L. Baudis, G. Heusser, I. Krivosheina, *et al.*, "Latest results from the Heidelberg-Moscow double beta decay experiment," *Eur.Phys.J.*, vol. A12, pp. 147–154, 2001. 13

[18] C. Aalseth *et al.*, "The IGEX Ge-76 neutrinoless double beta decay experiment: Prospects for next generation experiments," *Phys.Rev.*, vol. D65, p. 092007, 2002. 13

[19] C. Macolino, "Results on neutrinoless double beta decay from GERDA Phase I," *Mod.Phys.Lett.*, vol. A29, no. 1, p. 1430001, 2014. 13

[20] A. Barabash and V. Brudanin, "Investigation of double beta decay with the NEMO-3 detector," *Phys.Atom.Nucl.*, vol. 74, pp. 312–317, 2011. 13

[21] R. Arnold *et al.*, "Search for neutrinoless double-beta decay of ^{100}Mo with the NEMO-3 detector," *Phys.Rev.*, vol. D89, no. 11, p. 111101, 2014. 13

[22] K. Alfonso *et al.*, "Search for Neutrinoless Double-Beta Decay of ^{130}Te with CUORE-0," 2015. 13

[23] K. Asakura *et al.*, "Results from KamLAND-Zen," 2014. 13

[24] J. Albert *et al.*, "Search for Majorana neutrinos with the first two years of EXO-200 data," *Nature*, vol. 510, pp. 229–234, 2014. 13

[25] R. Bernabei, P. Belli, F. Cappella, R. Cerulli, F. Montecchia, *et al.*, "Investigation of beta beta decay modes in Xe-134 and Xe-136," *Phys.Lett.*, vol. B546, pp. 23–28, 2002. 13

[26] A. Picard, H. Backe, H. Barth, J. Bonn, B. Degen, T. Edling, R. Haid, A. Hermanni, P. Leiderer, T. Loeken, A. Molz, R. Moore, A. Osipowicz, E. Otten, M. Przyrembel, M. Schrader, M. Steininger, and C. Weinheimer, "A solenoid retarding spectrometer with high resolution and transmission for keV electrons," *Nucl.Instrum.Meth.*, vol. B63, p. 345358, 1992. 18

[27] V. Lobashev, V. Aseev, A. Belesev, A. Berlev, E. Geraskin, *et al.*, "Direct search for neutrino mass and anomaly in the tritium beta-spectrum: Status of 'Troitsk neutrino mass' experiment," *Nucl.Phys.Proc.Suppl.*, vol. 91, pp. 280–286, 2001. 18

[28] A. Osipowicz *et al.*, "KATRIN: A Next generation tritium beta decay experiment with sub-eV sensitivity for the electron neutrino mass. Letter of intent," 2001. 19

[29] J. Formaggio, "Project 8: Using Radio-Frequency Techniques to Measure Neutrino Mass," *Nucl.Phys.Proc.Supl.*, vol. 229-232, pp. 371–375, 2012. 19

[30] e. a. Eliseev, "Direct measurement of the mass difference of ^{163}Ho and ^{163}Dy solves the q-value puzzle for the neutrino mass determination," *Phys. Rev. Lett.*, vol. 115, p. 062501, Aug 2015. 20, 35

[31] C. Bennet, A. Hallin, R. Naumann, P. Springer, and M. Witherell, "The X-ray spectrum following ^{163}Ho M electron capture," *Phys.Lett.*, vol. B107, pp. 19–22, 1981. 20

[32] A. De Rujula, "A NEW WAY TO MEASURE NEUTRINO MASSES," *Nucl.Phys.*, vol. B188, p. 414, 1981. 20

[33] A. De Rujula and M. Lusignoli, "Calorimetric measurements of 163-ho decay as tools to determine the electron neutrino mass," *Phys. Lett.*, vol. B118, p. 429, 1982. 20, 21, 23, 33

[34] W. Bambynek, H. Behrens, M. Chen, B. Crasemann, M. Fitzpatrick, *et al.*, "Orbital electron capture by the nucleus," *Rev.Mod.Phys.*, vol. 49, pp. 77–221, 1977. 20

[35] P. Springer, C. Bennett, and P. Baisden, "Measurement of the Neutrino Mass Using the Inner Bremsstrahlung Emitted in the Electron-Capture Decay og 163Ho," *Phys.Rev.*, vol. A35, pp. 679–689, 1987. 20

[36] A. de Rjula and M. Lusignoli, "Single electron ejection in electron capture as a tool to measure the electron neutrino mass," *Nuclear Physics B*, vol. 219, no. 2, pp. 277–301, 1983. 23

[37] R. G. H. Robertson, "Examination of the calorimetric spectrum to determine the neutrino mass in low-energy electron capture decay," *Phys. Rev.*, vol. C91, no. 3, p. 035504, 2015. 27

[38] A. De Rujula and M. Lusignoli, "The calorimetric spectrum of the electron-capture decay of 163ho. the spectral endpoint region," *JHEP*, vol. 05, p. 015, 2016. 27, 29, 30

[39] A. Faessler, L. Gastaldo, and F. Simkovic, "Neutrino mass, electron capture and the shake-off contributions," *arxIV*, 2016. 27, 29

[40] L. Landau and E. Lifchitz, "Mecanique quantique," *MIR, Moscow*, vol. 36, 1974. 28

[41] R. L. Intemann and L. Pollock, "K -electron ejection accompanying nuclear k capture," *Phys. Rev.*, vol. 157, p. 41, 1967. 28

[42] L. Gastasldo, "Courtesy of," *Presentation at LTD*, 2015. 29

[43] M. W. Rabin, "Courtesy of," *Presentation at LTD*, 2015. 29

[44] A. Nucciotti, "Statistical sensitivity of 163 ho electron capture neutrino mass experiments," *The European Physical Journal C*, vol. 74, no. 11, 2014. 35, 37

[45] M. Lusignoli and M. Vignati, "Relic antineutrino capture on 163ho decaying nuclei," *Physics Letters B*, vol. 697, no. 1, pp. 11 – 14, 2011. 36

[46] J. W. e. a. Engle, "Evaluation of 163-Ho production options for neutrino mass measurements with microcalorimeter detectors," *Nuclear Instruments and Methods in Physics Research B*, vol. 311, pp. 131–138, Sept. 2013. 39

[47] K. Irwin and G. Hilton, *Transition-Edge Sensors*, pp. 63–150. Berlin, Heidelberg: Springer Berlin Heidelberg, 2005. 43, 50, 52

[48] J. Mather, "Bolometer noise: nonequilibrium theory," *Appl. Optics*, vol. 21, p. 1125, 1982. 51

[49] J. A. B. Mates, *The microwave SQUID multiplexer*. PhD thesis, University of Colorado, 2011. 53

[50] D. M. Pozar, *Microwave engineering; 3rd ed.* Hoboken, NJ: Wiley, 2005. 57

[51] P. K. Day, H. G. LeDuc, B. A. Mazin, A. Vayonakis, and J. Zmuidzinas, "A broadband superconducting detector suitable for use in large arrays," *Nature*, vol. 425, p. 817, 2003. 61

[52] J. Gao, J. Zmuidzinas, B. A. Mazin, H. G. LeDuc, and P. K. Day, "Noise properties of superconducting coplanar waveguide microwave resonators," *Appl.Phys.Lett.*, vol. 90, p. 102507, 2007. 61

[53] J. Burnett, L. Faoro, I. Wisby, V. L. Gurtovoi, A. V. Chernykh, G. M. Mikhailov, V. A. Tulin, R. Shaikhaidarov, V. Antonov, P. J. Meeson, A. Y. Tzalenchuk, and T. Lindstrom, "Evidence for interacting two-level systems from the 1/f noise of a superconducting resonator," *Nature Commun.*, vol. 5, p. 4119, 2014. 61

[54] J. Gao, M. Daal, J. M. Martinis, A. Vayonakis, J. Zmuidzinas, B. Sadoulet, B. A. Mazin, P. K. Day, and H. G. Leduc, "A semiempirical model for two-level system noise in superconducting microresonators," *Appl.Phys.Lett.*, vol. 92, p. 212504, 2008. 61, 62

[55] J. Gao, M. Daal, A. Vayonakis, S. Kumar, J. Zmuidzinas, B. Sadoulet, B. A. Mazin, P. K. Day, and H. G. Leduc, "Experimental evidence for a surface distribution of two-level systems in superconducting lithographed microwave resonators," *Appl.Phys.Lett.*, vol. 92, p. 152505, 2008. 62

[56] O. Noroozian, J. Gao, J. Zmuidzinas, H. G. LeDuc, and B. A. Mazin, "Two-level system noise reduction for Microwave Kinetic Inductance Detectors," *AIP Conf.Proc.*, vol. 1185, pp. 148–151, 2009. 62

[57] J. Zmuidzinas, "Superconducting Microresonators: Physics and Applications," *Ann.Rev.Condensed Matter Phys.*, vol. 3, pp. 169–214, 2012. 62

[58] E. Gatti and M. et al., "Processing the signals from solid-state detectors in elementary-particle physics," *Nuovo Cimento Rivista Serie*, vol. 9, pp. 1–146, Jan. 1986. 70

[59] B. A. Mazin, *Microwave Kinetic Inductance Detectors*. PhD thesis, California Institute of Technology, August 2004. 82